Titre: Title:	Impact of Controlled Oxygen Content and Microstructure on the Mechanical Behavior of 13Cr-4Ni Steel
Auteur: Author:	Laura Paim Pressi
Date:	2020
Type:	Mémoire ou thèse / Dissertation or Thesis
Référence: Citation:	Paim Pressi, L. (2020). Impact of Controlled Oxygen Content and Microstructure on the Mechanical Behavior of 13Cr-4Ni Steel [Master's thesis, Polytechnique Montréal]. PolyPublie. https://publications.polymtl.ca/5563/

URL de PolyPublie: PolyPublie URL:	https://publications.polymtl.ca/5563/
Directeurs de recherche: Advisors:	Jean-Philippe Harvey
Programme: Program:	Génie chimique

POLYTECHNIQUE MONTRÉAL
affiliée à l'Université de Montréal

Impact of Controlled Oxygen Content and Microstructure on the Mechanical Behavior of 13Cr-4Ni steel

LAURA PAIM PRESSI
Département de génie chimique

Mémoire présenté en vue de l'obtention du diplôme de *Maîtrise ès sciences appliquées*
Génie chimique

Décembre 2020

POLYTECHNIQUE MONTRÉAL
affiliée à l'Université de Montréal

Ce mémoire intitulé :

Impact of Controlled Oxygen Content and Microstructure on the Mechanical Behavior of 13Cr-4Ni steel

présenté par **Laura PAIM PRESSI**
en vue de l'obtention du diplôme de *Maîtrise ès sciences appliquées*
a été dûment accepté par le jury d'examen constitué de :

Louis FRADETTE, président
Jean-Philippe HARVEY, membre et directeur de recherche
Myriam BROCHU, membre

DEDICATION

To my parents Lauri e Elaine.
To my sisters Juliana, Roberta and Natália.

ACKNOWLEDGEMENTS

First of all, I would like to deeply acknowledge my research director, Professor Jean-Philippe Harvey, who trusted me and offered me this opportunity. I am grateful for all the attention and time dedicated to guiding me in this research and also for the financial support.

Special thanks to Prof. Alexandre Bois-Brouch and his entire team at the Center de Métallurgie du Quebéc for the knowledge and experience that enormously contributed to this project in the synthesis of the samples. Without samples we would have no results.

I would like to thank Prof. Denis Tibault for his availability to share his background solving my doubts as well as for providing access to IREQ for the analyses.

I thank Prof. Myriam Brochu for her cooperation and kindness in managing the use of the laboratory, prioritizing the safety of all users. I also thank the technical assistance of her team, Josée Laviolette and Paul Provencher, thanks for the teaching and contribution in the laboratory analysis and improvement of results. I would like to acknowledge the important help of Simon for the section 4.3.1 in the characterization of my samples.

To my colleagues and friends from CRCT who made this journey more joyful.

My friend Marina Lunardi who has been always willing to assist me in this professional transition to the academic area.

And finally, a special thanks to my friend Samanta Flach for your daily help, making it easier.

RÉSUMÉ

Les turbines hydrauliques en acier inoxydable 13Cr-4Ni sont des composantes critiques des centrales hydro-électriques. Ces pièces sont exposées à des contraintes sévères en service (chargement cyclique dans un environnement d'écoulement d'eau douce). Ces conditions requièrent un design de matériau optimal ainsi qu'une méthode de mise en œuvre précise. Plus spécifiquement, ces turbines subissent de fortes vibrations qui peuvent mener à de la fatigue et à un bris catastrophique de l'équipement. Le débit d'eau douce élevé mène à un environnement dynamique aqueux propice à la cavitation et à la corrosion par piqûres. Ces défauts macroscopiques de surface agissent comme des concentrateurs de contraintes et comme des sites d'initiation de fissure menant à un phénomène de fatigue accéléré. À l'heure actuelle, il y a un manque fondamental de connaissances quant à la contribution du procédé de mise en œuvre de l'alliage et d'autres facteurs qui y sont liés (tels les niveaux d'impuretés et la méthode de fusion utilisée pour faire la synthèse – maintien en température). Cette étude vise à quantifier l'impact de 1) la présence d'impuretés critiques comme l'oxygène et 2) la microstructure de l'acier 13Cr-4Ni (acier CA6NM) sur sa résilience Charpy et sa dureté. L'objectif ultime est de fournir des recommandations permettant d'améliorer la mise en œuvre de l'alliage CA6NM; Ceci afin d'améliorer la performance mécanique et d'usure de l'alliage dans pour cette application de turbine hydraulique. Pour ce faire, une procédure expérimentale de synthèse a été élaborée permettant d'obtenir un acier 13Cr-4Ni propre et exempt d'impuretés. Cette stratégie a été conçue à partir de calculs thermodynamiques (grâce à l'utilisation du logiciel FactSage) et de bilans de matière associés. Dans la première série de synthèse de l'alliage, deux billettes ont été produites dans deux fours à induction (four sous vide et un four avec protection à l'argon liquide). Après avoir confirmé la composition nominale de ces billettes, 7 autres billettes ont été stratégiquement produites avec des niveaux variables d'oxygène. Ces billettes ont été usinées afin de produire deux séries d'échantillons pour réaliser les analyses microstructurales, les tests de dureté et les tests de résilience Charpy à 0 ^{o}C. Une série d'échantillons fut traitée thermiquement grâce à une étape d'austénitisation suivie d'un recuit. Tous les échantillons ont été étudiés dans ces deux états métallurgiques (structure brute de coulée et structure traitée thermiquement). Quatre alliages commerciaux ont également été utilisés comme matériaux de référence. Les tests de résilience et de dureté, ainsi que les analyses chimiques et les caractérisations microstructurales nous ont permis de comprendre l'impact de la présence d'oxygène sur les performances des aciers ainsi synthétisés. Plusieurs types d'inclusions ont également été identifiées et leur impact sur le matériau a été discuté. Les résultats présentés dans ce travail

confirment l'importance d'ajuster finement le procédé de mise en œuvre ainsi que la composition chimique nominale de l'acier pour réduire l'impact négatif de la présence d'oxygène et donc la formation d'inclusions.

Ce projet fait partie d'une étude plus vaste appelée FATCO pour *FATCO: Fatigue and corrosion-fatigue behaviour of 13Cr-4Ni steels and additively manufactured alloys for application to large-size components, such as hydraulic turbines and machinery.*

ABSTRACT

13Cr-4Ni stainless steel hydraulic turbines are critical components of hydroelectric power stations. They are exposed to challenging operating conditions (i.e. cyclic loads in a freshwater environment) which requires optimal material design and manufacturing process. More specifically, these turbines experience strong vibrations and noise that may lead to fatigue and premature failure. The massive freshwater flow also induces a dynamic aqueous environment that promotes cavitation and pitting corrosion. These surface macroscopic defects act as stress concentrators and crack initiators at the origin of accelerated fatigue phenomena. However, there is a lack of understanding about the contribution of the production process of this alloy and other factors related to it (such as impurities and different production methods) affecting the performance of machinery produced with CA6NM.

This study aims at quantifying the impact of 1) the presence of the critical impurities such as oxygen and 2) the microstructure of a 13Cr-4Ni steel (CA6NM) on its notch toughness and hardness behaviour. The ultimate objective is to provide guidance on the improvement of the CA6NM elaboration process that will contribute to the mechanical and wear better performance of this alloy for hydraulic turbine applications.

To do so, an experimental procedure to synthesize a clean and exempt-from-impurities 13Cr-4Ni steel was elaborated based on thermodynamic calculations (using the FACTSAGE thermochemical package) and mass balances. In a first cast trial two steel billets were produced, using two different induction furnaces (i.e. vacuum and argon dripping atmosphere). After confirming chemical composition according to reference values, seven more bars were strategically synthesized with variations in composition, generating specimens with distinct levels of oxygen. The billets were machined to produce two batches of samples for microstructural analysis, hardness and impact Charpy measurements, from each ingot. One batch of samples went under a thermal process which consisted of an austenitization step, followed by a tempering phase. All the specimens were characterized in two conditions, as-cast and heat-treated. Also, four commercial alloys were analyzed allowing comparison.

Mechanical notched and hardness tests, chemical composition analysis, and microstructure characterization of these resulting materials lead us to the knowledge of the impact of the level of oxygen present in the samples on the observed properties. Moreover, the main types of inclusions that are present in this alloy have also been identified, as they are formed and affect the mechanical properties of this steel. It is evident that one needs to fine-tune the synthesis process in order to guaranty low oxygen content and also prevents the presence of

inclusions in the melt.

This project is part of a project entitled *FATCO: Fatigue and corrosion-fatigue behaviour of 13Cr-4Ni steels and additively manufactured alloys for application to large-size components, such as hydraulic turbines and machinery.*

TABLE OF CONTENTS

LIST OF TABLES

LIST OF FIGURES

LIST OF SYMBOLS AND ACRONYMS

A	Austenite
AC	As-cast
ASTM	American Society for Testing and Materials
BCC	Body-Centered Cubic
BCT	Body-Centered Tetragonal
BF	Blast Furnace
BOF	Basic Oxygen Furnace
CMQ	Centre de Métallurgie du Quebéc
CONSARC	Induction Furnace with vacuum system
CVN	Charpy V-Notch
DOE	Design of Experiments
DRI	Direct-reduced Iron
EAF	Electric Arc Furnaces
EDX	Energy Dispersive X-ray Spectroscopy
F	Ferrite
FATCO	Fatigue and corrosion
FCC	Face-Centered Cubic
HBN	Brinell Hardness
H.-Q.	Hydro-Québec
HRC	Rockwell C Hardness
HT	Heat-treated
IREQ	Institut de Recherche d'Hydro-Québec
LCAK	Low-carbon-aluminium killed
M	Martensite
NMIs	Nonmetallic inclusions
OES	Optical Emission Spectroscopy
SEM	Scanning Electron Microscopy
VIP	Induction Furnace with argon-dripping protection

LIST OF APPENDICES

CHAPTER 1 INTRODUCTION

1.1 Context

Hydro-power is one of the most important renewable energy sources worldwide, contributing to about 7% of the global primary energy consumption on earth [1]. For over a century, this process has supplied energy in the form of electrical work (i.e. electricity). Nonetheless, there are still many scientific opportunities to further develop and improve this technology from planning, design and operation perspectives [2].

Hydraulic turbines (figure 1.1) are the most critical devices of hydroelectric power stations. They are used to convert the kinetic energy of water into mechanical work, which is converted into usable electrical energy by a generator. Water turbines can face many mechanical challenges in service because of their operation mode. They are subjected to large cyclic loads which can cause a premature failure induced by fatigue (i.e. crack initiation, crack propagation and catastrophic failure). Besides that, turbines are exposed to fluid dynamics which can lead to cavitation, erosion and even cracking in regions with high-stress concentrations [3]. The damage caused by cavitation in hydraulic turbine components cause high repair costs as well as considerable loss of energy generated by unavailability of the machines, likewise limiting the operational flexibility of the system and reducing the useful life of the affected equipment [4].

In order to minimize these engineering challenges, several studies have been carried out in the past with the objective of developing new materials for the construction of rotors as well as new approaches to recover and repair cavitated regions. With the advent of more efficient materials, the technology Has become more reliable. This material improvement started in the 60s with the manufacturing of hydraulic turbines using the CA6NM stainless steel. This stainless steel cast alloy contains 11.5-14% of chromium, 3.5 to 4.5% nickel and less than 0.06% of carbon [5]. More specifically, the addition of nickel improves its resistance to corrosion and cavitation, as well as its hardness. Due to its low carbon content, this stainless steel also presents a better crack resistance and a great weldability [6].

This material is classified by ASTM as a soft martensitic stainless steel. It presents adequate mechanical properties when considering its use for the manufacturing of turbines. In fact, it is currently the most widely used stainless steel for the manufacturing of this type of equipment.

Figure 1.1 Old Francis turbine (picture taken at Hydro-Québec Électrium in Sainte-Julie, QC)

1.2 Introduction to the FATCO project

This master's project is part of a large scientific collaboration effort entitled FATCO which stands for Fatigue and Corrosion-fatigue behaviour of 13Cr-4Ni steels and additively manufactured alloys for applications to large-size components, such as hydraulic turbines and machinery. FATCO was developed in partnership with Hydro-Quebec (H.-Q.) and SACMI, which is an Italian group that develops large machinery for industrial applications in various industry sectors. This project represents a complementary work to various studies which have already been launched by the partners over the past years. The general objective of this project aims at increasing our fundamental understanding of the fatigue behaviour of the alloy 13Cr-4Ni steel, to seek solutions to improve its mechanical and corrosion properties and consequently its performance in service. Therefore, developing an in-depth study

relating fatigue, fatigue-corrosion damage, and material heterogeneity in this specific alloy is necessary. The FATCO project is divided into 9 milestones that have been spread over 5 years. Each milestone has specific objectives that complement each other; at the end, the results will be shared, offering guidance for the development of an improved stainless steel to extend the life in service of these critical equipment.

1.3 Research objectives of this master's thesis

1.3.1 Partial Milestone 5: Study of the impact of controlled oxygen content and microstructure on the mechanical behavior of 13Cr-4Ni steel

The main objective of milestone 5 is to study how the presence of detrimental impurities, such as S, P, N, O, C, influences the microstructure of the studied material as well as how these impurities affect its toughness performance. To achieve this objective, the milestone has been divided in two parts: 1) alloy synthesis and controlled pollution and 2) characterization of the synthesized alloy microstructure and mechanical properties. The first part of the project consists in the development of a state-of-the-art elaboration strategy (which includes melting and alloying, casting, machining and heat treating) to produce 13Cr-4Ni stainless steel billets with controlled levels of impurities. In this master's project, we only focused on the presence of oxygen to reduce the scope. The second part of the project consists in characterizing the impact of the presence of critical impurities (in this case oxygen) on the microstructure, the v-notch toughness behavior and hardness of 13Cr-4Ni steel. When completed, this study will be a major engineering and scientific contribution for the development of an optimal CA6NM elaboration process that will lead to enhanced performances of the hydraulic turbines. The strategy will also be applied to all the other impurities in future works of the FATCO team.

1.3.2 Specific objectives

This thesis entitled "Impact of controlled oxygen content and microstructure on the mechanical behavior of 13Cr-4Ni steel" aims at synthesizing a large number of 13Cr-4Ni stainless steel samples obtained in different conditions (i.e. different levels of oxygen in as-cast and heat-treated states) in order to quantify the impact of the presence of oxygen on the properties of this CA6NM alloy. More specifically we want to study the effect of oxygen on the microstructure (via the presence of inclusions), the v-notch toughness and the hardness of this stainless steel.

Here are the specific objectives of this project:

- Elaborate an experimental synthesis protocol based on thermodynamic simulations (mass and energy balances) to obtain 13Cr-4Ni steel billets in two different induction furnaces (vacuum and argon-dripping).
- Validate the chemical composition and level of impurity in the cast billets.
- Characterize the microstructures of the as-cast billets and compare them to standard materials provided by IREQ in order to refine the casting procedure.
- Cast and machine 7 billets with controlled oxygen content (ppm wt.)
- Perform austempering heat treatment to modulate the microstructure of the stainless steel.
- Analyze the chemical composition, microstructure and mechanical performance of all the samples.

1.4 Thesis outline

The content of this thesis is organized in five chapters according to the following description. In the chapter 1, an introduction is presented contextualizing the project, defining the problems and objectives of this study.

The chapter 2 consists of a literature review which explains how we can develop the optimized martensitic structure of the 13Cr-4Ni alloy from the as-cast structure using austempering heat treatment. We explain the role of each alloying element on the behavior of this stainless steel. We also briefly introduce the industrial elaboration processes of this alloy which explains the origin of the various impurities that are present in the final product. The main mechanical properties of the 13Cr-4Ni are also discussed. The presence of inclusions, their morphology as well as their effects on the material thermo-mechanical behaviour are finally detailed in this chapter.

The complete methodology of this study is presented in the chapter 3 of this thesis. The synthesis process of the cast billets is explained in detail (with a brief review of vacuum and argon-dripping furnaces). We also discuss in this section the design of experiment (DOE) that was developed for this project, along with the thermodynamic calculations that were used to refine the methodology. We then explain the sample preparation (i.e. grinding, polishing and etching) followed by the description of the analyses and mechanical tests that were performed. This includes a description of the chemical composition analysis techniques, the strategy used for the identification of the inclusions and for the general characterization of

the microstructure of each sample. Charpy and hardness tests performed in order to evaluate of the mechanical performance of the alloy are explained to complete this chapter.

The main results are presented and discussed in details in the chapter 4. The bulk chemical composition of all the synthesized samples are explained at the beginning of the chapter. A detailed data analysis on the presence of inclusions is provided. In sequence, a deep discussion is presented on the characterization of the inclusions present in the synthesized specimens and reference samples. After, the results of mechanical tests are presented and debated. At the end of this chapter, the samples resulting from the Charpy are also characterized.

The important findings of our study are summarized in the chapter 5. The final conclusions and important recommendations for both our industrial partner and the scientific community are listed. At the end, we indicate potential future research paths that could be followed to continue our work and report the limitations of our work regarding the knowledge transfer to the industrial manufacturing of turbines.

CHAPTER 2 LITERATURE REVIEW

2.1 13%Cr-4%Ni stainless steel

Stainless steel is a metallic alloy composed of iron, chromium and nickel as well as a limited amount of carbon. The main characteristic of this alloy is its high resistance to corrosion and high temperature in service. Depending on the application and required mechanical performance, other elements that modify and improve its basic properties may also be added to fine-tune its bulk composition [7].

The 13%Cr-4%Ni steels are grades within the martensitic stainless steel family. These alloys were developed for the manufacture of large-size equipment such as hydraulic turbines. Their chemistry was tailored to improve their mechanical performance giving the requirements of high fatigue resistance, great resistance to corrosive atmosphere and cavitation [8].

For this alloy, a martensitic structure is typically formed after a rapid solidification of the alloy from its liquid state. Apart from carbon, other alloying elements such as Mn, Cr, Mo and Ni act as equivalent-carbon to promote the formation of this metastable phase. Martensite is hard and brittle and often require a heat treatment to obtain a more ductile material. It has a body-centered tetragonal crystal structure which is out of equilibrium, resulting from a phase transformation promoted without any diffusion.

The quenching and associated abrupt drop in temperature traps the carbon atoms (an other alloying elements) within the crystalline structure of the host iron matrix before they can diffuse outside of it. This process results in a slight distortion of the crystal structure of the matrix, leading to the increase of the steel hardness [9, 10]. The alloying elements present in the steel determine its hardenability which is directly linked to the necessary cooling rate required to generate a martensitic structure. Higher levels of elements of specific alloying elements (such as Mn, Cr, Mo and Ni) result in greater propensity to form martensite [11].

It is known that the 13%Cr-4%Ni steel firstly solidifies in a delta-ferrite BCC structure before transforming into austenite [12]. From this state, air cooling is typically sufficient for most of the austenite to transform into martensite. It is also possible that a relative amount of delta ferrite remains in the microstructure at the end of the process [7]. Therefore, the resulting martensitic microstructure may contain a limited fraction of delta ferrite and also some residual austenite, from the incomplete conversion of austenite to martensite [13]. As indicated in the Schaeffler diagram presented in figure 2.1, 13Cr-4Ni steels are situated close to the martensite, martensite-ferrite and martensite+austenite regions.

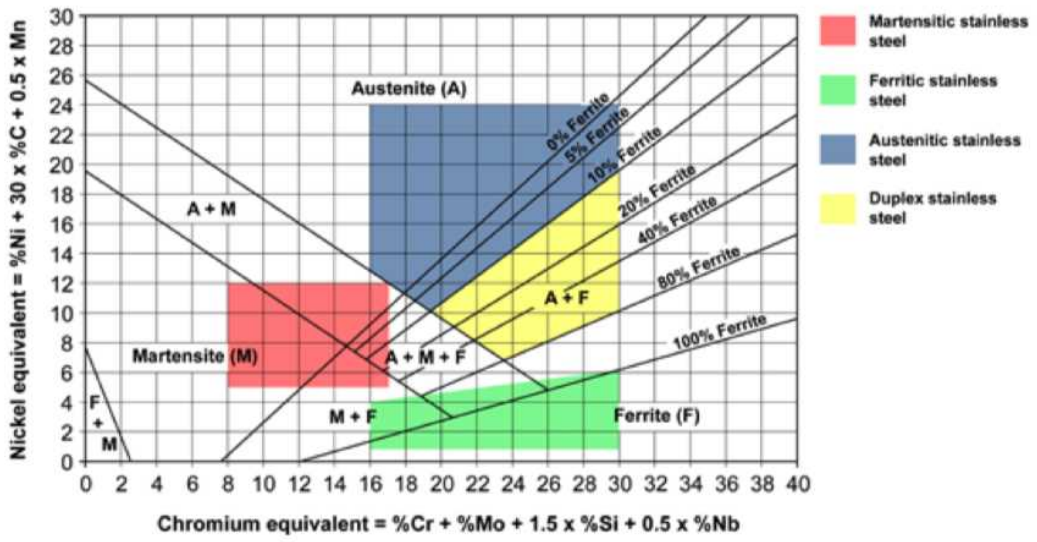

Figure 2.1 Shaeffler diagram presenting different phase assemblage zones considering nickel and chromium equivalent. Colors highlight the position of the major stainless steel families (red = martensitic, green = ferritic, blue = austenitic, yellow = Duplex), taken from [14] and modified by [15]

The two main morphologies of martensite are lathes and plates. The martensite in lath (also called massive martensite) is formed in steels that have small carbon contents, not exceeding 0.6% by weight. Whereas the morphology in plates (also called lenticular martensite), the carbon content is greater than 1%. When the presence of carbon is between 0.6% and 1% C, there will be the formation of a mixed microstructure. The massive martensite is presented as cells formed by distinct laths, whereas, the substructure of the martensite is formed by plates. [16]. The differences between these microstructures can be seen in figure 2.2, where (a) represents the lath martensite, (b) the plate martensite in a high-carbon matrix, followed by (c) which shows the mixed morphology.

CA6NM steels, which contain very low carbon content, present martensite in the form of lathes [17], as shown schematically in figure 2.3. The laths are parallel to each other, containing the same crystallographic orientation, forming blocks. The set of parallel and quasi-parallel blocks is identified as a package. Many packages can be found in a single austenitic grain [18]. This substructure configuration characterizes the way in which the plastic deformation and orientation of the system occurred when the energy released by the martensitic transformation was dissipated [19].

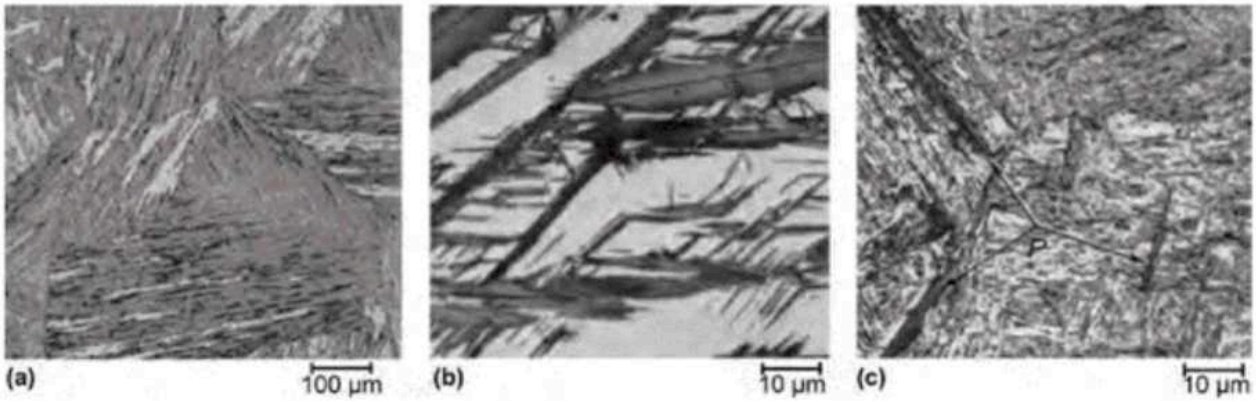

Figure 2.2 Micrographs of different martensites morphologies, (a) lath martensite, (b) plate martensite and (c) mixed morphology [20]

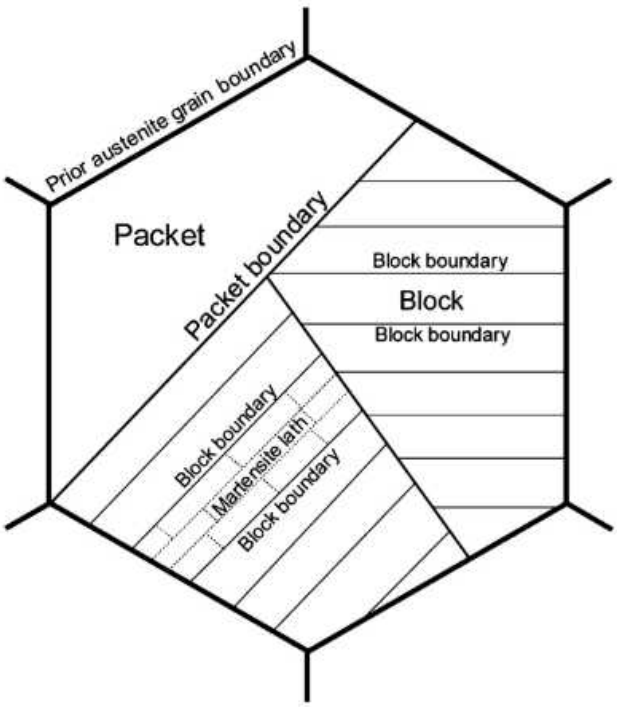

Figure 2.3 Graphical representation of the formation of lath martensite microstructure [18]

2.2 Alloying elements and impurities

The addition of specific alloying elements will lead to an improvement of specific material properties in order to reach the desired performance in service. Here is a list of the different alloying elements present in the 13Cr-4Ni stainless steel and their principal role:

2.2.1 Alloying elements

Cr: A Stainless steel typically must have a minimum of 10.50 wt.% chromium in order to be able to develop a protective Cr_2O_3 layer at its surface. This element is therefore responsible for great corrosion resistance. Depending on its relative amount in the alloy and upon the exposition of the material to oxygen, a protective film on the steel surface (Cr_2O_3) will form. This oxide layer will further prevent the corrosion of the material. The presence of chromium can also lead to the precipitation of carbides and nitrides which are to be avoided as they locally deplete the material in chromium (and prevent from the formation of a continuous oxide layer). It also acts as a ferrite promoter-stabilizer [11].

Ni: Nickel is an face-centered cubic structure stabilizer and contributes to the austenite formation, partially suppressing the formation delta-ferrite. Therefore Ni increases the mechanical strength, the toughness of the alloy and its ductility [11].

Mo: Molybdenum improves the corrosion resistance and high temperature strength of the alloy by carbide precipitation (which also prevents the formation of chromium carbides). It is a ferrite promoter [21].

Mn: It is added in very low quantity, below 1 wt.%. Manganese forms MnS that prevents the formation of FeS, which lead to hot shortening. It also strengthen the steel matrix by substitution solid solution hardening [11].

Si: Silicon adds fluidity to the molten alloy, which justifies a higher content in welded materials. Silicon forms intermetallic components with Fe and Cr and also promotes the formation of carbides. Silicon adds resistance to high temperature corrosion and acts as a ferrite-promoting element [7].

C: Carbon plays an important role in the steel composition since the hardness is greatly affected by its presence. The formation of carbides make the structure brittle, favoring cracks. A higher carbon content will result in a martensite of greater hardness. Carbon is also quite reactive with chromium, leading to the precipitation of chromium carbide to be avoided. For these reasons, very low carbon concentration is desired. Carbon is a gamma-promoting element [22].

2.2.2 Critical impurities

O: The presence of oxygen should be avoided as it leads to the formation of brittle inclusions which have detrimental effects on the mechanical performance of the alloy. This topic will be covered in details in the next sections.

S: Sulfur negatively impact the machining, hot forming, and weldability due the formation of low-melting point phases.

P: Phosphorus also forms low melting point phases that account for hot shortening. A concentration below 0.025 wt.% reduces the possibility of formation of the undesired phases [23].

H: Hydrogen is another undesirable element. It has a major solubility difference between the liquid and solid state in iron, which results in the formation of porosity upon solidification.

2.3 Heat treatment

The martensite, in the after-quenching state of the stainless steel, is practically never kept as-is because of its poor mechanical properties. Therefore the application of a heat treatment is required. This heat treatment, aims at relieving the stresses generated by the formation of martensite. In addition, the heat treatment will reduce the hardness of the material to the values specified by the industrial collaborator of this project.

The formation of a totally martensitic microstructure is expected from the as-cast state, which will present the highest hardness that can be achieved during the material elaboration. Then a specific austempering heat treatment is performed. Depending on the heat treatment heating and cooling rates, holding time and associated holding temperatures, the desired microstructure and hardness.

CA6NM steels are normally austenitized between 950 to 1050 °C, a range of temperatures at which occurs the homogenization of the segregated elements, the dissolution of carbides and decomposition of the delta ferrite remained from the cast. The austenitization temperature must not be too low, as this leads to low values of toughness due to the non-dissolution of the carbides and, at the same time, it must not be too high in order to avoid the sharp growth of the austenitic grains [24].

As mentioned by Foroozmehr *et al.*: *"In the as-quenched state, the microstructure of 13%Cr-4%Ni martensitic stainless steels is a combination of lath martensite and small amounts of delta ferrite. During subsequent tempering at around 600 °C, the martensite is partially transformed into stable austenite, forming a so-called "reformed austenite" phase"* [25], which

is thermally stable.

The objectives of using a tempering treatment are diverse and depend basically on the steel chemical composition and the final application of the material. In most martensitic steels, such as the CA6NM, tempering is used in order to increase toughness and ductility. More specifically, the phenomena related to tempering are: carbon segregation and carbide precipitation; recovery and recrystallization of the martensitic structure as well as the formation of ferrite [26]. Also, in the specific case of CA6NM steels, another consequence of the tempering treatment is the presence of reformed austenite that will be retained after the cooling to room temperature. However, when a deformation is applied to it, it turns back to martensite. This is the TRIP effect, which stands for transformation induced plasticity. Reformed austenite is thus mechanically unstable [27].

The material softening that occurs during tempering improves ductility and resilience, due to the double action of the tempering treatment: on the one hand, the martensite hardness is reduced after the relaxation of residual stresses in the martensitic structure, and on the other hand, there is the re-formation austenite which leads to the improvement of mechanical properties according to Bilmes [12].

Most of the mechanical properties as strength, hardness, and toughness are highly dependent on the heat treatment. According to the thermal process, theses mechanical characteristics can be fine-tuned [7]. Performing a thermal treatment under the optimal tempering temperature will provide both a high proportion of reformed austenite and a good mechanical stability, which will improve the crack propagation resistance of the CA6NM [27].

Figure 2.4 represents a schematic of the heat treatment steps during our proposed austempering thermal process. It starts with fresh martensite in the as-cast structure. The austenitization step will erase this microstructure and will form austenite which will be transformed to martensite upon cooling. The final microstructure will mostly consist of tempered martensite as well as some fraction of retained austenite and some delta-ferrite.

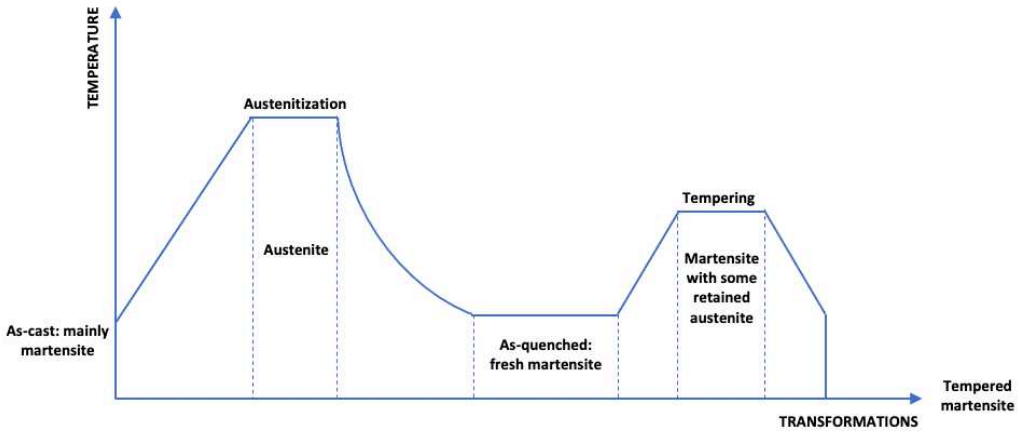

Figure 2.4 Graphical representation of the phases evolution during a typical heat treatment of the CA6NM, starting from its as-cast state

2.4 CA6NM

CA6NM cast stainless steel was developed in Europe in the 1960s to meet the requirements of mechanical properties of parts used in aggressive media such as hydraulic turbines, with the objective of increasing the service life of these machines. This steel is part of the family of 13%Cr-4%Ni steels which are stainless steels with martensitic structures, presenting ideal mechanical properties for their use in applications subjected to heavy loads and corrosive media. This steel chemistry allows to prevent aqueous corrosion, to obtain high toughness as well as good resistance to erosion by cavitation, good casting properties and great weldability [28].

Cast steels are classified based on their use and chemical composition, with a designation defined by the High Alloy Product Group of the Steel Founders' Society of America. The first letter of the CA6NM steel designation refers to its resistance in corrosive media (C) specifying the use of this alloy in an aggressive and humid environment. The second letter refers approximately to the ratio of chromium/nickel. The following character is a number that indicates the maximum carbon content (in weight percentage X 100). Finally, the subsequent letters correspond to the first letter of the alloy elements present in the material, in this case, nickel (N) and molybdenum (M) [8].

According to ASTM A-743/A743M [29], CA6NM has around 13 wt.% chromium, 4 wt.% nickel, molybdenum and a maximum of 0.06% carbon. Table 2.1 shows the permissible ranges of chemical composition to give this alloy the adequate mechanical and corrosion

properties for its use in hydraulic turbines. Table 2.2 presents the desired properties of the CA6NM alloy for this application as provided by H.-Q.:

Table 2.1 The CA6NM chemical composition (wt.%) according to ASTM-A-743/743M [29]

C	**Mn**	**P**	**S**	**Si**	**Cr**	**Ni**	**Mo**
0.06	1.00	0.04	0.03	1.0	11.5-14.0	3.5-4.5	0.40-1.00

Table 2.2 Desired properties of CA6NM requested by H.-Q.

Property	**Target**
V-notch toughness	Minimun 50J at 0 °C
Hardness	Maximum 285 HBN
Microstructure	Martensitic structure

2.5 Steelmaking

It is important to recognize that the performance of the 13Cr-4Ni stainless steel will be directly linked to the presence of impurities such as oxygen, sulfur, phosphorus and hydrogen. These impurities are introduced at various stages of the elaboration of the material. They can come from the minerals used to produce primary iron (such as P and S) as well as from their elaboration process (such as O and H) and recycling.

There are two main processes that are used to obtain iron and steel. The blast furnace-basic oxygen furnace (BF-BOF) route uses a blast furnace to convert iron-rich concentrates to carbon-saturated liquid iron followed by a basic oxygen furnace to remove carbon. This process is also known as basic oxygen steelmaking and iron ore, coal and steel scrap are used as raw materials.

The second possibility is a path that uses a mix of recycled steel and pre-reduced iron pellets (also called direct-reduced iron (DRI) pellets) in an electric arc furnace (EAF). The availability of recycled steel will define the ratio of scrap-to-DRI used in the furnace [30]. The figure 2.5 illustrates the integrated manufacturing for the iron and steelmaking process.

The blast furnace is a shaft furnace fed continuously by top with iron ore, coke and limestone. In a counter-current flow, from the bottom of the furnace, hot air is blown. Excess carbon in the reactor reacts with the oxygen forming ultimately CO gas, which ascends in the furnace

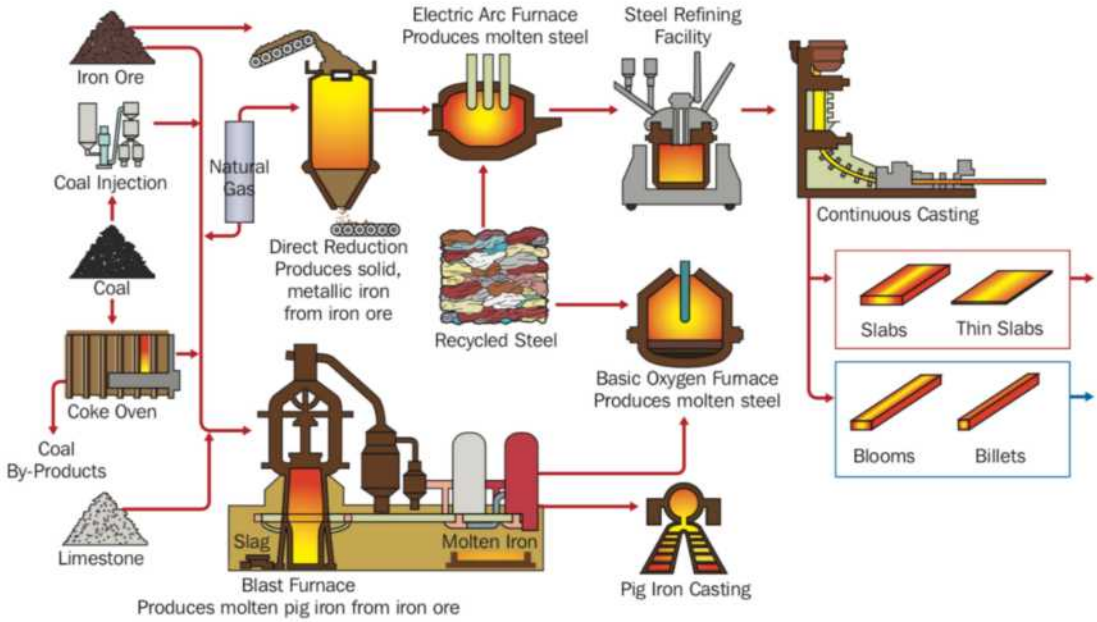

Figure 2.5 Overview of the Ironmaking and steelmaking production processes [31]

reducing the concentrate. At the bottom of the furnace liquid iron is collected. On the top of the metallic melt, there is the formation of slag that floats due its lower density and can be skimmed, removing impurities from the process. The hot metal is saturated with carbon, containing around 4-6 wt.%. This liquid iron goes to the BOF where scrap steel can also be mixed. In this reactor pure oxygen is blown into the molten metal removing the excesses of carbon and other impurities (such as manganese, silicon, etc) and converting hot metal to pure iron. The decarburization step is required in order to obtain an acceptable amount of carbon. An excessive carbon content leads to a fragile steel [32]. To refine the quality of the metal, the residual oxygen that remains in the molten metal is removed in the refining step where deoxidizer as well as other alloying elements are added.

A synthetic slag phase can also form at the top of the unit and can be removed. The molten steel can then be cast. The EAF process also lead to the formation of a molten iron-steel that needs to be further refined. As mentioned previously, the EAF uses a mix of direct reduced iron pellets and recycled steel scrap that are melted by electric arcs followed by similar steel refining step [30].

2.6 Inclusions (oxide, carbide, intermetallic)

In steelmaking, the physical, mechanical and corrosion properties of the final product are controlled by its entire process history (including liquid alloying, refining, solidification and heat treatment). The optimization and fine-tuning of the steel properties to improve the performance of the material in service is often connected to the metal cleanliness [33].

The cleanliness of the steel is in turn related to the presence of impurities which form inclusions during the elaboration process and/or traces of undesired elements/components in the matrix. It is well known that inclusions and precipitates play an important role in the mechanical properties of steel (such as strength, fatigue, machinability, ductilibility, etc.) mainly because they represent discontinuities and act as stress concentration sites [34].

They also may impact the corrosion resistance of the material, especially if they deplete the steel with valuable elements such chromium and molybdenum which controlled the formation of the oxide layer at the surface of the material to prevent its corrosion.

Typically, their presence is characterized in the steel in terms of volume fraction, size and distribution, composition, and morphology. It is understood that the composition and structure of the inclusions can present different behaviors during metalworking. For the desired properties to be achieved, it is necessary to have a control of the main characteristics of the inclusions [35]. As mentioned by Da Costa e Silva: *"Tailoring inclusions to improve properties and performance became an important feature of steelmaking and in the 1980s the term inclusion engineering was coined to describe this process"* [33].

Inclusions present in stainless steel are normally identified as oxides, sulfides, oxy-sulfides, nitrides, carbides, and carbonitrides. These undesired components are also described as non-metallic inclusions (NMIs), besides nitrides, carbides and carbonitrides that are designated as precipitates. Precipitations normally occur in the solid state causing a severe impact on steel properties through grain refinement and precipitation strengthening [35].

Non-metallic inclusions are mainly classified by their chemical composition and according to the phase of the metallurgical process in which they are developed. The composition classification depends on the nature of the inclusion (oxides, sulfides, etc) and the relation to the stage of formation differs if the inclusion is formed before the beginning of the solidification process (named primary) or those formed while the steel solidifies (secondary). This classification is effective concerning when inclusions are formed or removed. Primary NMIs are developed in the liquid phase and can possibly be removed, unlike secondary inclusions that are formed while the structure solidifies which makes removal impossible. However, the inclusions that can not be removed can be "tailored" in order to cause less impact on the

properties of the final product [33].

Another pertinent classification is related to the source of the inclusions. Inclusions classified as indigenous inclusions are introduced in liquid or solidifying steel as a product of reaction in the making process, generally as a great amount of tiny particles in steel. Inclusions incorporated in the steel by contact with liquid steel are named exogenous inclusions, coming from fragments of refractories or particles of slag, are presented irregularly and in smaller quantities as coarse particles with indefinite format. The origin of these nonmetallic phases regularly can be from the main process, which liquid steel is transferred between vessels, or/and the refining steps of the steel production, as well as precipitation within solid steel and casting process [36].

The inclusion size is also a common way of classification of NMIs, being identified as macro and micro inclusions. Kiessling's proposal [37] presents the distinction between sizes: i.e., an inclusion is classified as macro in case during the process or use of product the inclusion is wide enough to cause prompt defect. Other inclusions which do not cause instantaneous failure are identified as micro inclusions. Since this designation of sizes is made arbitrary, in order to identify macro and micro inclusions, it becomes difficult to apply and justify this classification. However, it is still important as a classification regarding the size [33].

The objective of the quality control in the steelmaking process ensures the desired amount and properties of inclusions. The formation of various inclusions also depends on the steel composition and the sequence of processes necessary to achieve required composition as deoxidation and/or alloying procedures. Thus, the inclusions characteristics can be set according to the synthesizing process and the demanded steel properties [35].

In this project, we will prove that oxygen saturation is typically reached when using an open-air induction furnace, even with the use of argon-dripping at the top of the melt. To lower the oxygen content dissolved in the molten alloy, deoxidation agents such as aluminum and Si-Mn master alloys can be used. These deoxidation agents dissolve in the melt and then react with monatomic oxygen to form solid particles that will float at the surface. Figure 2.6 presents the evolution of the oxygen saturation as a function of the melt temperature calculated using the FactSage software. These calculation were performed using the nominal composition of the 13Cr-4Ni targeted in this project. We also see on this figure the equilibrium oxide phases that should form during the elaboration process of the alloy. We found in the literature [35] that these endogenous inclusions will grow mostly by solid particle collisions. Other secondary inclusions will form as well in the steel during its solidification since the oxygen solubility is virtually 0 in solid iron.

Another important point to consider is that the oxygen content of the steel can potentially

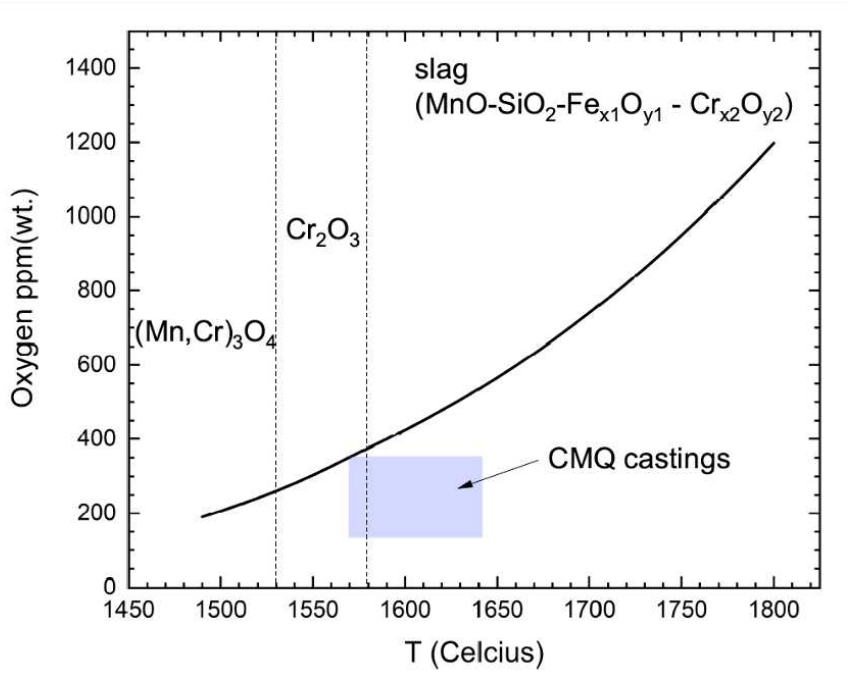

Figure 2.6 Evolution of the oxygen solubility in the liquid 13Cr-4Ni as well as the oxides saturating the melt as a function of the temperature. The temperature range and oxygen content reached during the synthesizes of this project is highlighted in blue

be higher than the equilibrium solubility limit because of many factors such as: 1) reaction between the refractory and the steel, 2) oxidation by the air atmosphere via slag-free zones at the surface of the melt induced by too violent gas stirring, and 3) oxygen contamination by other additions. Exogenous inclusions may also be present in the final material because of different steelmaking operations. As an example *Yang et al.* reported that the transfer of steel between the various vessels may lead to clogging of tundish nozzles due to inclusions buildups (such as corundum and spinel inclusions). Such deposits will constrain the molten steel flow in the unit, may break off and be entrained in the final product. This ultimately leads to the presence of detrimental exogenous inclusions in the solidified steel. These inclusions are most frequently identified as MgO-Al_2O_3 or MgO-Al_2O_3-CaO crystals, and are referred to as spinels. This solid solution contains ions with different charges, for example Mg, Ca and Al [38].

The formation of complex mixed oxides may also occur in this type of stainless steel. They are mainly oxides of manganese, silicon and aluminium originated from the deoxidation process.

An extensive study is presented on the formation of possible oxides from the $MnO - SiO_2 - Al_2O_3$ ternary oxide system in steel [36].

The following considerations were made by Zhang and Thomas regarding the sources of non-metallic inclusions formed in low-carbon-aluminum killed (LCAK) steel [39]:

- Most of the indigenous inclusions in LCAK steel are formed because of the deoxidation process. The dissolved oxygen reacts with the added deoxidant (aluminum) producing the inclusions, i.e. alumina. Aluminum inclusions may be of dendritic shape when produced in a high oxygen concentration, or may result from the collision impact among smaller particles.

- Alumina is considered as a reoxidation product, which can form if, the aluminium remaining in the liquid steel is oxidized by FeO, MnO, SiO_2 and other oxides presented in the slag, as well as refractory linings or if atmosphere exposition occurs.

- During transfer between steelmaking vessels, metallurgical fluxes are entrained in the steel resulting in liquid inclusions, which are usually spherical. This phenomena is known as slag entrapment.

- Exogenous inclusions can act as sites for heterogeneous nucleation of alumina. Presenting large and irregularly shaped because of its origin as loose dirt, broken refractory brickwork, and ceramic lining particles.

- Some inclusions can form without knowing the origin, (i.e. as chemical reactions), forming oxides from inclusion modification which can be observed when Ca is added to the melt and the treatment is not executed properly. However inclusions containing CaO may also originate from entrained slag.

Even at the high temperatures that are necessary in steelmaking operations (around 1600 °C), several oxide inclusions are solid. Thus, their prolonged presence in the liquid state would lead to a round shape appearance. They can also be presented as dendritic structures (ex.: Al_2O_3) and become spherical as they spent time in the iron melt; this transformation in the morphology of the particles is due to the reduction of their surface area and thus their total internal energy [40].

There might be a rupture of the oxides particles when submitted to heat stresses, forming an assemblage of stretched shape fragments. This is due to the high hardness of oxide inclusions compared to the steel matrix. Nevertheless, harder oxide particles that do not break up

during heat treatments may fracture at a later stage. This may result in the formation of conical gaps at inclusion-matrix interfaces as austenite contour the particles [36].

Figure 2.7 shows a schematic diagram presenting some inclusions that may form in aluminum-killed steel, comparing different shapes in an as-cast steel and the transformation due to hot rolling, where "A" represents Al_2O_3 and "C" represents CaO [23].

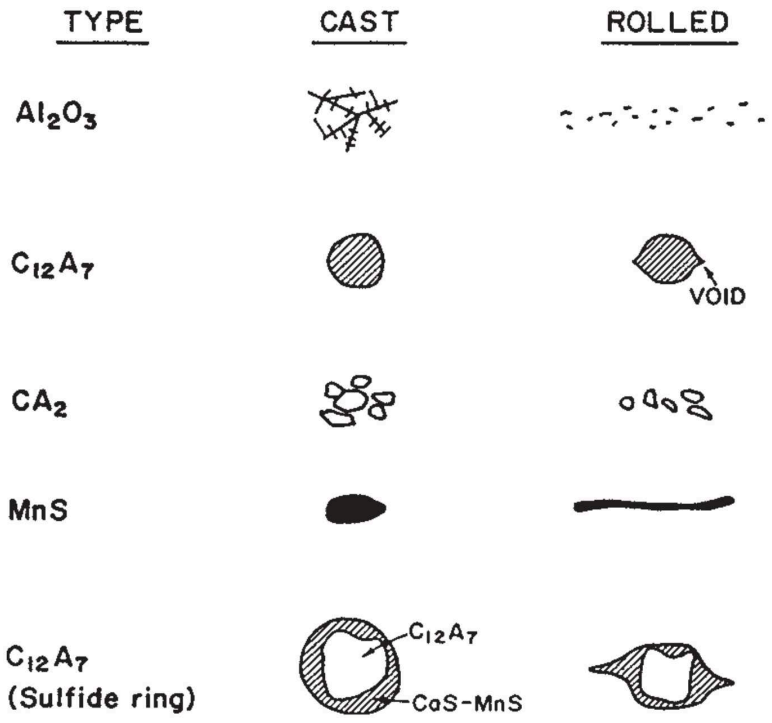

Figure 2.7 Schematic of the inclusions forming in LCAK steel, in the as-cast and hot rolled state. In this figure "A" being considered as Al_2O_3 and "C" as CaO [23]

Since aluminium is widely used as a deoxidant agent, several studies have been performed aiming to better understand the behavior of this agent added to the molten steel. In the study of Steinmetz and collaborators [41], the growth morphology of alumina particles present in steel as a function of its activity in the melt is graphically detailed (figure 2.8). Figure 2.9 taken from Tiekink *et al.* [42] presents a more detailed variation of all the possible alumina particle shapes. This figure demonstrates the effect of both the level of oxygen and concentration of aluminium on the morphology of the resulting inclusions. Both figures are adapted by Da Costa e Silva which presented a recent study on the origin and control of non-metallic inclusions in steel [33].

The alloy composition influences directly on the arrangements that may form, manganese sulfide (MnS) are present in mostly steels. Manganese is intentionally added to form MnS

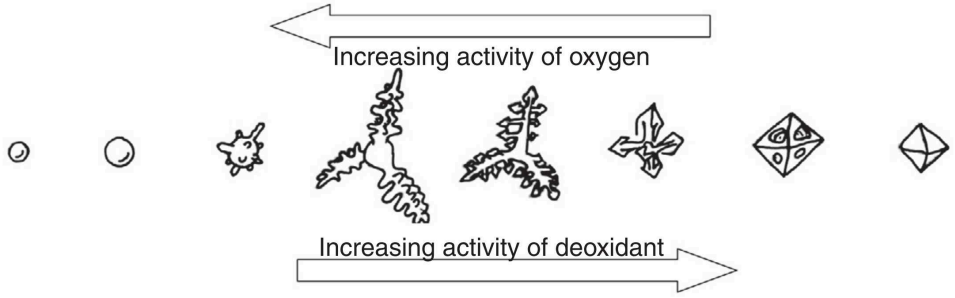

Figure 2.8 Schematic of the inclusion shapes as a function of the activity of aluminium and oxygen in the liquid steel (the figure is not in scale) [41], adapted by [33]

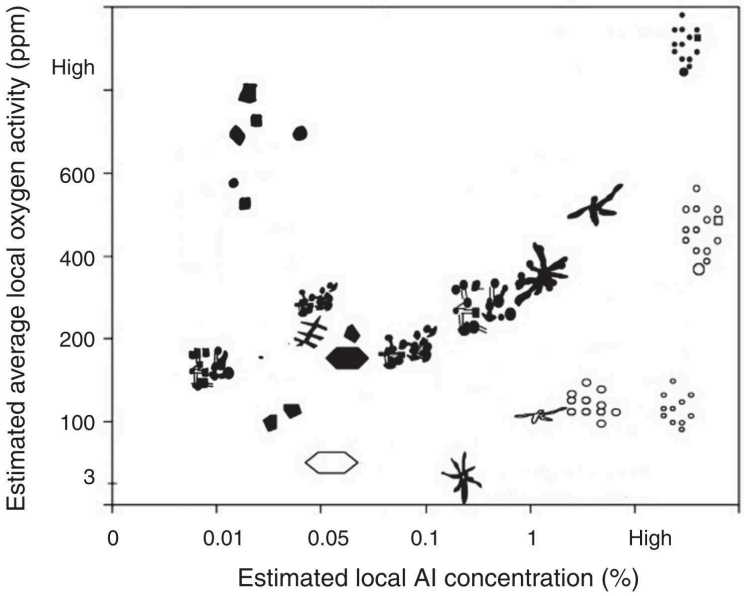

Figure 2.9 Schematic of the different shapes of alumina inclusion as a function of the estimated oxygen and aluminium concentration in the molten steel [42], adapted by [33]

instead of forming FeS, which occurs when there is not enough manganese in the composition. The presence of FeS is avoided because it compromises the resistance of the steel to heated work, due to the low melting point of this compound [43].

2.7 Effect of discontinuities on the mechanical and corrosion behavior of the steel

It is known that critical properties such as fatigue, toughness and corrosion are highly influenced by the presence of defects such as inclusions, porosities, grain boundaries, dislocations and more. These defects may origin from the melt and can also be formed as a consequence of the solidification process (including the cooling rate), the presence of different alloying elements, the level of impurities and the subsequent thermo-mechanical history of the material to obtain the final product. There is a wide varieties of defects according to [25, 44, 45] that negatively affect the microstructure and the performance of the material in service.

There are important efforts in the material science community to tailor the properties of the inclusions that are present in steel in order to reduce their impact. This scientific field is called inclusion engineering. The mechanical properties of inclusions play an important role on the overall strength of the material. This is due to the usually large difference of strength between the particle interface and the bulk matrix [46]. Various experiments studies considering different types and sizes of inclusions were developed by Murakami and Endo. As they reported, the size of the inclusion that are present in the stressed zone is directly related to fatigue failure. [47].

In the review made by Da Costa e Silva, the author concluded that *"when considering the literature on crack origination and propagation in fatigue one must consider the size and volume fraction of NMIs. Crack origination may occur "in the matrix" or related to second-phase particles, in special NMIs"* [48].

Corrosion-related impacts were studied by *Ryan et al.*. They detected regions around sulfides inclusion that had a lower chromium content. These zones were identified as favorable places for corrosion promotion, since chromium is the most important element to form a protective layer at the top of the steel [49].

Williams et al. [50] also conducted studies on the presence of sulphides in stainless steel. It was noted that the formation of a Fe layer around the inclusion which, when dissolved, would favorably lead to the formation of corrosion pits. The inclusion engineering technique is suggested there in order to prevent this behavior, leading to a steel optimal resistance to corrosion.

Other studies performed on this specific alloy (i.e the CA6NM) [51, 52] verified the impact of the carbon carbon content and heat treatment on the resulting microstructures and mechanical properties. However there is still a lack of knowledge regarding the effect of presence of other critical impurities on the behavior of this material.

CHAPTER 3 METHODOLOGY AND EXPERIMENTAL PROCEDURE

The present section defines the methodology that has been used to synthesize 13Cr-4Ni stainless steels alloys with controlled levels of oxygen content, which is the impurity under investigation in this study. This novel methodology was developed in collaboration with the Centre de la Métallurgie du Québec (CMQ). The CMQ provided the expertise regarding melting, casting and chemical characterization of our samples. Two types of furnaces technologies have been used: i.e. vacuum induction melting and argon-dripping induction melting.

3.1 CA6NM synthesis

When the project started, there were no 13Cr-4Ni commercial samples available that were out of spec in terms of different critical impurities such oxygen, nitrogen, sulfur and hydrogen. Furthermore, our scientific project required a controlled level of each specific impurity to elucidate their respective role on the mechanical and corrosion performance of the material. Finally, there were no standard materials available for this project that met the targeted chemistry in terms of impurities ranges.

Because of that, the first step of this master's project was to generate 13Cr-4Ni stainless steel specimens with the exact same bulk composition as the material used in the elaboration of the turbines of our industrial partner (i.e. Hydro-Québec). By using a precise mass balance strategy, we were able to purposefully contaminate the stainless steel batches with different levels of oxygen. These synthetic alloys were then cast, cut, machined and heat-treated. Ultimately, these samples could be analysed in terms of: chemical homogeneity, hardness, microstructure, V-notch toughness and corrosion behavior.

As mentioned previously, there were two furnace options at the CMQ to produce the stainless steel melt and cast the billets: one induction furnace called CONSARC which works under vacuum, and a second induction furnace identified as VIP, operating in an open atmosphere with a protection of liquid argon dripping on the top of the melt. As it will be presented later in the results section (chapter 4), there is a drastic impact of the melting technology on the metallurgical quality of the steel used to produce the billet, even with equivalent level of oxygen. The vacuum furnace prevented us from skimming the melt to remove the slag phase forming at the top of the liquid metal while the open atmosphere required more technical experience to prevent further air contamination during the melting and casting operations.

3.1.1 Experimental procedure

The main objective of our methodology was to mimic the chemical composition of the CA6NM commercial alloy used by our industrial partner. To do so, we decided to use pure raw materials (see table 3.2) and we tried to avoid any synthetic slag production to control the chemistry of the melt. Table 3.1 lists the targeted chemical composition of the alloy, with some additional constraint on the carbon content (i.e. below 0.03%).

Based on the chemistry of these available raw materials (table 3.3), an initial mass balance was performed to quantify their respective amount, taking into account their purity. Table 3.1 shows the expected composition of the cast bar based on the proportion each raw material presented in table 3.2.

It is to be noted that the absolute amount of produced melt to be cast was constrained by the volume capacity of the graphite mold available at the CMQ. Based on these considerations, a total amount of around 9kg of stainless steel was produced for each batch.

Table 3.1 Chemical composition (wt.%) required by Hydro-Québec (nominal). These are maximum values, except where ranges are specified. Iron concentration represents the balance. The expected composition of the cast bar based on our mass balances is also presented in this table.

Fe	**C**	**Mn**	**P**	**S**	**Si**	**Cr**	**Ni**	**Mo**
Nominal:								
Bal.	0.03	0.5-1.0	0.03	0.03	0.6	11.5-14.0	3.5-5.5	0.5-1.0
Expected:								
81.05	0.01	0.90	0.01	0.00	0.14	12.73	4.40	0.75

Table 3.2 Proportion (wt.%) and masses (g) of master alloys for each cast ingot, resulted from the mass balance.

Ingredient	**Proportion (%)**	**Mass (g)**
Fe master	75.358	6836.36
Ni master	4.396	398.79
Fe-Cr master	18.117	1643.57
Addition: Mn	0.873	79.19
Addition: Mo	1.256	113.94
Total	100	9071.85

Table 3.3 Elemental composition of each raw material used in our work (wt.%)

Master alloys	**Fe**	**C**	**Mn**	**P**	**S**	**Si**	**Cr**	**Ni**	**Mo**
Fe master	99.925	0.004	0.04	0.007	0.0027	0.003	0.01	0.006	0.0015
Ni master	0.0012	0.0007		0.0002	0.0007	0.0005		99.9	
Fe-Cr master	28.987	0.025		0.016	0.002	0.77	70.2		
Addition: Mn	0.001	0.001	99.7		0.03	0.002		0.0002	
Addition: Mo	39.5	0.44		0.0005					59.8

Thermodynamics calculations were also performed using the FactSage thermodynamic software to complete the experimental protocol. More specifically, we simulated the melting process in order to identify for example the potential volatility of some alloying elements (like Mn) to limit the maximum temperature (and vacuum pressure when applicable) of the furnace. Based on a preliminary analysis of these simulations, it was expected to lose manganese by evaporation during the melting process. This information was taken into account in the establishment of the mass balance by adding more Mn-containing raw material into the melt.

FactSage also provided useful information about the oxygen solubility in the melt as a function of temperature, as well as the inclusions to be expected in the presence of this impurity. The FactSage simulations were also used to define the required range of temperature to en-

sure that all the raw materials would melt and that an homogeneous molten phase would be produced.

3.1.2 Induction furnaces

Both melting furnaces available at CMQ are electrical furnaces with the operation based on heating through electromagnetic induction. This technology mainly consists of an inductor and a crucible. The crucible is surrounded by a copper wire that forms a coil. An alternative current passes through the primary inductive circuit, leading to the generation of an alternating magnetic field. Under the influence of a magnetic field in a body placed inside the inductor, an electric field appears which induces eddy currents (also called Foucault current). These eddy currents will generate heat because of the Joule effect (electrical resistance of the materials). This phenomenon will ultimately melt the material inside the crucible. The main difference between the furnaces is that the CONSARC works under a controlled atmosphere (vacuum) while the VIP is an open system.

CONSARC - vacuum

The CONSARC furnace (figure 3.1) operates between 0.06-0.1 Torr with a water-cooled crucible. During the heating process, the material in contact with the crucible might solidify or not completely melt. Thus, to prevent alloying elements losses trough this unreacted-solidified layer, an extra amount of Fe-Cr master alloy was added at the bottom of the crucible at the beginning of each experiment as suggested by CMQ. Also, since this equipment works in a closed system, the melting and pouring into the mold occur under vacuum, there is no possibility to skim the melt to remove the slag.

VIP - argon dripping protection

The VIP furnace (figure 3.2) works in open atmosphere. To prevent excessive oxidation of the melt, a protective layer of liquid argon drips on the top of the melt. Since this furnace works in open system mode, it is possible to add the ingredients/master alloys in different stages, to verify the condition of the mixture and to periodically evaluate the temperature of the melt. At the end of the melting process it is also possible to remove the produced slag, a process called skimming of the melt.

Figure 3.1 Picture of a CONSARC furnace which operates in a closed system under vacuum

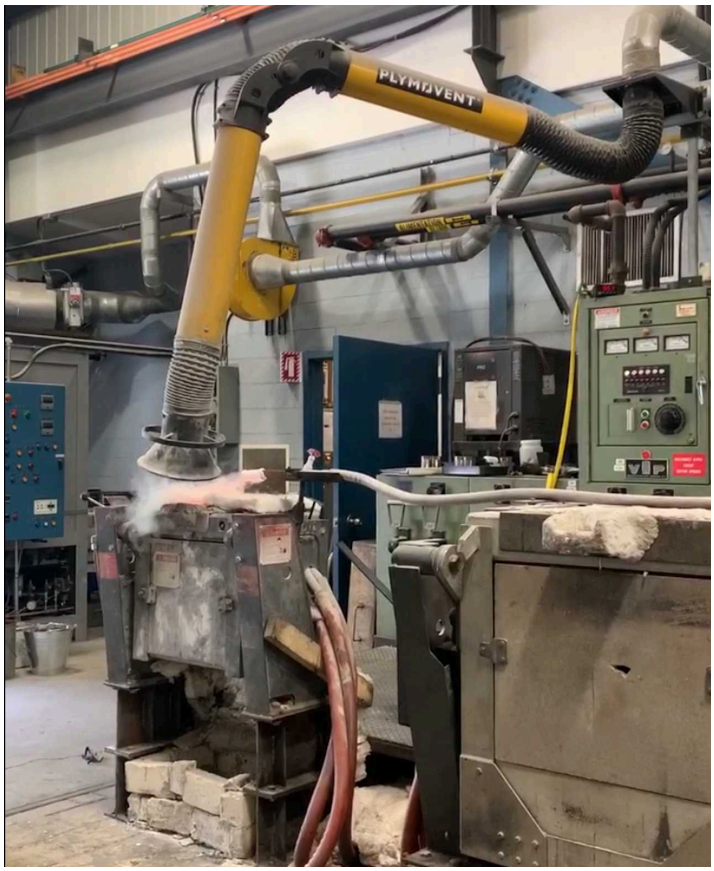

Figure 3.2 Picture of the VIP furnace during a melting process with liquid argon being poured on top of the melt

Mold

The alumina-coated graphite mold presented figure 3.3 was used to produce all the cast billets. This mold has the following specifications: it presents a cylindrical-shape cavity with and internal diameter of 2.25" and a length of 15".

Figure 3.3 Graphite mold leaving the furnace after the pre-heat treatment

3.1.3 Casting procedure

Our team assisted the CMQ technical staff in the operation of both furnaces for the 9 tightly-planned casting days. We carefully supervised each operation and provided support for auxiliary tasks. The delicate operations were performed by the technical staff of the CMQ. The following sub-section presents the complete casting procedure we developed in the first stage of this project. Many iterations were required to obtain this final melting and casting strategy.

Preparation steps

- Preparation of the graphite mold: cleaning, application of a fresh alumina-based coating, and pre-heating (498 °C) in order to remove any humidity and to reduce the

thermal shock during the casting.

- Cleaning of the crucibles.
- Verification of the precision of the balance using its calibration card.
- Weighting of the ingredients to a precision indicated in table 3.2.

3.1.4 Casting steps - CONSARC furnace

The following specific protocol was used for the preparation of the vacuum furnace melting operation:

- The crucible was placed into the furnace heating chamber.
- An extra amount of Fe-Cr master (about 166g) was added at the bottom of the crucible.
- The Fe master, Fe-Cr master, Ni master and Mo were then added into the crucible.
- Manganese (more volatile element according to FactSage calculations) was then placed in a shovel for a later addition into the melt.

When all the preparation of the furnace was completed, the melting operation could be started. It consisted of the following steps:

- The vacuum pump was started; the chamber pressure was decreased up to about 0.06 Torr.
- A heating ramp was performed by increasing the power furnace by increments of 25% of its full power every 45 seconds until it reaches 190kW.
- The Mn master alloy placed in the shovel was added lastly.
- During the addition of these ingredients, the power was increased to ease the melt and then decreased to its optimum value. After the addition was completed, the power was raised to its maximum value for 4 minutes to ensure the formation of an homogeneous melt.
- The furnace power was finally reduced to a minimum value while the preheated mold was filled with the molten alloy.

Casting steps - VIP furnace

The argon-dripping furnace offered more flexibility in its operation. Additions could be made at different strategic times and the operator could skim the melt prior to the casting operation. Here is the specific procedure used for this furnace:

- The Fe master alloy was placed in the crucible.
- The protective pure argon system was mounted on the crucible. Argon was delivered int its liquid form onto the surface of the melt.
- The furnace power was increased until it reached about 100kW. As a consequence, the temperature of the melt was increased up to the target temperature of 1600 °C. In fact, we overshoot to a temperature of about 1700 °C to ensure complete and homogeneous melting.
- The other ingredients were added in the following order: Fe-Cr master, Ni master, Mo and Mn. **Note**: Before adding a new ingredient, it was ensured that the previous ingredient was visually completely melted and well mixed.
- At all time, the furnace power was carefully controlled to guarantee that a temperature higher than the liquidus of the alloy (i.e. 1561 °C) was obtained.
- When it was inferred from the temperature and power readings that the mixture had melted, the temperature was maintained for ten minutes to ensure homogenization of the melt.
- The surface of the melt was skimmed.
- Finally, the melt was poured into the pre-heated mold.

3.1.5 Casting experiment design

Preliminary casts

In the preliminary cast series performed in 2019, two billets were synthesized using the procedure defined previously. We produced one billet for each furnace using virtually the same raw material proportion, aiming at the same bulk composition for both billets. These billets had their elemental composition verified by optical emission spectroscopy. Our analyses showed that their chemical composition (table 3.4) was within the specification limits provided by Hydro-Québec. The oxygen content was quantified by an inert gas fusion analysis. With the

confirmation of these results and thermodynamics simulations it was possible to complete the experiment design.

Table 3.4 Chemical composition (wt.%) and oxygen content (ppm) of each billet obtained from the first cast trial. *Required*: Specification requested by H.-Q.; *expected*: composition predicted from the mass balances

Identif.	**Fe**	**C**	**Cr**	**Ni**	**Mn**	**P**	**S**	**Si**	**Mo**	**O**
Required	Bal.	0.03	11.5-14.0	3.5-5.5	0.5-1.0	0.03	0.03	0.60	0.5-1.0	-
Expected	Bal.	0.01	12.73	4.40	0.90	0.01	0.00	0.14	0.75	-
2019V-I	Bal.	0.01	13.00	5.08	0.95	0.01	0.00	0.14	0.67	290
2019C-I	Bal.	0.02	14.57	5.30	1.05	0.01	0.00	0.12	0.76	95

DOE for the project

The overall strategy of our project was to synthesize more than seven billets made of the 13Cr-4Ni stainless steel with different levels of oxygen contamination. According to our preliminary cast trials, it was concluded that five runs would be performed using the argon-dripping VIP induction furnace since it provided a more flexible approach to reach an accurate bulk composition. Two billets were also produced in the vacuum CONSARC furnace, as presented in the preliminary design of experiment (DOE) presented in table 3.5. It is to be noted that the exact same alumina-coated graphite mold was used for all our casts in order to keep, as much as possible, the same experimental conditions.

Another important consideration we made in the project was to mimic the de-oxidation process of commercial alloys to form more representative inclusions. To do so, we saturated the melt using hematite and then used aluminum as a deoxidizer agent. Therefore the same melting and casting procedures were used at the exception that hematite was added in the melt to increase its oxygen content, which was then reduced by the Al deoxidizer agent.

A second series of casts were performed using the VIP furnace in order to confirm that: 1) the addition of hematite would increase the oxygen content in the melt, and 2) that aluminium would reduce the oxygen content of the melt. From the first five casts, we can see that only one billet reached the targeted specifications, i.e. billet 2020V-II for which we added aluminium. The other bars were out of spec because the added hematite was not pure enough, even if its chemistry was considered in the definition of our mass balances. This led

Table 3.5 Preliminary DOE for the second cast trial showing the addition amount (g) of deoxidizer agent (Al) and pollutant (Fe_2O_3). The expected oxygen content (ppm) for each recipe is also presented

Billet identification	Fe_2O_3 g per Kg of steel	Al g per Kg of steel	Targeted O content ppm
2020V-I	7	0	2000
2020V-II	0	2.5	< 20
2020V-III	7	1	250
2020V-IV	3.5	1	135
2020V-V	3.5	0	500
2020C-I	0	1	< 20
2020C-II	7	0	600

to an alteration of concentration of other elements into the melt.

Thus, the DOE was refined a second time. It was decided to work with similar amounts of aluminium as originally planed in order to reach low oxygen content. Furthermore, a 99,9% hematite material was purchased to solve the problem we faced in the previous casts. Some changes to the DOE were also dynamically made during the casting process as chemical composition and oxygen analyses were being obtained throughout the casting days. The final DOE is presented in table 3.6. The identification of the billets has not been replaced in order to keep the samples traceable, in case of future analyses.

3.1.6 Thermodynamic calculations for the DOE

Thermodynamics simulations were performed using the Equilib module of the FactSage software. The following database selection was made: FactPS (gas phase), FToxid (slag and solid inclusions) and FSstel (melt and intermetallic phases). By considering the chemical composition of the billet identified as 2019V-I and by imposing a system pressure of 1 atm, it was possible to evaluate the liquidus temperature of the alloy to be at 1561.48 °C (using the precipitate target phase feature).

Our thermodynamic calculations also allowed us to generate the graphs presenting 1) the evolution of the oxygen solubility in the melt as a function of temperature (figure 3.4); 2) the

Table 3.6 Final DOE for the second cast trial (after refinement)

Billet identification	Fe_2O_3 g per Kg of steel	Al g per Kg of steel	Targeted O content ppm
2019V-I	-	-	290
2020V-II	0	2.5	< 20
2020V-VI	0	1.5	(unknown: not skimmed)
2020V-VII	0	0.5	250
2020V-VIII	11	0	600
2020V-IX	0	1.5	80
2019C-I	-	-	95
2020C-I	0	1	< 20
2020C-II	7	0	600

oxygen content evolution in the melt as a function of the aluminum addition at a temperature of 1670 °C (figure 3.5); and 3) the effect of the addition of hematite on the solubility in the molten alloy (figure 3.6). From these calculations, we see that we can reach a solubility limit of about 300-800ppm in the range of temperature reached during the operation of both furnaces. We can also see that the addition of aluminum can drastically lower the oxygen content to about 20ppm. We also confirmed with FactSage that hematite (Fe_2O_3) used as a contamination agent would melt. According to our calculations, hematite melts at about 1580 °C which confirms that there will be no problem to dissolve it in the melt.

In order to predict which phases would form during solidification (fast cooling, out-of-equilibrium phases) and after the heat treatment of the billets (reaching a pseudo-equilibrium state), a series of thermodynamic calculations were performed in the range of temperature from 500 °C to 1700 °C. The fundamental understanding of the phases (and their composition) forming in the system (see figure 3.7) allowed us to identify the inclusions to look for during the microstructural characterization of the alloys.

Table 3.7 presents some characteristics of the oxide inclusions that might form during the synthesis process(including the de-oxidation process). These inclusion density data can be compared to the density of CA6NM, which according to Steel Founders' Society of America

[53] is 7.7 g/cm^3 at melting. From this comparison, it is confirmed that all the solid oxide inclusions that would form during the melting process should float to the top of the melt. According to these evidences, the skimming process was therefore of prime importance to remove the inclusions before casting the alloy.

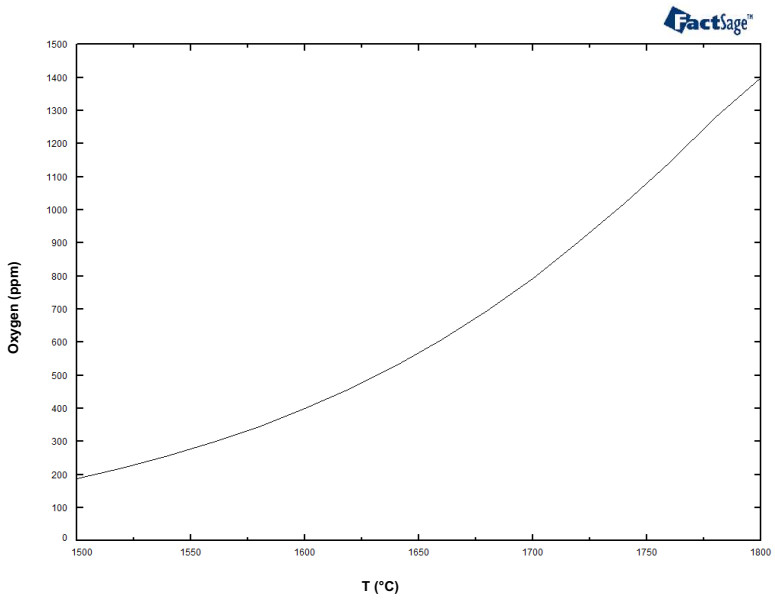

Figure 3.4 Oxygen solubility (ppm) in the melt as a function of temperature at 1 atm

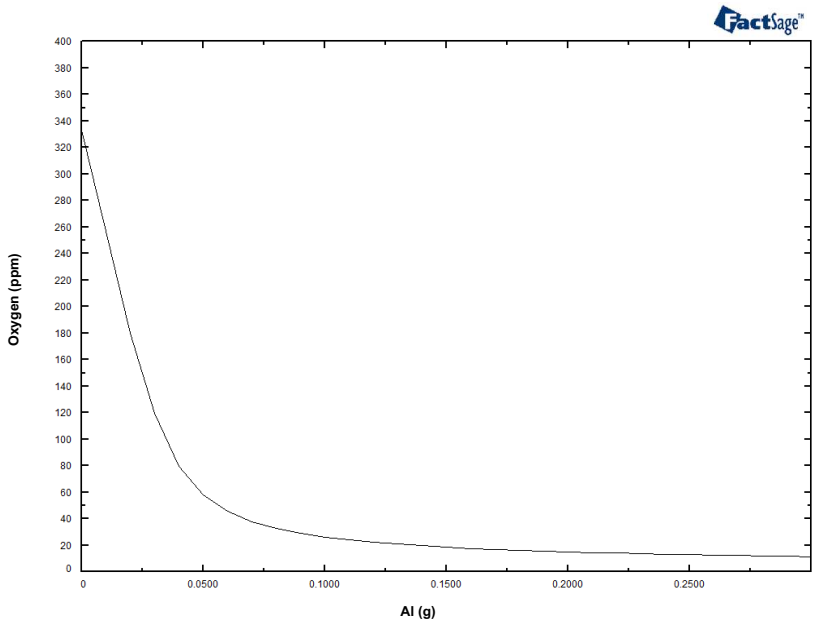

Figure 3.5 Effect of oxygen content (ppm)in the melt as a function of the aluminium addition (g) at 1670 °C (1 atm)

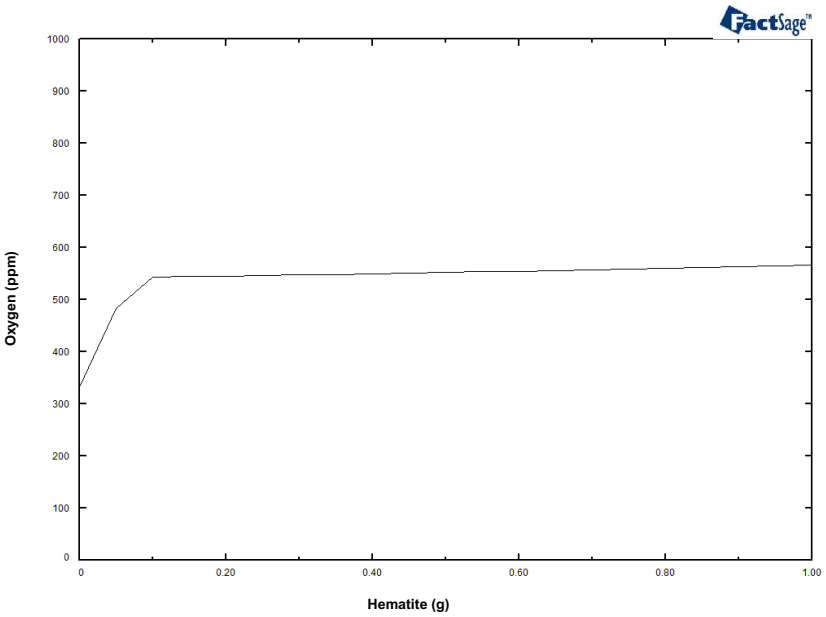

Figure 3.6 Oxygen concentration (ppm) vs the amount of hematite (g) in the melt at 1670 °C (1 atm)

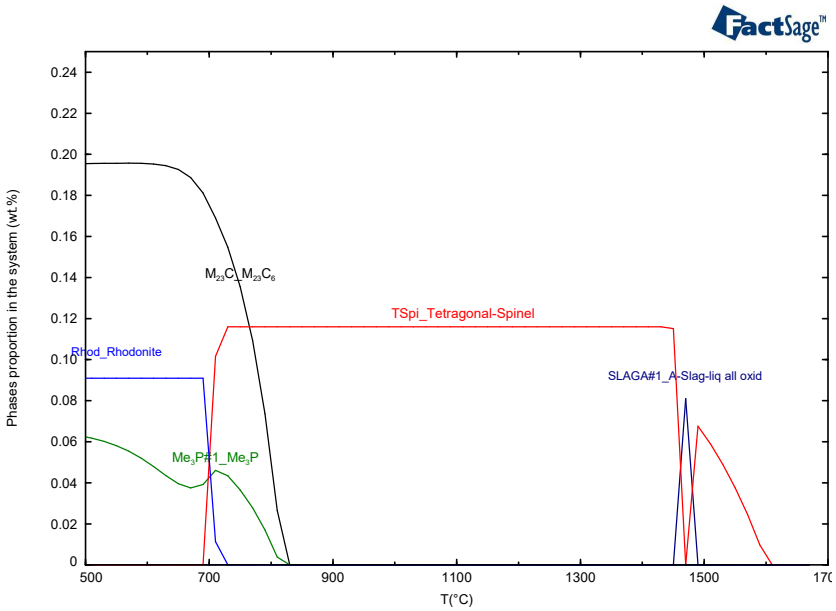

Figure 3.7 Proportion of phases (wt.%) present in the system as function of temperature at 1 atm (BCC and FCC not shown)

Table 3.7 Information of a selection of common metal oxides, adapted from [54].

Oxide	Oxide melting point (^oC)	Density (gcm^{-3})
Al_2O_3	2,072	3.97
Cr_2O_3	2,266	5.21
Fe_3O_4	1,570	5.18
FeO	1,369	5.70
Mn_3O_4	1,564	4.86
NiO	1,984	6.67
SiO_2	1,713	2.30
$3Al_2O_3.2SiO_2$	1,920	3.16
$FeSiO_3$	1,146	3.50

3.2 Samples preparation

Originally, the two 13Cr-4Ni billets obtained from the 2019 cast trials were cut to generate samples from 3 different length positions (see figure 3.8). This strategy was designed in order to verify the chemical and metallurgical homogeneity of the billet. As shown in this figure, six distinct cylindrical-shape samples were created. The microstructure of each sample was analyzed using both optical and scanning electron microscopy (see the samples identified with a yellow star). Six samples were used for hardness measurement. It is to be mentioned that we heat-treated half of these samples while we studied the other half of the samples in their as-cast state. The orange area in figure 3.8 represents the sample that went through the heat treatment. The original observed face of these heat-treated samples can be seen in the other as-cast samples taken from the same length position. Two batches of samples (illustrated with the blue parallelepipeds), containing three specimens each, were machined for v-notch Charpy tests. The first batch was not heat-treated (i.e. as-cast microstructure) while the second was heat-treated according to the procedure presented in this section. Besides that, three samples from other areas (represented with a red star in figure3.8) were extracted for chemical composition and oxygen content analyses.

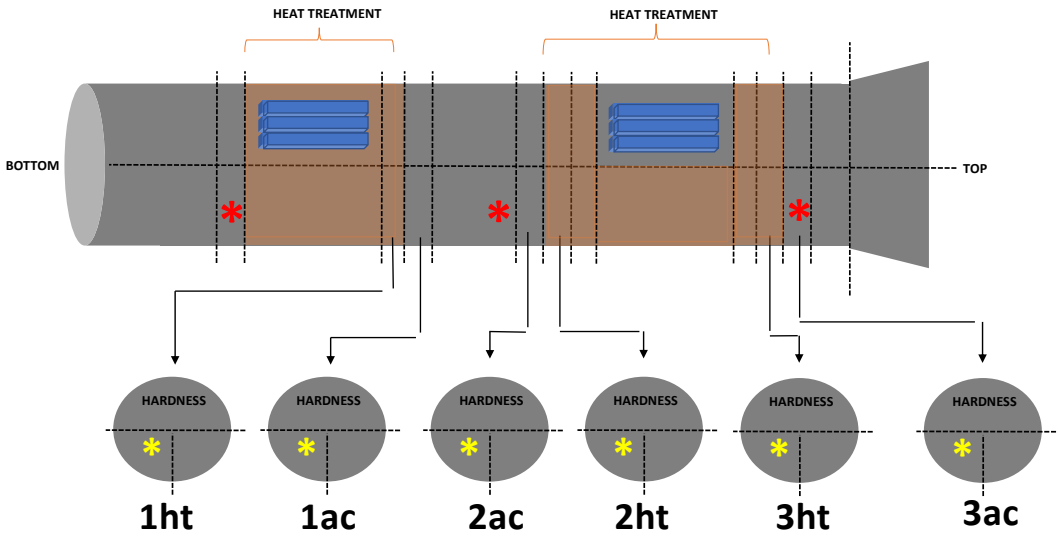

Figure 3.8 Bar cutting representation: billets 2019V-I and 2019C-I

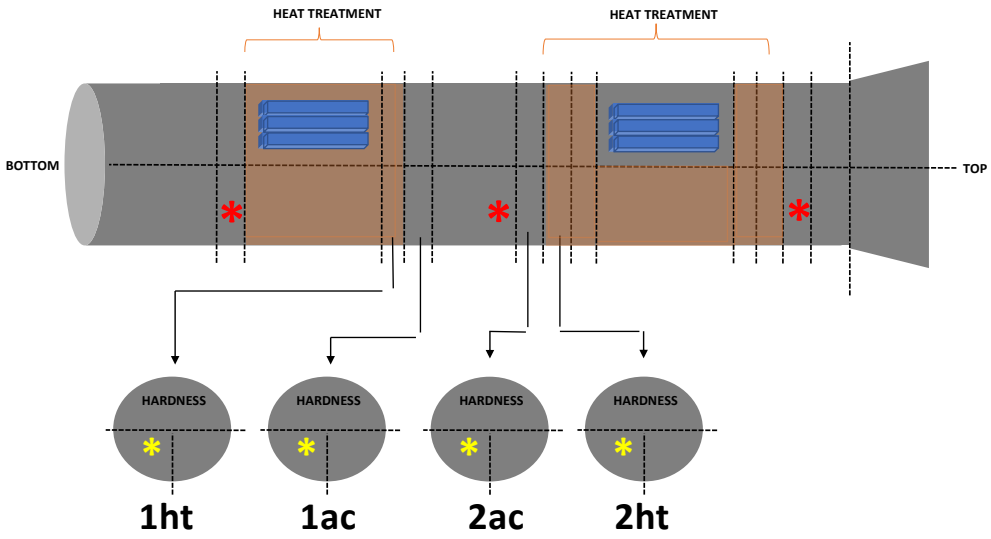

Figure 3.9 Bar cutting representation: billets synthesized in 2020

The subsequent seven cast bars were separated using the same strategy (figure 3.9), however the samples were derived from two different axial positions, instead of three, since the previous results showed a better homogeneity in the center of the bar. All the bars were cut using an abrasive saw with a cooling system, in order to not modified the microstructure with the generated heat during the cut process.

3.2.1 Identification of the billets and samples

The billets were identified using an alpha-numeric code which consists of the year of the cast, followed by the letter V or C, being related to the furnace VIP (V) or CONSARC (C). The number after the dash indicates the chronological order of production (ex.: i.e. 2019V-I was the first billet cast in 2019 in the VIP furnace). As for the sample identification, it is composed of an alpha-number sequence representing the position where the sample was taken and the metallurgical state, i.e. as-cast(as) or heat-treated (ht). As an example, all the samples identified by the code 1ac used for the microstructural characterization are coming from the same length position in each billet and are in their as-cast state. The same is applicable when comparing the hardness, Charpy and chemical composition of our samples. Finally, the commercial samples provided by Hydro-Québec are simply identified as A, B, C and D. They are heat-treated CA6NM specimens coming from different manufacturers.

3.3 Heat treatment

Firstly, the cast billets were cut into smaller samples for further investigations as presented in figure 3.8. Some samples went through a specific heat treatment in order to modulate the microstructure of the steel, following the H.-Q. requirements.

The required heat treatment is defined as a long austenitizing process, followed by a tempering stage, both performed in an air furnace. The duration of each plateau step was imposed by the thickness of the samples, which were below $\leqslant$200 mm. Thermocouples were distributed inside the furnace and in contact with the specimens to ensure a precise temperature reading. The samples were initially placed in the furnace and the temperature was increased using a heating rate of about $\leqslant$30 °C per hour until it reaches 1025$\pm$20 °C. This temperature was held for 8 hours. Next, a slow air cooling was performed until the samples reached room temperature. Before starting the tempering process, the specimens were placed in the furnace and kept for 20 hours in the temperature of $\leqslant$90 °C. Then, a linear heating curve was started respecting the rate of $\leqslant$30 °C/h until a temperature of 615$\pm$15 °C was achieved. This condition was maintained for 8 hours and was followed by a temperature decrease using a cooling rate $\leqslant$50 °C/h to a temperature of 200 °C. When this temperature was reached, the samples were removed from the furnace and set at room temperature, ending the heat treatment process.

3.4 Analysis and mechanical tests

3.4.1 Chemical composition analysis

Regarding the chemical homogeneity of each cast billets, their chemical composition (including oxygen content) was obtained at different distinct axial positions (figures 3.8 and 3.9). The analyses were performed at the CMQ using the optical emission spectroscopy [55] for determining the alloy elemental composition and an inert gas fusion [56] technique for oxygen quantification.

3.4.2 Metallography

A total of more than 40 samples were extracted from the cast billets, prepared, polished, etched and characterized at the microscope. Four samples coming from the commercial alloys received from H.-Q. were also prepared.

All the samples were mounted in conductive Bakelite, ground and polished in an automatic grinding/polishing machine using a load of 27 N per specimen. The surface preparation and

polishing process consisted of mainly four stages: grinding using a 120[P120] grit SiC paper with water cooled (step 1), polishing with polycrystalline diamond solution 9μm (step 2) and 3μm (step 3), followed by a final polish alumina suspension (0.05μm) (step 4), resulting a mirror finish surface. Between each step, samples were washed and cleaned with hand soap and water. This ensured that any particle from the previous step would be removed and would not contaminate the next polishing step. At the end of the procedure, the samples were placed in an ultrasonic ethanol bath for 5 minutes in order to remove any residue coming from the polishing solutions. The samples were then quickly dried with compressed air. More detailed information about the grinding and polishing method can be found in the table 3.8.

Table 3.8 Polishing methodology using Buehler's consumables

Surface	Abrasive	Base speed (rpm)	Relative rotation	Time (min)
CarbiMet	120 grit (P120) SiC water cooled	300		Until plane
UltraPad	9μm MetaDi Supreme Diamond	150		5:00
TriDent	3μm MetaDi Supreme Diamond	150		3:00
ChemoMet	0.05μm MasterPrep Alumina	150		2:00
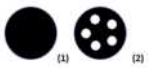	1:Platen 2:Specimen holder			

Sample etching

In order to reveal the microstructure of the as-cast and heat-treated 13Cr-4Ni stainless steel, some samples were etched. Etching was performed using the Viella's reagent [57] (1g of picric acid, 5ml HCl and 100 ml of ethanol) for approximately 40 seconds, at room temperature. This etching solution was suggested by H.-Q.. Preliminary tests with a different etching solution did not clearly reveal the microstructure. The specimens were observed in the optical microscope and pictured at 100x magnification.

Inclusion analysis

The inclusion characterization of our samples included an in-depth optical microscopy analysis. A total of 44 surfaces were photographed as polished at 100x magnification using the 2D stitch function of the Keyence optical microscope. This software reconstitutes the entire metallographic sample surface by stitching several pictures of the specimen. The focus was set using the automode option of the microscope at medium range. As graphically shown in figure 3.11, the picture represents the entire surface of the specimen, allowing the observation of the complete radius distance, from the center to the border. These pictures were scanned by another team member using the software ImageJ. This colleague performed the particle analysis using a code he developed. This customized code can locate and identify each particle with a Feret diameter >20μm. This Python code is also able to exclude all the undesirable features that are not inclusions, such as shrinkage defects, porosities, dust, scratches and other artifacts. Black objects with blurry contours that appeared featureless were classified as porosities (figure 3.10 left), whereas objects with that appeared grayish were classified as inclusions (figure 3.10, right). The inclusions statistical analysis was performed using this customized-tool as well.

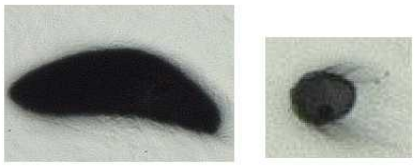

Figure 3.10 Typical porosity (left) and inclusions (right). The objects are not to scale, the left one has an approximate width of 200μm and the inclusion on the right an approximate diameter of 30μm

The characterization of the inclusions was done by the observation of two samples per bar (one heat-treated and one as-cast) through scanning electron microscope (SEM) and energy dispersive X-ray spectroscopy (EDS). The samples were examined as polished with different magnifications in order to check the morphology and chemical composition of the inclusions. The commercial samples were also analyzed.

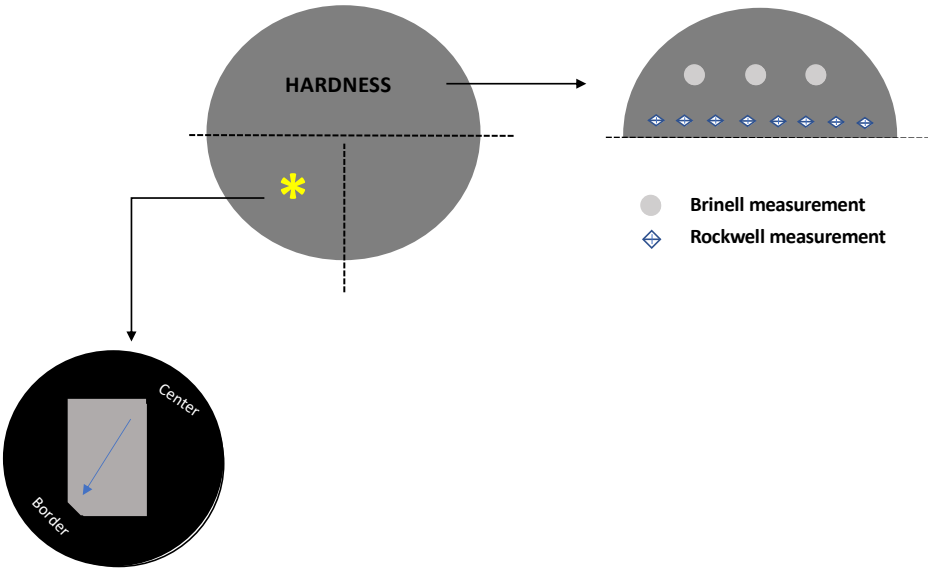

Figure 3.11 Non-scale graphical representation of the specimen analyzed area for the metallography observations (left) and hardness measurements (right)

3.4.3 Charpy

Notch-toughness Charpy tests were performed in batches of 3 specimens. Each batch was coming from a different billet in both as-cast and heat-treated states. The samples were machined following the ASTM standard [58] with the geometrical specifications presented in figure 3.12. The Charpy tests were performed at 0 °C, as requested by H.-Q., with a speed of the pendulum at the impact moment of 5.234 m/s and a maximum impact energy of 300J. The experiments were performed at IREQ by their technician.

The fractured surfaces were observed and analyzed in order to define the type of failure (i.e. brittle or ductile) they experienced.

3.4.4 Hardness

More than 40 specimens were taken from the cast billets to investigate their hardness. Four commercial samples were also studied. The samples were coming from at least two axial positions (figures 3.8 and 3.9) and were analyzed in their as-cast and heat-treated states. The surface of the samples was prepared by a sequence of manual grinding with a SiC paper (120 and 240 grit) at 150 rpm. This step was required to ensure that the two parallels surfaces

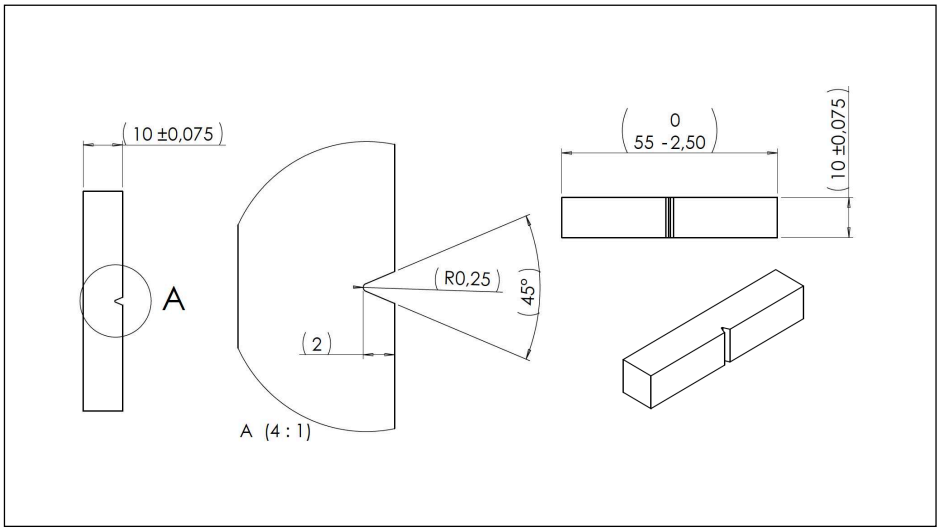

Figure 3.12 Charpy specimen geometrical specifications in mm provided by IREQ

did not present scratches that could alter the measurements. For the heat-treated samples, it was necessary to firstly remove the exposed-surface to heat treatment using a grinding with the SiC paper 60 grit.

The specimens were analyzed through the Rockwell C method [59]. One primary objective of this hardness study was to see if a hardness gradient has been established from the center to edge of the billet. Since the indentor is small in such a hardness measurement, it has been possible to perform 8 measurements per sample as showed in figure 3.11. The samples were also studied using the Brinell method (3000kgf - 10mm) [60], as required by the ASTM standard for this material.

3.4.5 Summary of the experimental activities

Table 3.8 presents a summary of the experiments performed during the course of this project. It provides the number of analyzed samples and the number of measurements performed for each specimen. This table also shows who performed each experiment. All the samples were machined by the student with the exception of the Charpy specimens.

Table 3.9 Summary of the experimental activities performed in the project

Activity	Number of samples	Number of measurements	Performed by
Chemical composition analysis	24	minimum 3	CMQ
Polishing	44	-	the student
Etching	44	-	the student
Optical microscopy verification	44	-	the student
Inclusions quantification	44	-	Simon Riverin
Inclusions characterization (SEM/EDS)	22	-	the student
Charpy	18	3	IREQ
Hardness (Brinell)	40	3	the student
Hardness (Rockwell C)	44	8	the student

CHAPTER 4 RESULTS AND DISCUSSIONS

4.1 As-cast synthesized billets

A total of nine 13Cr-4Ni billets with different level of oxygen were synthesized using the final DOE (see table 3.6). These billets were characterized and tested using the procedure described in the previous chapter. The fine-tuning adjustment of the chemistry of each stainless steel melt was performed so the compositions shown in table 4.2 could be obtained. To reach these compositions, extra additives consisting of aluminum (deoxidizer) and hematite (polluting compound) were used. These extra additives were introduced in proportions that are presented in table 4.1. The added masses are expressed in this table in relative weight percentage of the total weight of the melt.

Table 4.1 Cast details corresponding additional ingredients (wt.%)

Identif.	**Modification in synthesis recipe**
2019V-I	reference bulk composition
2020V-II	addition of 0.25 wt.% Al
2020V-VI	addition of 0.15 wt.% Al (not skimmed)
2020V-VII	addition 0.05wt.% Al
2020V-VIII	addition of 1.08 wt.% Fe_2O_3
2020V-IX	addition of 0.15wt.% Al
2019C-I	reference bulk composition
2020C-I	addition 0.10 wt.% Al
2020C-II	addition 0.69 wt.% Fe_2O_3

4.2 Elemental composition analysis

The bulk chemical composition of each billet is presented in table 4.2. We also reported in this table the required chemical composition as provided by H.-Q as well as the expected chemical composition that should be obtained using our mass balance calculations. We also

provided at the end of this table the chemical analysis of the commercial samples which were used as reference materials for the microstructure characterization and hardness.

We can see from this table that the billet synthesized in the argon-dripping VIP furnace during the first cast series (i.e. 2019V-I) presented only slight variations from the expected elemental compositions. In fact, the nominal composition felt within the requested limits for all the elements. On the other hand, the billet synthesized in the vacuum CONSARC furnace from this 2019 cast series (i.e. sample 2019C-I) presented a higher chromium content. This can be explained by the extra amount of Fe-Cr master alloy deliberately added at the bottom of the crucible (since we thought there would be a partial solidification / lack of fusion at the water-cooled crucible interface). The Mn concentration of this billet was also slightly above the maximum limit. We originally expected (from our thermodynamic calculations) that some Mn loss would occurred by evaporation during the synthesis, as the Mn vapor pressure was significant at the operating temperature of the furnace. These preliminary results show that the melting process under vacuum would have required a kinetic model coupled to our thermodynamic calculations to better predict the Mn losses by evaporation. We therefore decided after this first trial not to add any extra Mn.

We can also see from this table that the 2020V-VI billet was out of spec in terms of carbon concentration. During this alloy synthesis, some aluminium was added to lower the oxygen content and the melt was deliberately not skimmed prior to the casting. Even without the slag removal prior to the casting, this billet presented a low oxygen content which implies that the slag was not transferred to the mould during the casting. Another important observation from this table can be made for the 2020V-VIII billet. We can see that this billet has a chromium content below the desired value. This low concentration can be related to the addition of hematite in the melt, which resulted in the formation of some chromium oxides which were then removed in the slag phase prior to the casting. The same phenomenon can be expected for Mo, which explains its low concentration in this billet when compared to the other cast samples. The same effect was observed for the bar 2020C-II, in which was also added hematite.

Overall, the reached chemical composition of all our billets are more than satisfactory. This is a strong evidence of the good technical operation of the furnaces by the CMQ staff. It has to be remembered that the very low carbon concentration was one of the major constraints imposed by our industrial partner. Using our synthesis approach (adequate selection of raw materials - master alloys), we were able to obtain cast billets with carbon contents lower than the commercial samples (at the exception of the 2020V-VI billet). We also noticed that all the synthesized specimens showed a higher content of Ni, Mn and Mo when compared to the

reference samples. Finally, we can see that the silicon content of the synthesized billets was inferior to the concentration in the reference materials.

Note: The results related to the commercial sample are presented with a different precision because the chemical compositions were obtained from a previous study performed at IREQ. The oxygen content of these samples were quantified in this study.

Table 4.2 Chemical composition (wt.%) and oxygen content (ppm) of all the synthesized billets and commercial samples. Required is the specification requested by H.-Q. and the expected is the composition predicted from the mass balance

Identif.	**Fe**	**C**	**Cr**	**Ni**	**Mn**	**P**	**S**	**Si**	**Mo**	**O**
Required	Bal.	0.03	11.5-14.0	3.5-5.5	0.5-1.0	0.03	0.03	0.60	0.5-1.0	-
Expected	Bal.	0.01	12.73	4.40	0.90	0.01	0.00	0.14	0.75	-
2019V-I	Bal.	0.01	13.00	5.08	0.95	0.01	0.00	0.14	0.67	290
2020V-II	Bal.	0.02	13.17	4.49	0.90	0.01	0.00	0.11	0.65	37
2020V-VI	Bal.	0.05	13.16	5.09	0.91	0.01	0.00	0.09	0.71	69
2020V-VII	Bal.	0.01	12.15	4.64	0.85	0.01	0.00	0.09	0.65	289
2020V-VIII	Bal.	0.01	11.33	4.72	0.82	0.01	0.00	0.05	0.64	358
2020V-IX	Bal.	0.01	12.28	4.73	0.94	0.01	0.00	0.08	0.66	193
2019C-I	Bal.	0.02	14.57	5.30	1.05	0.01	0.00	0.12	0.76	95
2020C-I	Bal.	0.01	12.54	4.62	0.70	0.01	0.00	0.03	0.78	22
2020C-II	Bal.	0.004	12.25	4.47	0.55	0.01	0.00	0.05	0.67	118
Commercial Samples										
A and D	Bal.	0.016	12.79	3.49	0.5	0.019	0.007	0.26	0.55	130
B	Bal.	0.013	13.1	4.3	0.83	0.026	0.002	0.65	0.51	54
C	Bal.	0.02	13.6	4.1	0.58	0.019	0.0025	0.41	0.61	34

4.3 General microstructure analysis

The figure 4.1 presents the microstructure of the heat-treated samples synthesized in the argon-dripping VIP furnace. Each panel represents a specific billet which is clearly identified.

The specimens produced in the vacuum CONSARC furnace are shown in figure 4.2. Four commercial samples provided by Hydro-Québec are also presented in figure 4.3.

In general, it is possible from these metallographies to confirm the major presence of martensitic structures characterized by blocks of martensite laths inside what used to be austenite equiaxed grains. A heat-treated sample taken from the 2020V-6 billet shows a good reveal of the microstrucure after the chemical attack and is presented in figure 4.4. It is possible to observe the prior austenite grain boundaries as indicated by the arrows. As a result of the heat treatment tempering, these tempered martensite structures should also present some reformed austenite. However, the austenite phase is so thin that it needs to be observed through SEM in higher magnifications. It is to be noted that the etched samples did not clearly reveal the microstructure in many cases, even though the recommended solution for this stainless steel grade was used. This is believed to be due to the elapsed time between the sample polishing and its chemical attack. It is also possible to note the presence of polishing artefacts in some samples such as 2019V-I, 2020V-II, 2019C-I and the commercial samples A and B.

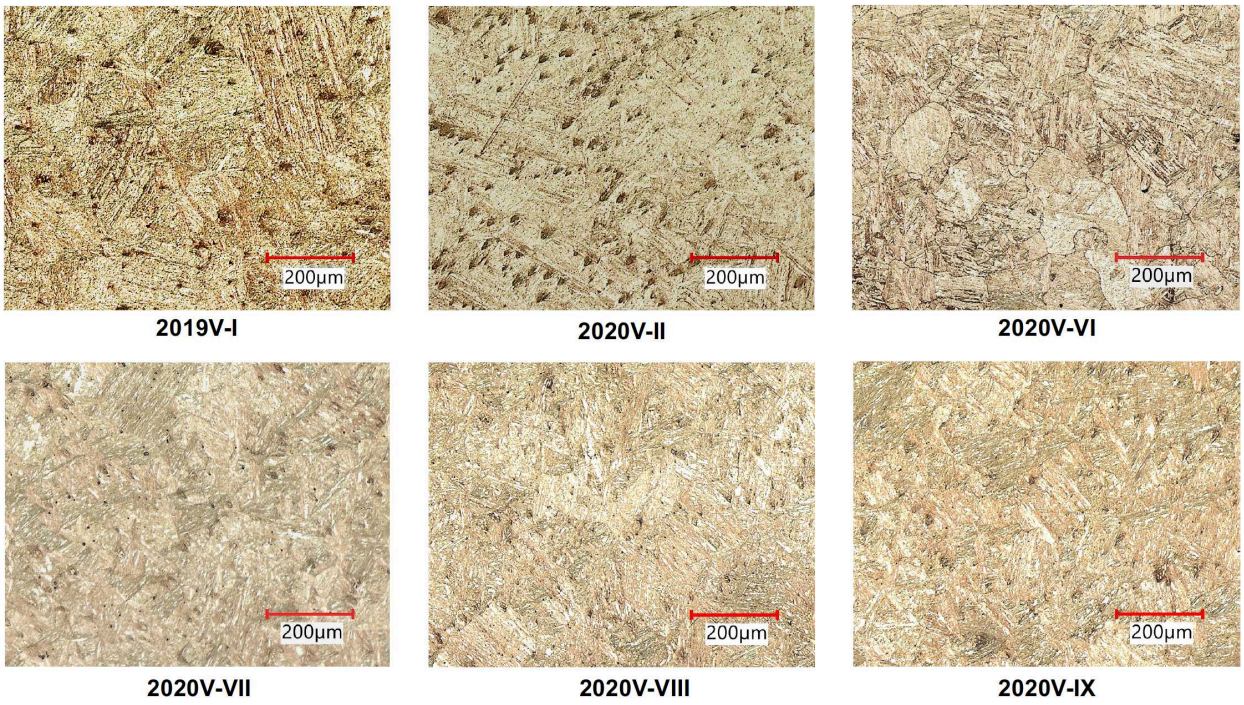

Figure 4.1 Optical micrographs of heat-treated samples (magnification 100x) - billets synthesized in the VIP furnace

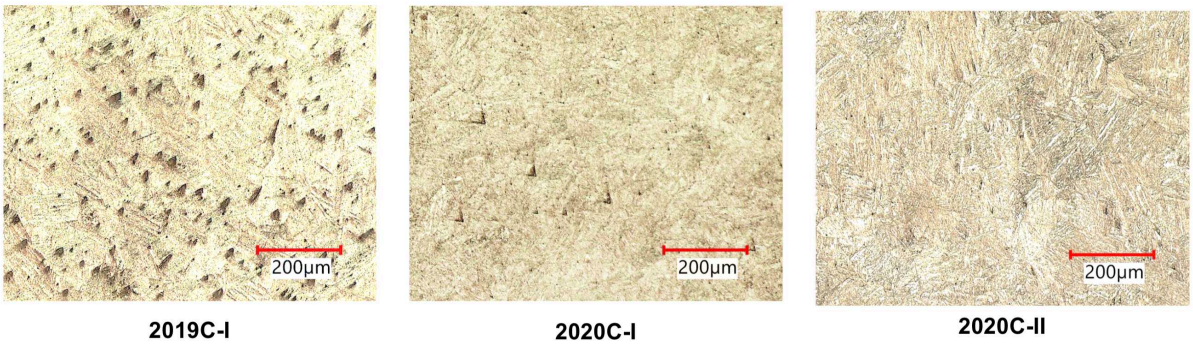

Figure 4.2 Optical micrographs of heat-treated samples (magnification 100x) - billets synthesized in the CONSARC furnace

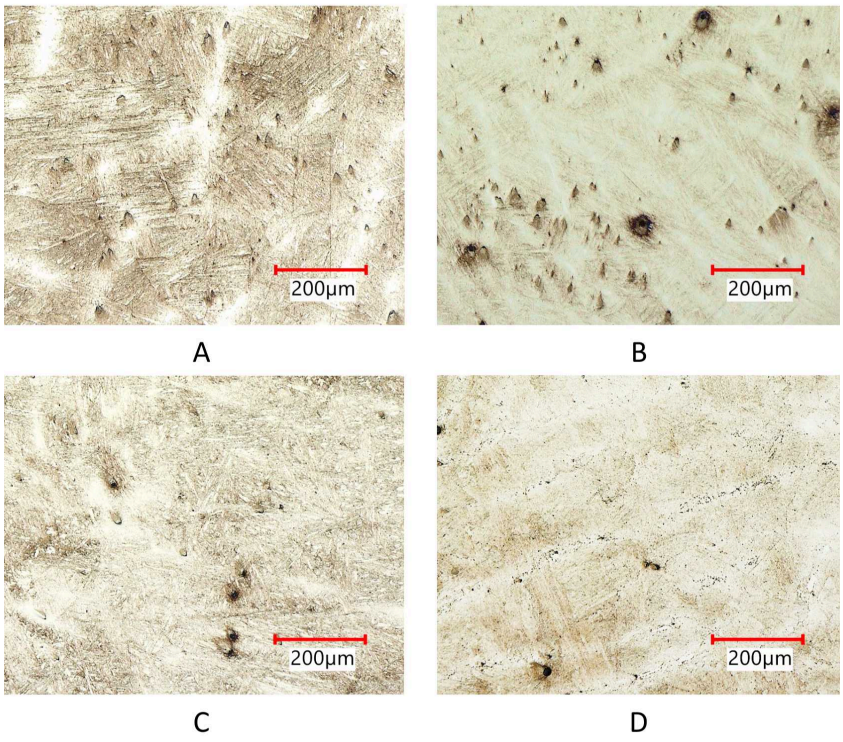

Figure 4.3 Optical micrographs of commercial samples (magnification 100x)

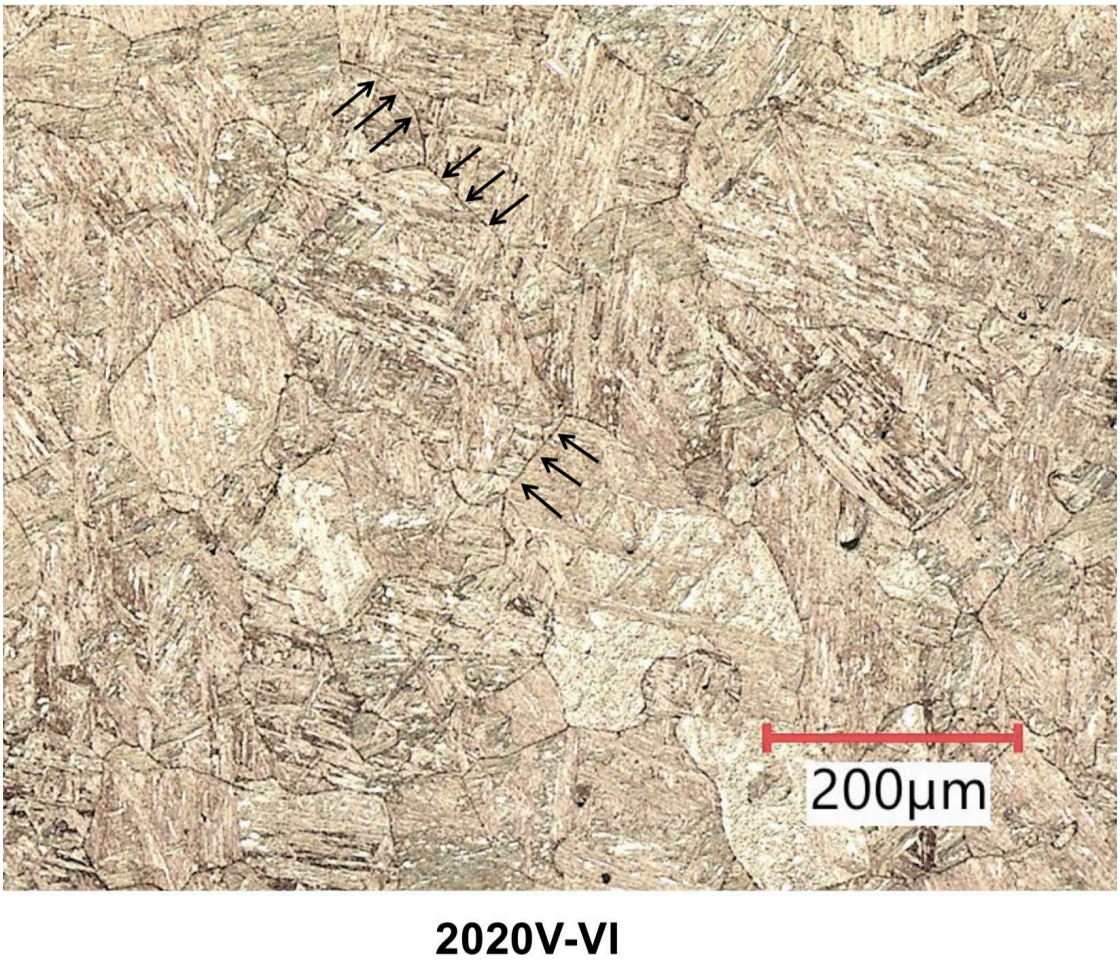

Figure 4.4 Optical micrograph from billet 2020V-VI (magnification 100x)

Density of inclusions

It is clear that the density, shape, composition and size of the inclusions present in the stainless steel alloy will impact its mechanical performance (such as the fatigue behavior). Inclusions have a different hardness range when compared to the matrix, are typically brittle, can act as stress concentration sites and may induce chemical heterogeneities.

Figure 4.5 shows the total inclusion density for all the as-cast samples. The dark grey columns represent the total area occupied by all the inclusions (per unit of observed area) while the light grey columns show the number of inclusions per mm^2. The amplitude of both indicators should be read on the left y-axis. The blue dots (followed by a number) provide the oxygen content which can be read the right y-axis.

The x-axis shows the identification of each measured samples. There are two pairs of results

per cast billet (representing two samples from the same billet with different axial positions).

The samples are identified using the convention detailed in the subsection 3.2.1 and also shown in figure 3.9. The 12 pairs of columns on the left of this graph are samples synthesized in the VIP furnace (underlined in red) while the 6 pairs of columns on the right present the measurements done for the samples synthesized in the CONSARC furnace (underlined in green).

When comparing the billets obtained from the two different furnaces, we can see in both cases that the melt made with the reference bulk composition (2019V-I and 2019C-I) presented a higher density of inclusions when compared with the billets for which aluminum was added. These melts were saturated in oxygen, which ultimately resulted in a higher inclusion content. There is a correlation in this graph between the oxygen content of the sample and the inclusion density for a given furnace. The scattering may be explained by the difficulty in measuring the oxygen content (coupled to the small number of expensive analyses that could be performed), as well as the potential heterogeneity of the billets. This heterogeneity within a billet is partially proven by the differences observed in this figure when comparing samples of a given billet obtained from two distinct length positions. We see for most samples a tendency of a reducing number of inclusions in the second analyzed position which is at the edge of the bar, closer to the top. This behavior is observed for most of bars at the exception of the 2019V-I and 2019C-I billets.

When analyzing the ratio between the number of inclusions and the area density, we can see from this figure that it is mostly constant for each sample of the same bar. This observation implies that the size of the inclusions are similar in a given billet. However, when comparing the different bars, we can see that these ratios greatly differ, which is a clear indication that there is a change in the size and shape of the inclusions as a function of the bulk composition of the bar and its oxygen content.

Figure 4.6 presents the same types of data, but this time for the heat-treated samples. The same chart layout is kept. It can be noted from this figure that there is an increase in the number of inclusions in most of the samples synthesized in the VIP furnace after the heat treatment. It implies that these inclusions are precipitating during the heat treatment. The opposite observation can be made for the samples that were synthesized under vacuum in the CONSARC furnace. In this case, it may be possible that the inclusions obtained from the melt were meta-stables and partially dissolved upon the heat treatment. It also seems for the CONSARC samples that the density of inclusions is more correlated with the oxygen content of the sample.

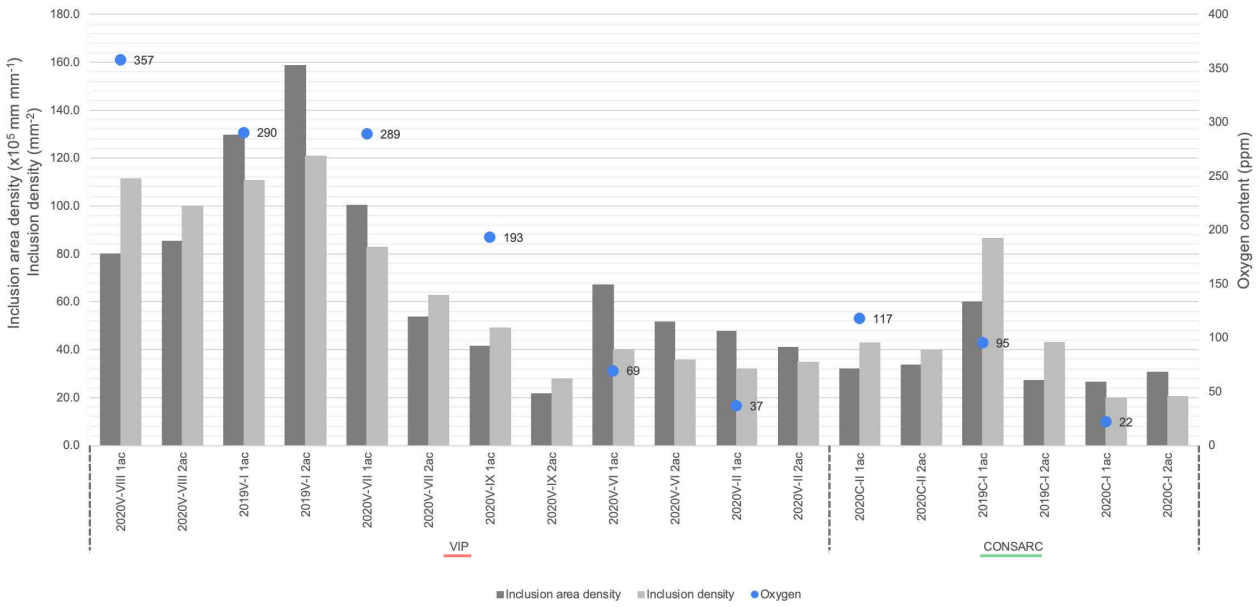

Figure 4.5 Inclusion density and inclusion area density vs oxygen content, being accounted two samples per bar (different length positions) in the condition **as-cast**

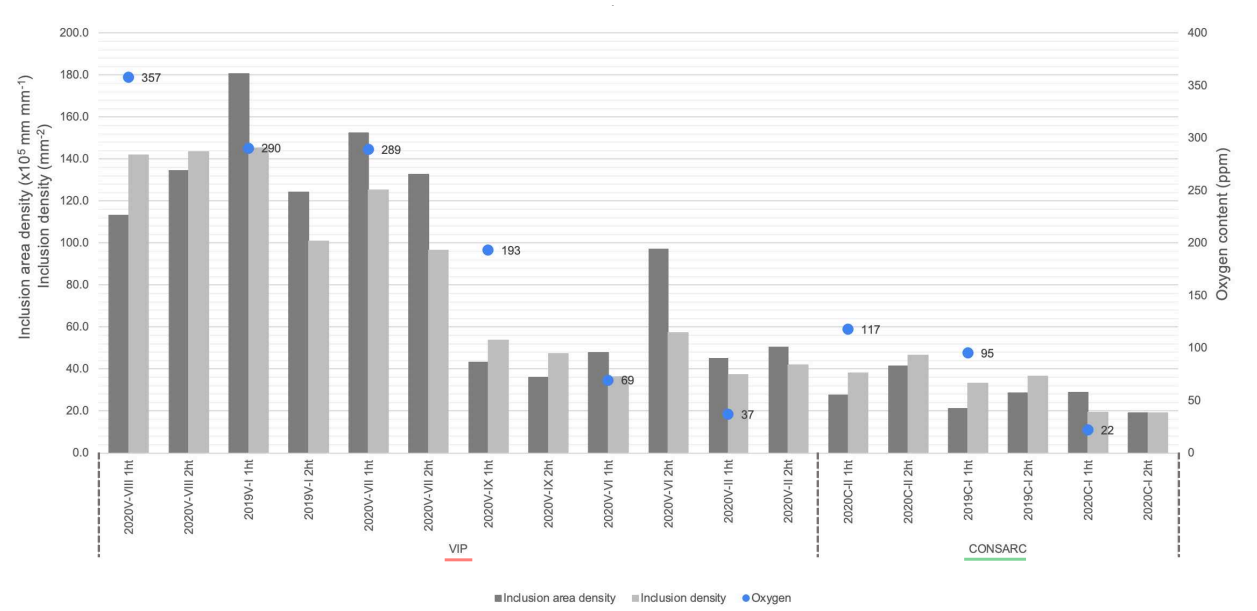

Figure 4.6 Inclusion density and inclusion area density vs oxygen content, being accounted two samples per bar (different length positions) in the condition **heat-treated**

The graph presented in figure 4.7 shows the average of two different length position samples (heat-treated state) for each billet. The greyer columns represent the inclusion area density, followed by the inclusion counts density columns which are colored in light grey. Both scales

are read in the left y-axis. The y-axis on the right indicates the oxygen concentration which is provided by the blue dots. The x-axis gives the billet identification as well as complementary information regarding the melt synthesis. The first set of data on the left are related to the VIP furnace, followed by the results obtained from the CONSARC furnace and the one obtained for the commercial alloys on the far right, underlined in yellow. As seen from this figure, only one specimen for each commercial sample was analyzed.

A striking feature can be seen on this figure when looking at the ratio of the number of inclusions and area density obtained for the commercial samples. Whereas the count of inclusions is small, the surface of the inclusions are significantly higher than for the synthetic samples which resulted in a substantially larger ratio when compared to our synthesized samples. This is most probably caused by the different melting conditions and alloying practices when compared to our protocol which lead to larger inclusions in the commercial alloy.

Also, the total inclusion area density is considerably greater for the 2020V-VIII, 2019V-I and 2020V-VII casts, which are also the billets with the higher content of oxygen. The billet labeled as 2020V-VI, which was not skimmed, presents a similar quantity of inclusions combined to a higher inclusions area density when compared to the 2020V-IX billet (which was skimmed) indicating that the inclusions were bigger in the former.

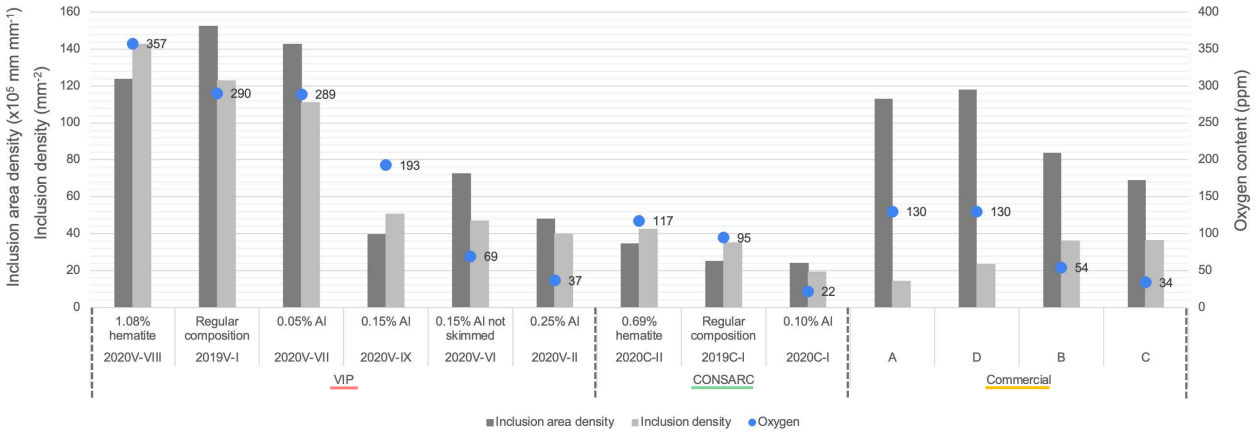

Figure 4.7 Inclusion density and inclusion area density vs oxygen content, being accounted the mean of two samples per bar (different length positions) in the condition **heat-treated** and one specimen of each commercial sample

Looking at the size distribution of inclusions, figure 4.8 shows the Kernel density estimation of inclusion counts as a function of their characteristic size. In this figure, the inclusion

distribution as a function of the Feret diameter (which represents the maximum dimension of the inclusion) is presented for the 9 cast billets, considering 2 different axial position for the as-cast and heat-treated specimens. The dashed lines represent the as-cast samples and the continuous lines are associated to the thermally heat-treated samples. The different colors indicate the position (orange line = samples closer to the top of the bar - surface of the mould; blue line = sample located closer to the bottom of the billet).

By comparing these lines, the effect of the position and heat treatment can be revealed. Firstly, most inclusion distributions are nearly identical for two distinct positions of the same billet. In few cases, samples taken at the top of the billet contains more inclusions. This may be explained by inclusion entrainment at the end of the casting operation and by their low density which favors their displacement toward the surface. In other cases, it is the opposite. Because of that, no definite trend can be inferred from these data.

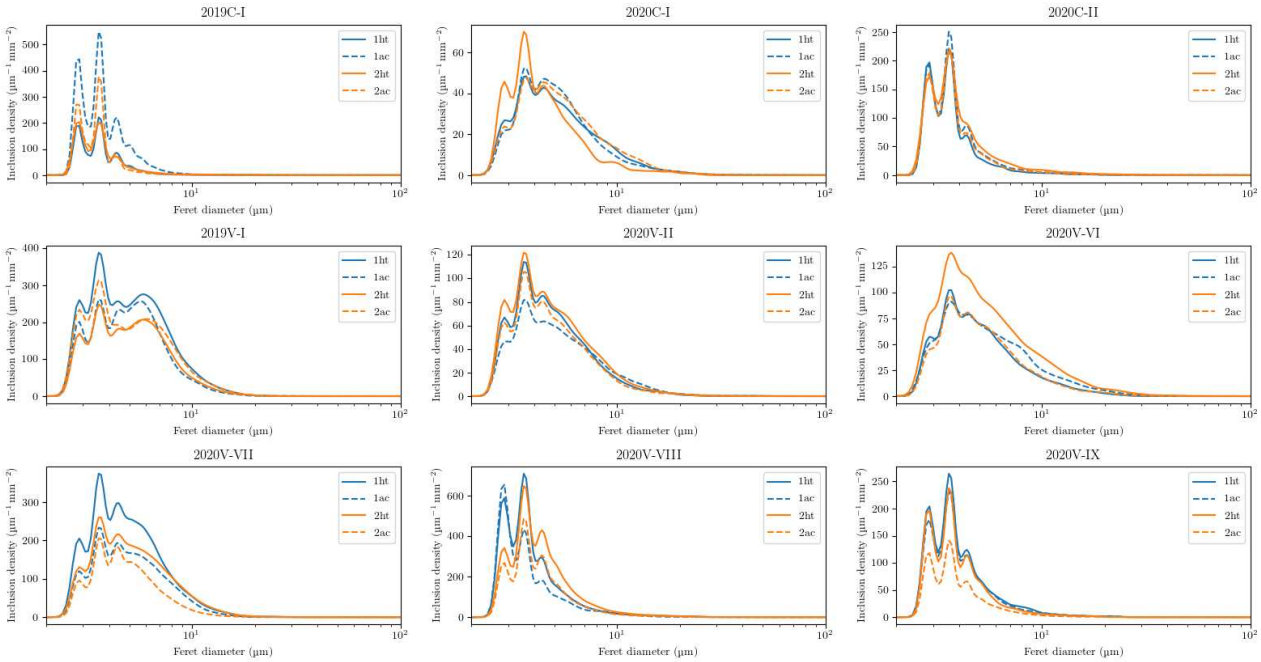

Figure 4.8 Inclusion count density vs Feret diameter, each graph accounts for 2 as-cast and 2 heat-treated samples per bar

Figure 4.9 presents Kernel density plots showing the distribution of total inclusion area as a function of their Feret diameter. These curves were obtained by weighting the area of each inclusion. The same label and axis layout as for figure 4.8 were used. Data from the nine cast billets in both their heat-treated and as-cast-samples for two distinct length positions were used to generate this figure. The area density distributions seem to follow a specific

trend which is independent of the position or the thermal history of the sample. For example, samples from the 2020C-2 billet all have a peak area density around 3-4 microns which is independent of the heat treatment and the length position of the sample. In some cases, one of the four curves is significantly different from the others, as seen for example in the 2019C-I distributions. This may be due to differences in polishing, cleaning, photography and image analysis.

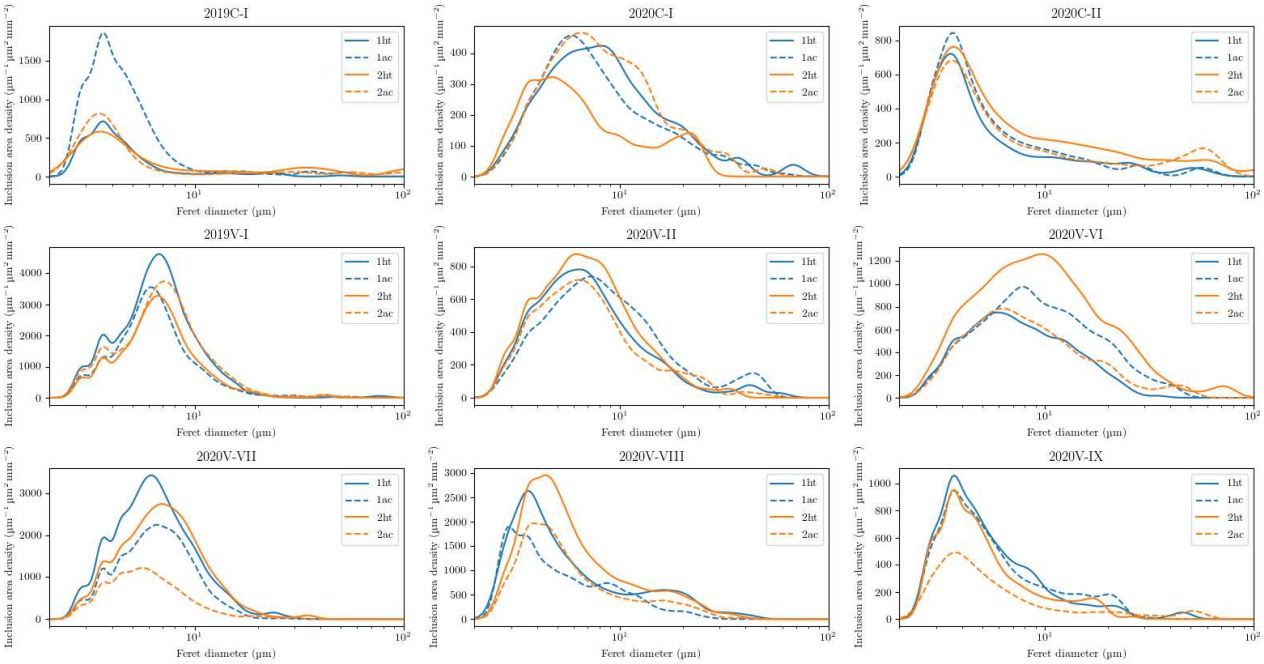

Figure 4.9 Inclusion area density vs Feret diameter, each graph accounts for 2 as-cast and 2 heat-treated samples per bar

Figure 4.10 was obtained by averaging the two as-cast samples for each billet. This allowed to summarize all the information presented in both figures 4.8 and 4.9. A comparison between each bar taking into account the inclusion count is presented on the left panel while the right panel presents a similar comparison for the inclusion area. Similar graphs are presented in Figure 4.11 for the heat-treated samples.

It can be seen from these figures that there is an increase in the number of inclusions with similar Feret diameter in the heat-treated samples. This is potentially explained by an inclusion coalescence phenomenon promoted by the energy transferred to the sample during the heat treatment. When comparing the various curves obtained under the same conditions, we see similar trends. This implies that specific types of inclusions are forming, this can also be seen in the figure 4.8 where it shows the similarity between the curves of different samples

in the same bar. We can also identify the larger inclusions that are present in these bars by observing the location of the tail thinning of these distributions. The graphs on the right panel of these figures reveal that the bigger inclusions contributed more to the total inclusion area than the smaller inclusions. Moreover these larger inclusions are fewer than the smaller ones. For example the most important contributors to the total inclusion area are the large inclusions between 5-10 microns for the 2019V-I and 2020V-VII billets.

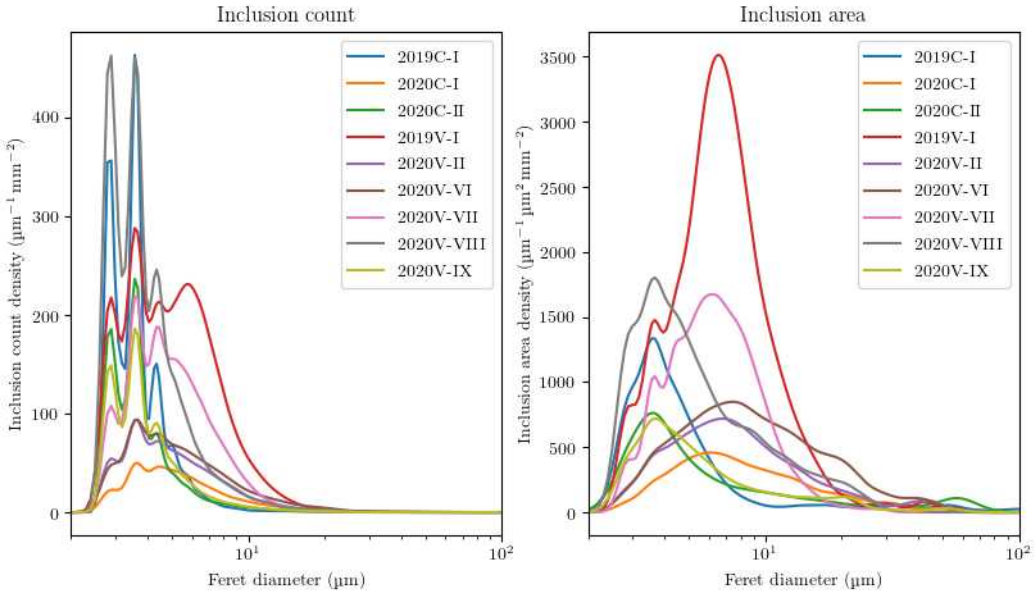

Figure 4.10 Inclusion count density (on the left) and inclusion area density (right) both vs Feret diameter. Being considered the mean of the two **as-cast** samples per bar

A similar analysis with the commercial samples is represented in figure 4.12. These graphs show that the inclusion density is considerably lower for these commercial alloys than for most of the synthesized samples (see the comparison with figure 4.11). On the other hand, the inclusion areas are significantly larger for the commercial alloys, confirming the information obtained from figure 4.7.

Finally, figures 4.13 and 4.14 show the distribution of the square root of area parameter for the heat-treated specimens and commercial samples, respectively. The square root of area parameter considers the side of a square having an equivalent area as the inclusion, which is often used for fatigue life estimation. The distributions are also Kernel density plots. They are normalized such that the total areas under the curve are equivalent to the inclusion density as shown in figure 4.7.

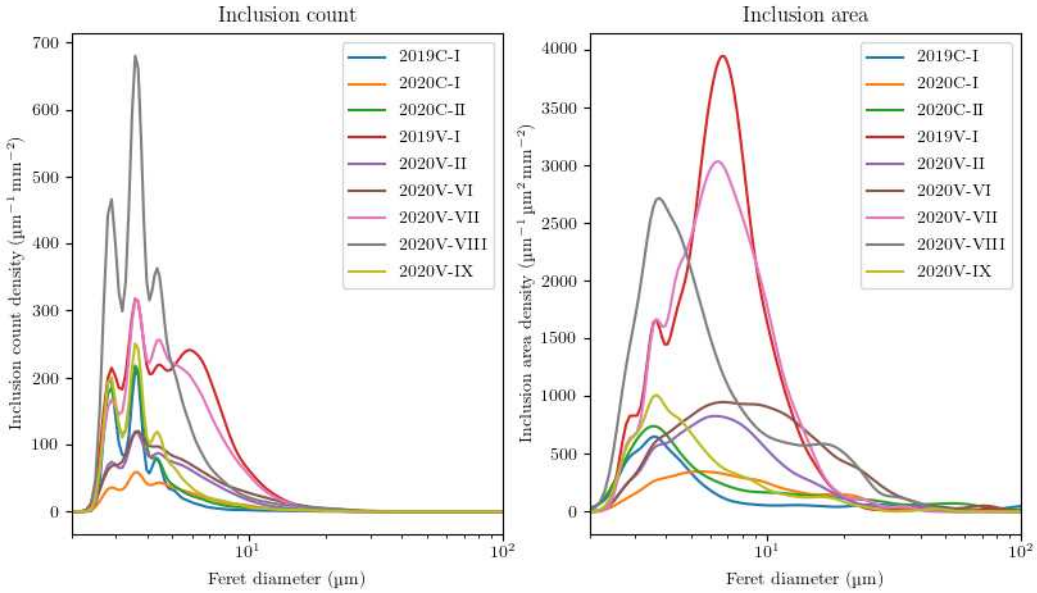

Figure 4.11 Inclusion count density (on the left) and inclusion area density (right) both vs Feret diameter. Being considered the mean of the two **heat-treated samples** per bar

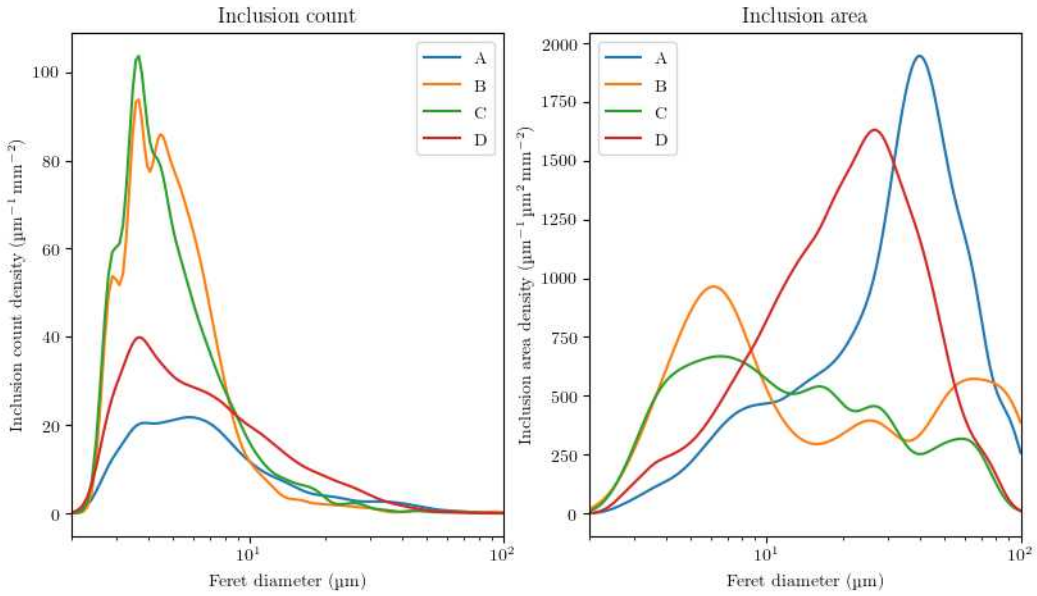

Figure 4.12 Inclusion count density (on the left) and inclusion area density (right) both vs Feret diameter. Being considered one specimen per commercial sample

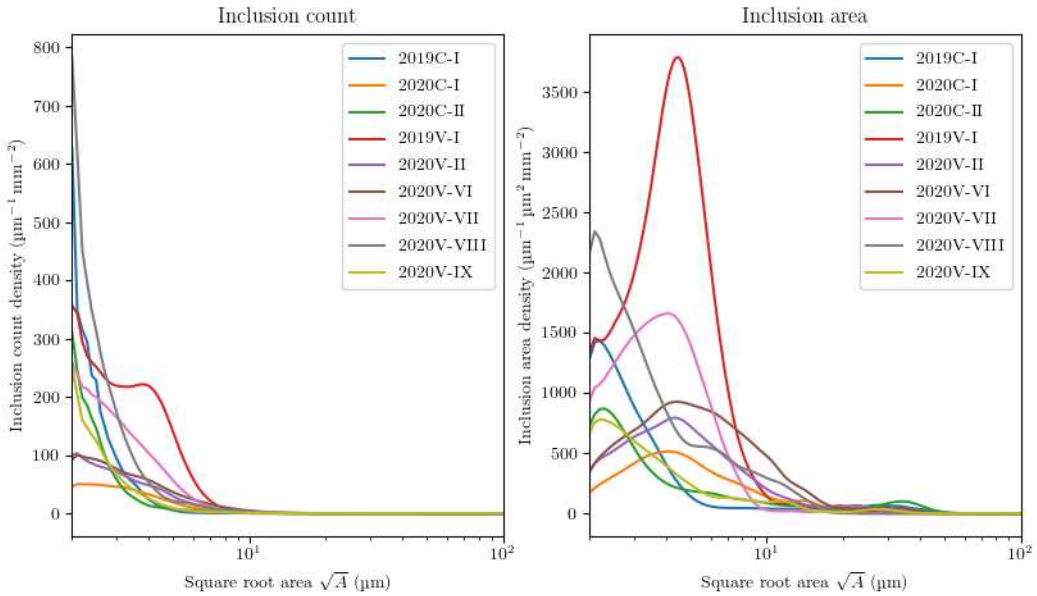

Figure 4.13 Inclusion count density (on the left) and inclusion area density (right) both vs square root area. Being considered the mean of the two **heat-treated samples** per bar

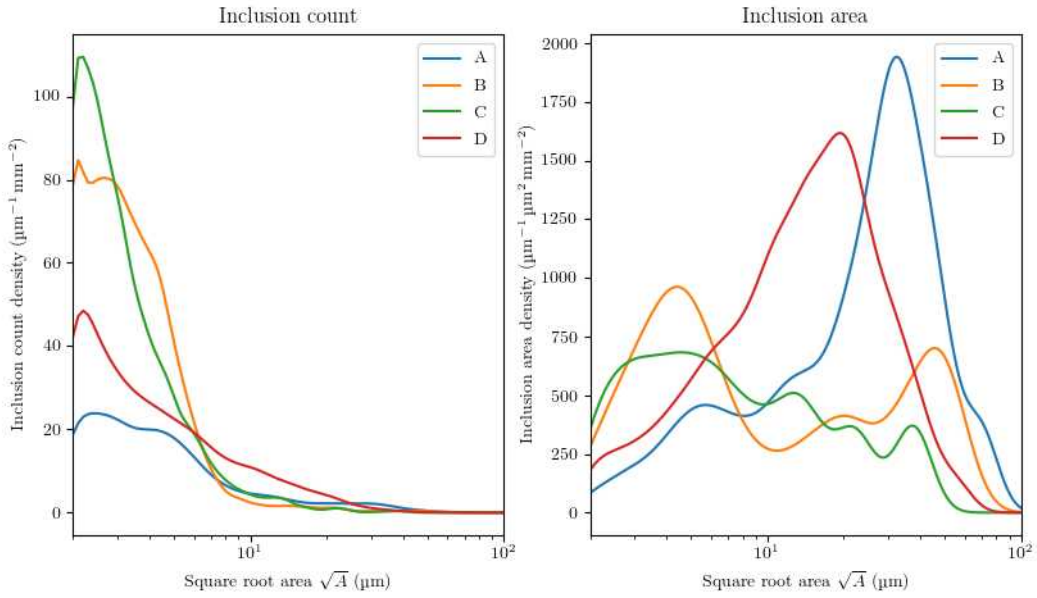

Figure 4.14 Inclusion count density (on the left) and inclusion area density (right) both vs square root area. Being considered one specimen per commercial sample

4.3.1 Inclusions characterization

As it was presented in the literature review, the characterization of the inclusions forming in the stainless steel is of prime importance as their presence can modulate critical properties, especially fatigue, toughness and corrosion. Alloying elements such as chromium, which is purposefully added to the alloy to protect its surface from the environment, may react with the dissolved oxygen and form inclusions. Slag entrainment during the casting of the molten alloy can be another source of inclusion in the cast product and should be avoided.

The effect of the presence of inclusions on the material mechanical and corrosion properties will depend on multiple inclusions characteristics such as: 1) their shape, 2) their size, 3) their distribution in the microstructure, 4) their chemical composition.

It is also important to remember that there is a major oxygen solubility limit difference between the liquid and the solid state, as seen in figure 4.15. In fact, the oxygen solubility in the solid alloy is virtually equal to zero. The rapid solidification during casting the alloy will lead to a supersaturation state. It is therefore possible that inclusions will also precipitate during the heat treatments. This solubility limit is also modulated by the chemistry of the melt. As a consequence, we can see in this figure that about 1800ppm of oxygen can be dissolved in pure iron while this solubility drops to about 400ppm for the 13Cr-4Ni alloy.

This section will present an analysis of the microstructure of our billets (in both as-cast and heat-treated conditions) using a scanning electron microscope. We payed a special attention to the presence of the biggest inclusions. The SEM pictures are followed by their respective table of spectrums.

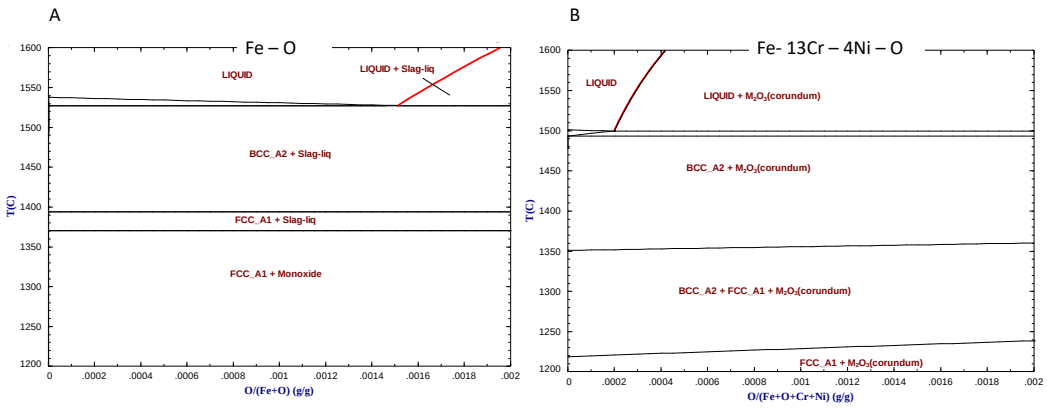

Figure 4.15 Oxygen saturation phase diagram (1 atm) for A) pure Fe and B) Fe-13Cr-4Ni, in weight fraction

2019C-I AC

Firstly, the martensitic matrix chemical composition, which was semi-quantitatively evaluated using EDS, is consistent with our OES results, at the exception of the carbon content. However, it has to be remembered that EDS is not an accurate method for the quantification of the presence of C.

The diameter of the large spherical inclusions in this billet is about 3 microns. These inclusions content is mainly Mn, Fe, O, Si and S. Considering the shape and the chemistry of these inclusions, we believe these are inclusions that were formed in the liquid state before the solidification. In fact, it seems reasonable to associate these particles to a slag phase. The presence of Al was not detected in this billet which is logical since we did not add it to the melt.

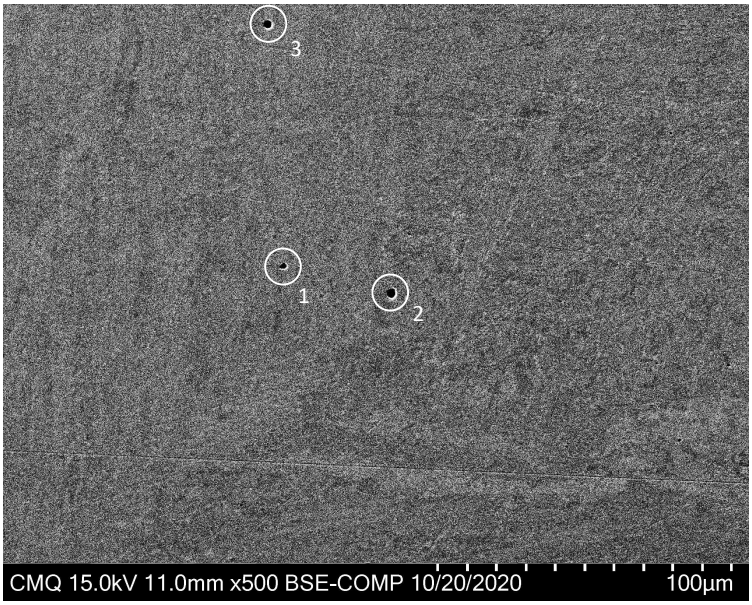

Figure 4.16 SEM image with selected inclusions from the bar 2019C-I, as-cast condition (magnification 500x)

Table 4.3 Elemental spectrum (wt.%) from EDS referring billet 2019C-I as-cast

Spectrum	Fe	Cr	Ni	Mn	C	O	Ti	Si	S	Mo	Se	Al
Matrix	75.5	14.9	5.2	1.2	2.0			0.1		0.9		
1	22.5	13.7	0.8	36.3	2.9	1.4			21.7		0.8	
2	20.9	7.1	1.0	32.2	1.3	23.7	0.4	11.1	1.9		0.3	
3	22.3	9.1	1.2	28.8	1.8	22.5	0.6	10.4	2.6		0.6	0.2

2019C-I HT

One important effect of the heat treatment on the microstructure of this billet is the precipitation of pyramidal-shape inclusions (with defined edges). These inclusions are rich in Cr, Mn, Fe and O. From our thermodynamic analysis, it can be inferred that these are probably corundum-like inclusions. We also observed the spherical inclusions coming from the melt which are of similar size than in the as-cast structure (i.e. diameter between 2-5 microns). The formation of these Cr-rich inclusions may have a negative impact on the corrosion behavior of the steel as Cr-depletion will occur in these regions.

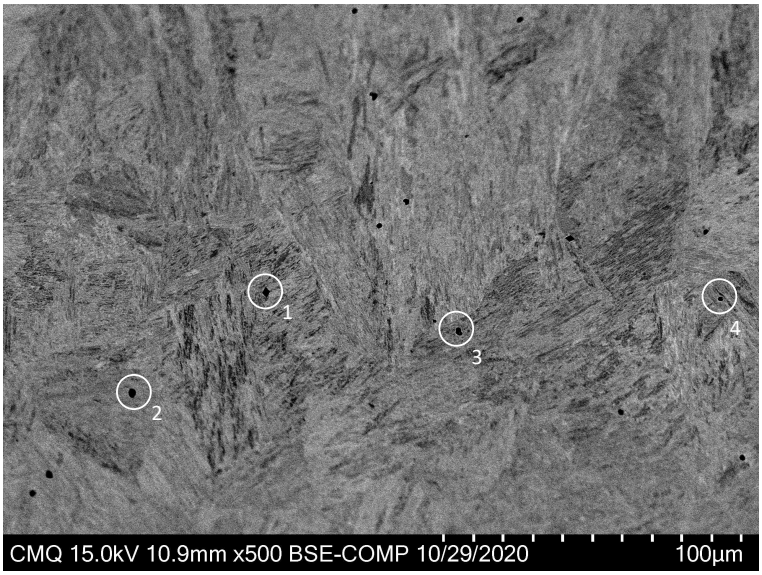

Figure 4.17 SEM image with selected inclusions from the bar 2019C-I, heat-treated condition (magnification 500x)

Table 4.4 Elemental spectrum (wt.%) from EDS referring billet 2019C-I heat-treated

Spectrum	Fe	Cr	Ni	Mn	C	O	Ti	Si	S	Al
Matrix	76.1	15.6	6.3	1.2	0.8					
1	11.3	43.7		24.4	0.8	17.5	1.3	0.1		0.8
2	15.7	29.1	1.1	31.3	0.7	13.1	1.0	1.5	6.4	
3	33.2	31.0	2.6	18.6	0.5	10.8	0.6	0.7	2.0	
4	59.0	21.3	6.0	7.9	0.7	3.5	0.6		1.0	

2020C-I AC

The chemistry of the matrix obtained from EDS analysis shows higher concentration of Cr, Mo and carbon when compared to OES results. The size of the inclusions in this billet varies between 2-10 microns. Since Al was added to the billet, the inclusions are enriched in Al when compared to the reference bulk composition (without Al addition). From the EDS semi-quantitative analyses, it can be inferred that most of them are corundum inclusions, i.e. $(Cr, Al, Fe)_2O_3$. It is to be noted that these inclusions were most probably formed in the molten alloy, as predicted by thermodynamics. Their shape is irregular and is a function of the Al-content, which is consistent with the studies found in the literature.

There is also the unexpected presence of few inclusions enriched in C, with a relatively large size (around 8 microns), as seen on figure 4.18 (right panel). Their presence needs to be further investigated as carbides are typically smaller in steels that contain very low concentration of C.

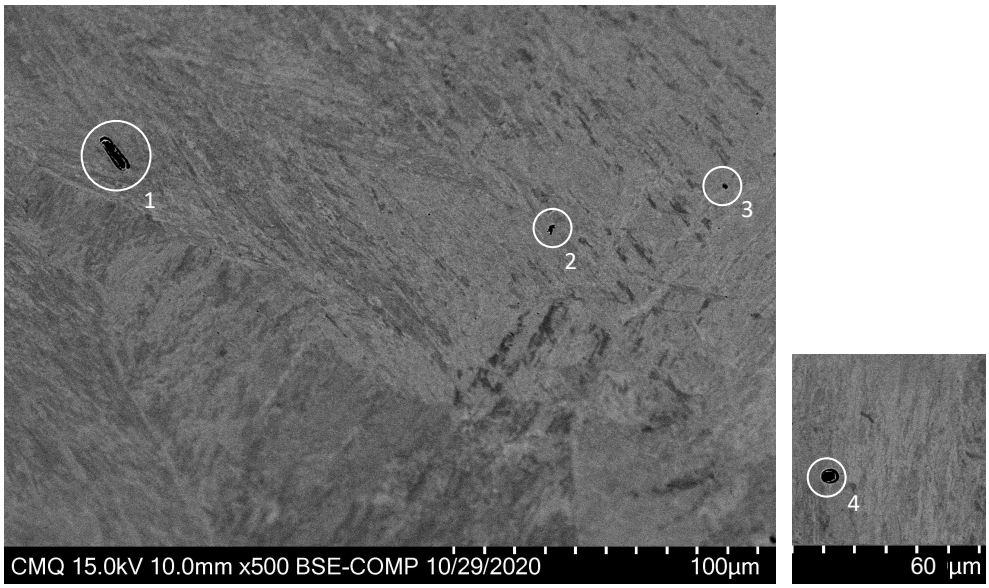

Figure 4.18 SEM image with selected inclusions from the bar 2020C-I, as-cast condition (magnification 500x)

Table 4.5 Elemental spectrum (wt.%) from EDS referring billet 2020C-I as-cast

Spectrum	Fe	Cr	Ni	Mn	C	O	S	Mo	Al
Matrix	80.8	13.2	4.3		0.8			0.9	
1	59.1	9.9	2.6	0.9	0.7	11.9	0.3		14.6
2	33.0	7.6			0.8	21.3			37.3
3	75.6	13.1	4.4		1.0	2.6		1.0	2.3
4	35.4	7.0	2.0		55.3				0.3

2020C-I HT

The most notable feature of this sample is the precipitation of an intermetallic phase containing Al, Fe and Cr. From the semi-quantitative analysis, this phase can be associated with the $(Al, Fe)_{11}Cr_2$ solid solution as reported by Pavlyuchkov et al [61].

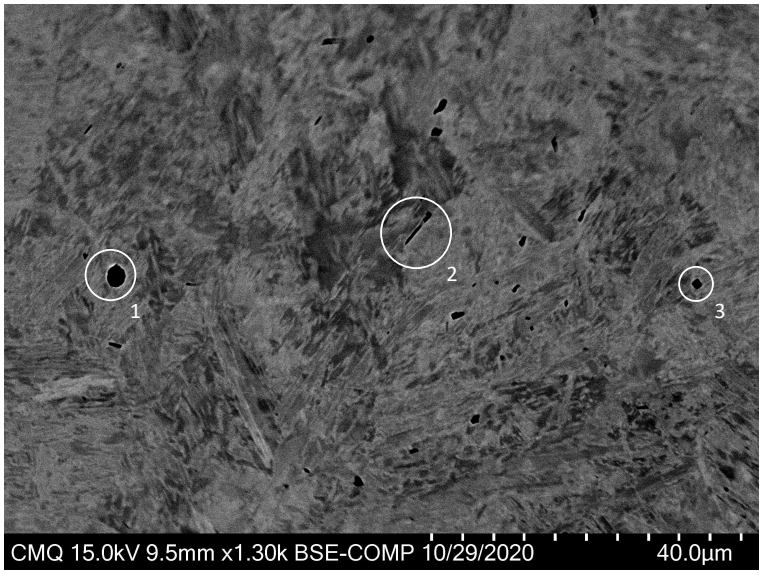

Figure 4.19 SEM image with selected inclusions from the bar 2020C-I, heat-treated condition (magnification 500x)

Table 4.6 Elemental spectrum (wt.%) from EDS referring billet 2020C-I heat-treated

Spectrum	Fe	Cr	Ni	Mn	C	O	Ti	S	Mo	Al	N
Matrix	80.1	13.7	4.3		1.1				0.9		
1	20.1	9.4	1.0	0.7	1.2	24.3	1.7	0.4		41.2	
2	76.7	13.1	3.2	1.1	1.1			0.3		3.4	1.1
3	54.1	11.0	3.3	1.9	0.8	0.8		0.7		22.5	5.6

2020C-II AC

One important feature of this billet is that hematite (Fe_2O_3) was added the melt to pollute in oxygen. Our strategy was successful as there are clear evidences that the hematite melted dissolved in the molten alloy and allowed the formation of a inclusions containing Fe, Mn, Cr and O.

Our thermodynamic calculations predict that these inclusions should be spinel solid solutions of the type $(Fe, Mn, Cr)_3O_4$. However, the predicted composition does not match the EDS spectrum. The size of these inclusions varies between 2-4 microns.

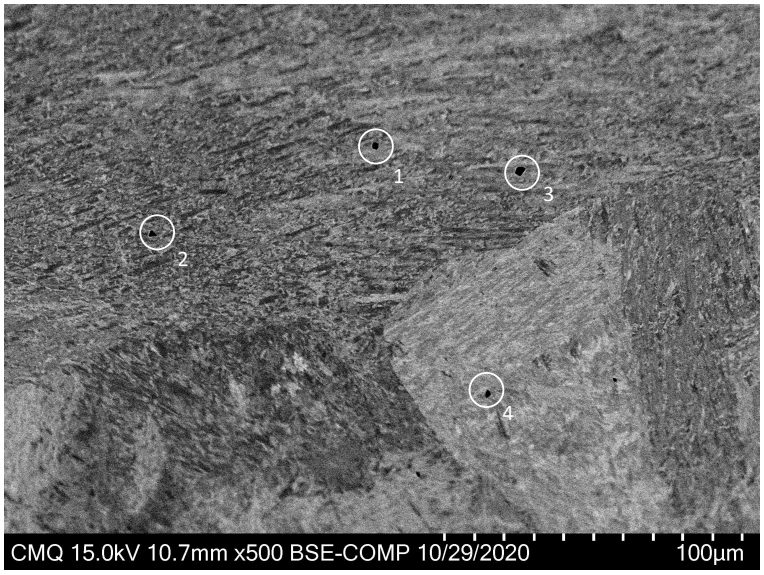

Figure 4.20 SEM image with selected inclusions from the bar 2020C-II, as-cast condition (magnification 500x)

Table 4.7 Elemental spectrum (wt.%) from EDS referring billet 2020C-II as-cast

Spectrum	Fe	Cr	Ni	Mn	C	O	Ti	Al	F	Mg
Matrix	81.9	13.5	3.7		0.9					
1	31.3	34.3	1.7	16.8	0.8	12.5	1.5	0.2	0.8	
2	24.3	38.2		20.0	0.7	15.3	1.4			
3	36.3	31.9	1.3	14.4	1.1	13.3	0.9	0.4		0.4
4	36.7	32.4	1.4	14.4	0.9	13.1	1.2			

2020C-II HT

Two important microstructural features were found in this heat-treated sample. Firstly, we were able to find elongated inclusions that probably precipitated during the heat treatment. Secondly, we found triangular-like shape inclusions with a different nominal chemical composition when compared to the inclusions in the as-cast state. These inclusions are rich in Cr, Mn and O with a low amount of Fe when compared to the as-cast inclusions. The size of the inclusions varies between 3-10 microns.

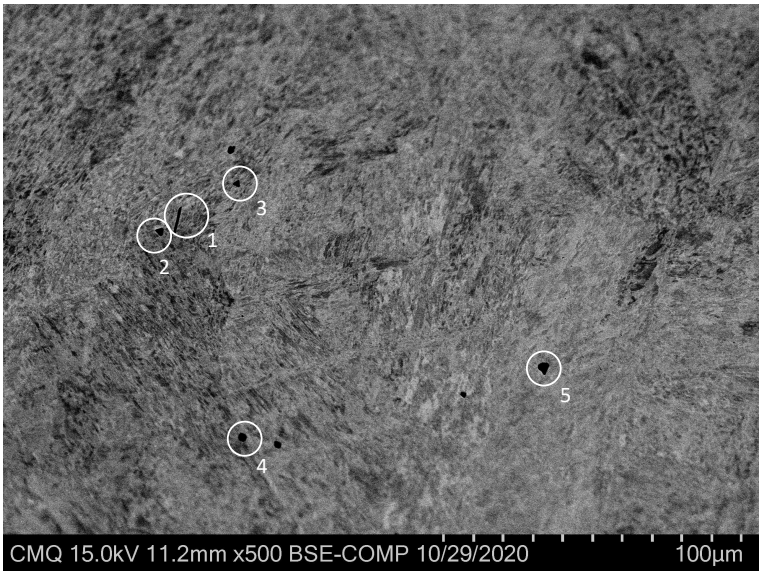

Figure 4.21 SEM image with selected inclusions from the bar 2020C-II, heat-treated condition (magnification 500x)

Table 4.8 Elemental spectrum (wt.%) from EDS referring billet 2020C-II heat-treated

Spectrum	Fe	Cr	Ni	Mn	C	O	Ti	Al	S	V
Matrix	81.9	13.2	4.1		0.7					
1	53.1	24.6	2.5	10.2	0.7	8.4	0.4			
2	14.1	42.6	0.7	22.1	1.0	17.9	1.0	0.2		0.3
3	5.3	47.9		26.5	0.7	17.9	1.8			
4	3.6	47.0		26.8	0.8	19.4	2.1	0.3		
5	27.1	32.6	1.8	20.7	0.7	13.0	1.6		2.5	

2019V-I AC

This is the first billet obtained from the argon-dripping furnace in 2019. The SEM image shows bulky inclusions rich in Cr, Mn and O. Their size is about 6-9micron. These should be spinel inclusions according to our thermodynamic calculations. There is also the presence of some small spherical inclusions (1-2 microns in diameter) which are associated to the formation of a slag (containing Si) during the melting operation.

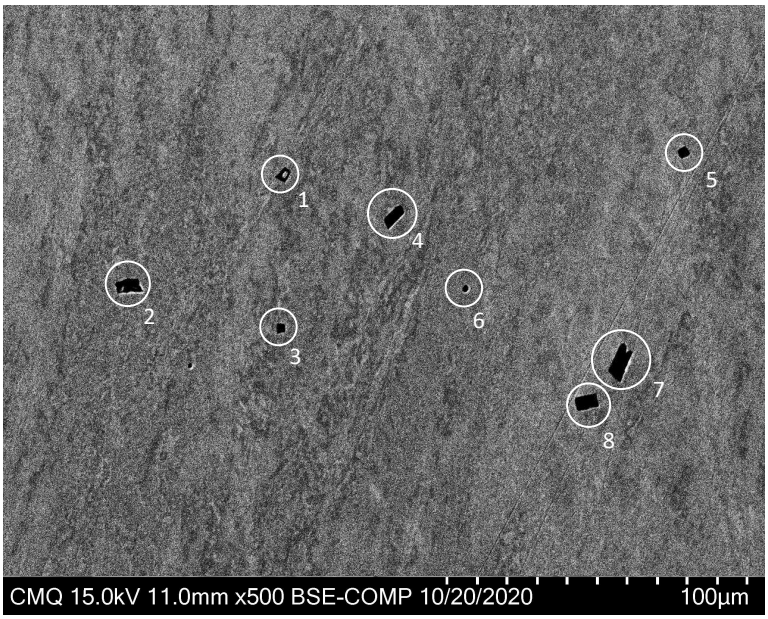

Figure 4.22 SEM image with selected inclusions from the bar 2019V-I, as-cast condition (magnification 500x)

Table 4.9 Elemental spectrum (wt.%) from EDS referring billet 2019V-I as-cast

Spectrum	Fe	Cr	Ni	Mn	C	O	Si	S	Mo	Se	Al	V
Matrix	77.4	13.0	4.9	1.0	2.7		0.2		0.8			
1	6.2	44.8		22.1	1.4	25.1	0.1					0.3
2	2.5	44.4		21.4	2.1	29.1	0.1				0.2	0.3
3	5.1	45.2		23.2	1.6	23.8	0.2	0.5			0.3	0.3
4	3.4	43.2		21.2	1.8	29.6	0.1				0.4	0.3
5	4.5	43.8		22.0	1.5	27.3	0.2				0.6	0.3
6	29.8	10.2	1.5	29.3	1.5	16.3	8.0	2.8		0.5		
7	2.7	44.9		21.2	1.3	29.4	0.1				0.1	0.2
8	2.7	44.3		20.9	1.8	29.7	0.1				0.2	0.3

2019V-I HT

The only noticeable difference here after heat treating the billet is the formation of elongated inclusions with a similar composition as the inclusions formed in the molten alloy.

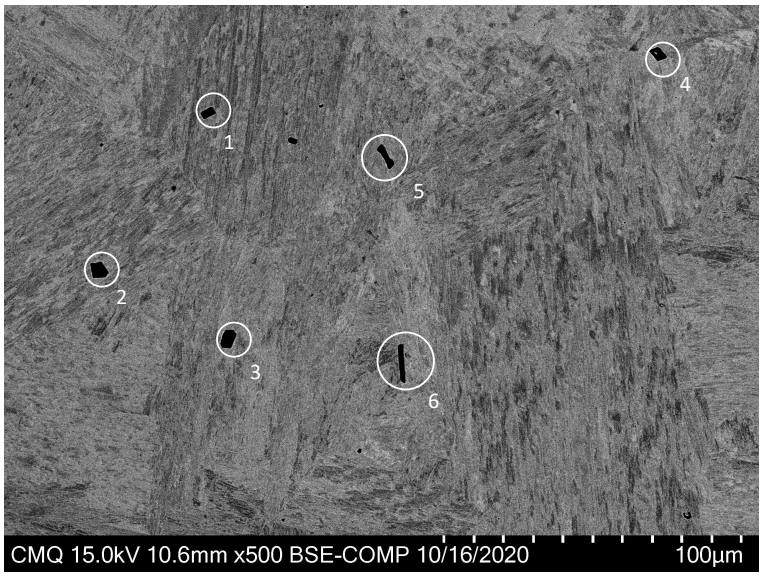

Figure 4.23 SEM image with selected inclusions from the bar 2019V-I, heat-treated condition (magnification 500x)

Table 4.10 Elemental spectrum (wt.%) from EDS referring billet 2019V-I heat-treated

Spectrum	Fe	Cr	Ni	Mn	C	O	Si	Al	V
Matrix	78.5	12.7	3.5	0.7	4.0	0.4		0.1	
1	2.6	43.4		22.6	2.3	27.9	0.5	0.3	0.4
2	2.6	44.3		22.4	2.4	27.9	0.1	0.1	0.4
3	1.7	44.1		23.0	2.5	28.3		0.2	0.2
4	2.6	44.0		22.9	2.7	27.8		0.1	
5	6.7	42.0	0.6	22.1	2.6	25.4		0.4	
6	9.2	40.9		21.1	2.8	25.3	0.2	0.5	

2020V-II AC

A major feature of this billet is the high aluminum addition which led to the lowest oxygen content for this furnace. The nominal composition of the EDS spectrum of the spherical inclusions of this SEM image (figure 4.24) was used in FactSage to predict the phase assemblage associated to this composition. According to our calculations, this composition should lead to an equilibrium between alumina and the molten alloy. It is therefore suspected that the alumina particle are not whetted by the molten metal, which would result in weak interfaces between the matrix and the inclusion. Another hypothesis at this point is that these spherical alumina inclusions are more brittle when compared to the other types of inclusions. This would explain the relatively poor performance of these material, considering their low oxygen content. The diameter of these inclusions is about 8-10 microns, with the presence of smaller inclusions (1-2 microns).

2020V-II HT

The noticeable feature for the heat-treated sample of this billet is that the newly precipitated inclusions present a lower content of Fe combined to a higher amount of Al and oxygen. The inclusions also have a round-like shape (figure 4.25).

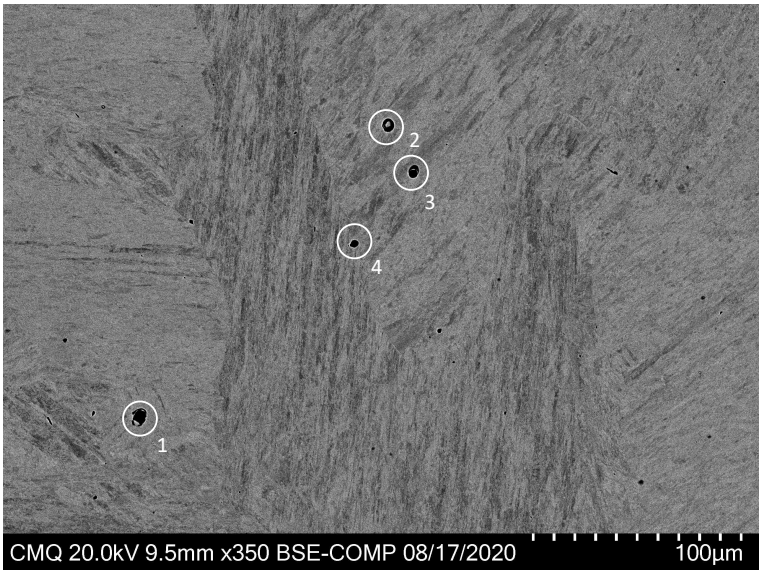

Figure 4.24 SEM image with selected inclusions from the bar 2020V-II, as-cast condition (magnification 500x)

Table 4.11 Elemental spectrum (wt.%) from EDS referring billet 2020V-II as-cast

Spectrum	Fe	Cr	Ni	Mn	C	O	Si	S	Mo	Al	Ca
Matrix	75.8	13.1	4.2	0.9	4.6	0.5			0.6	0.2	
1	33.2	7.1	1.1	0.5	6.7	26.2	0.4			24.7	0.2
2	71.6	12.1	4.0	1.0	5.3	2.8	0.2	0.3		2.7	
3	44.6	8.9	1.7	0.4	6.7	17.4	0.2	0.1		19.7	0.2
4	67.2	13.5	2.2	2.4	2.6	6.4	0.1	0.3		5.2	

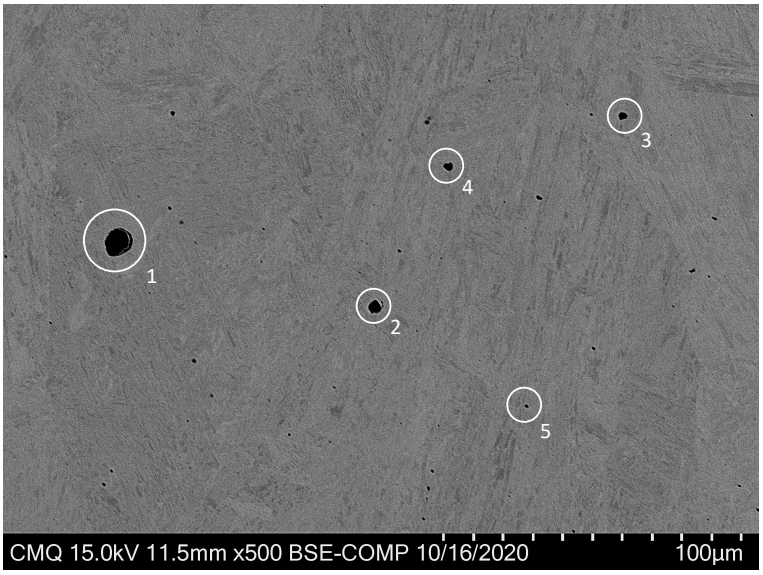

Figure 4.25 SEM image with selected inclusions from the bar 2020V-II, heat-treated condition (magnification 500x)

Table 4.12 Elemental spectrum (wt.%) from EDS referring billet 2020V-II heat-treated

Spectrum	Fe	Cr	Ni	Mn	C	O	Si	S	Mo	Al	Ca	Cl	Cu
Matrix	75.9	13.5	4.8	0.9	3.3	0.6			0.8	0.2			
1	14.8	3.0	0.7		6.4	36.2	0.3			38.3	0.4		
2	21.7	4.0	0.6		7.2	35.7	0.2	0.2		30.1		0.4	
3	25.6	5.5	1.5	0.9	4.7	29.7	0.2	0.8		31.2			
4	34.2	6.9	1.7	2.0	2.3	22.9		1.5		24.4			3.9
5	57.5	10.8	3.5	0.8	2.1	11.9	0.1		0.6	12.5			

2020V-VI AC

This billet was deoxidized using Al but was not skimmed prior to casting. Even thought it resulted in a low oxygen content, its V-notch toughness was modest. These results seem to demonstrate that alumina particle need to be fluxed and removed prior to casting since their presence in the steel is detrimental.

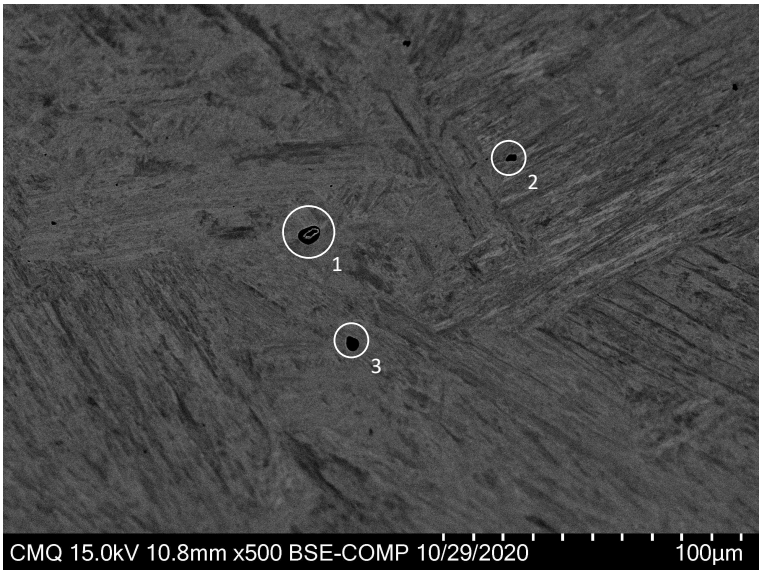

Figure 4.26 SEM image with selected inclusions from the bar 2020V-VI, as-cast condition (magnification 500x)

Table 4.13 Elemental spectrum (wt.%) from EDS referring billet 2020V-VI as-cast

Spectrum	Fe	Cr	Ni	Mn	C	O	Si	S	Mo	Al	Ca
Matrix	79.5	13.7	4.4	1.2	0.9			0.3			
1	71.7	12.3	4.1	0.9	1.4	5.5	0.1		0.8	2.9	0.2
2	31.1	6.8	1.2	0.5	1.1	21.6		0.4		31.7	0.8
3	51.9	9.0	2.7	0.8	1.5	14.0		0.3		18.2	0.2

2020V-VI HT

The heat treatment performed on this billet seemed to have a major impact on the presence of the spherical zones observed in the as-cast billet. Also, this is one of the argon-dripping furnace billets for which the v-notch toughness was the most improved when compared to the as-cast state. Therefore, it is suspected that the heat treatment was able to eliminate or homogenize these spherical zones.

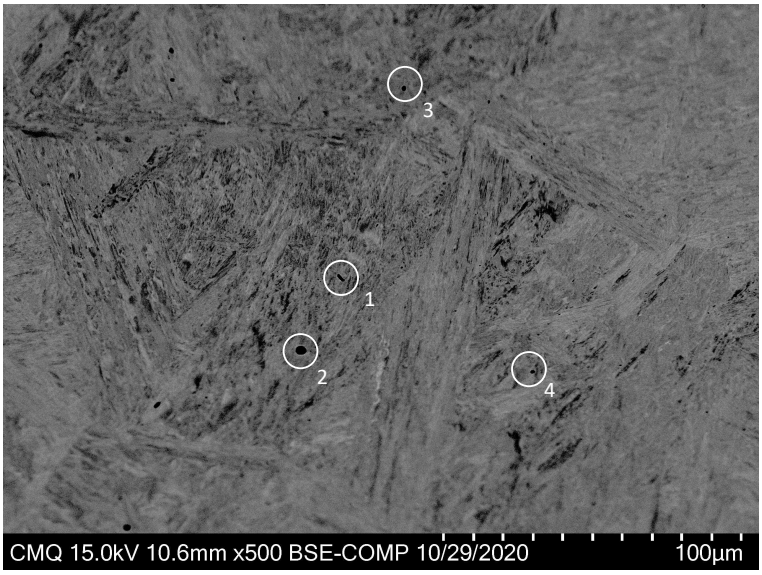

Figure 4.27 SEM image with selected inclusions from the bar 2020V-VI, heat-treated condition (magnification 500x)

Table 4.14 Elemental spectrum (wt.%) from EDS referring billet 2020V-VI heat-treated

Spectrum	Fe	Cr	Ni	Mn	O	Si	S	Al	Ca	Cu	P
Matrix	79.3	13.8	4.8	1.1							
1	33.2	7.3	1.8	3.6	20.7		2.0	31.5			
2	22.1	4.4	0.9	1.1	27.0	0.3	0.5	42.4	1.0		0.2
3	37.3	8.5	1.7	24.3	5.4		11.1	8.3		3.4	
4	63.3	12.2	2.8	1.6	7.3		0.4	12.3			

2020V-VII AC and 2020V-VII HT

This billet was partially de-oxidized using aluminum and skimmed prior to the casting. Interestingly, we did not detect the presence of aluminum in the inclusions which proved the effectiveness of the operation. These angular shape inclusions were rich in Cr, Mn and O, with small amount of Fe. According to FactSage calculations, these should be $MnCrO_4$ spinel inclusions (in equilibrium with the molten metal). The characteristic size of these inclusions is about 3-6 microns, with bigger inclusions around 8-10 microns. It is to be noted that this sample outperformed the non-skimmed sample 2020V-VI even if its oxygen content was higher, which stresses the importance of this step. For the 2020V-VII HT, there is nothing to report.

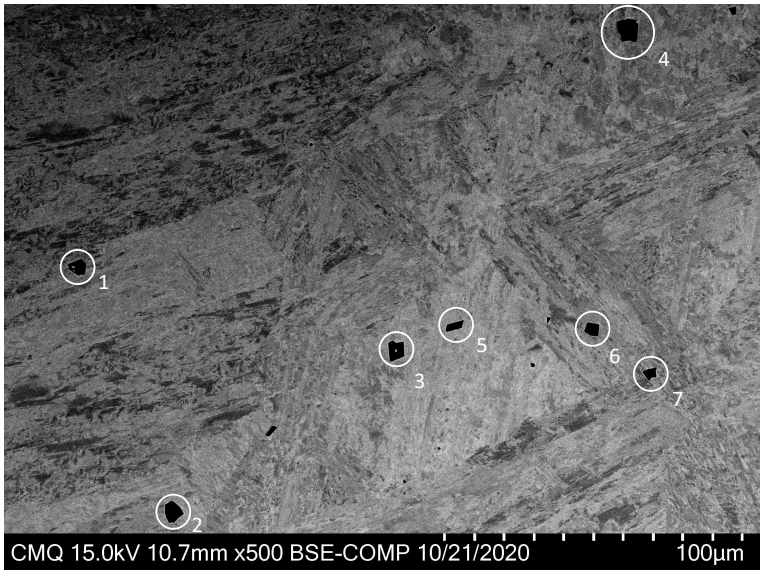

Figure 4.28 SEM image with selected inclusions from the bar 2020V-VII, as-cast condition (magnification 500x)

Table 4.15 Elemental spectrum (wt.%) from EDS referring billet 2020V-VII as-cast

Spectrum	Fe	Cr	Ni	Mn	C	O	Si	Mo	Al	N	V
Matrix	80.2	12.8	4.0	1.0	1.1	0.1		0.8	0.1		
1	2.6	50.3		23.2	1.0	22.2				0.4	0.3
2	2.7	49.8		24.3	1.2	22.0					
3	8.2	48.1		22.4	0.8	20.0			0.1		0.3
4	3.3	50.9		23.6	0.9	21.2					
5	3.7	50.2		22.5	0.8	22.1	0.1		0.3		0.3
6	3.3	50.4		23.2	0.9	22.2					
7	3.0	50.8		22.7	1.0	22.3			0.1		

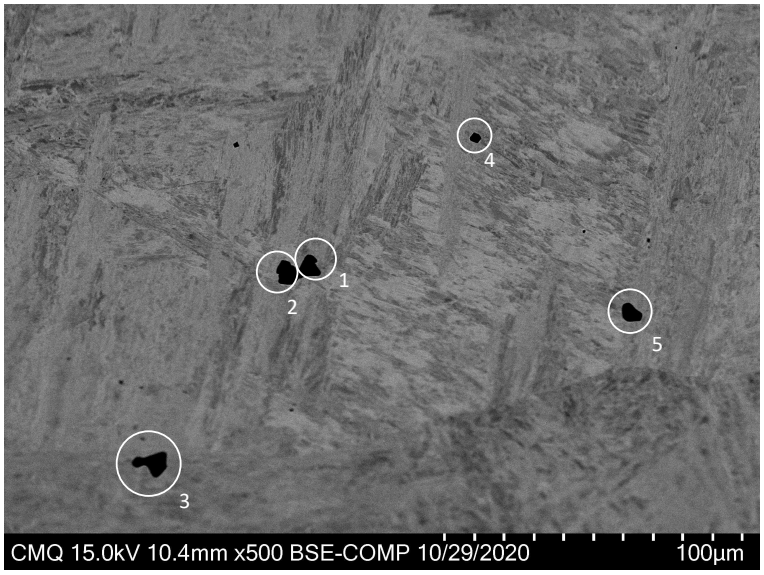

Figure 4.29 SEM image with selected inclusions from the bar 2020V-VII, heat-treated condition (magnification 500x)

Table 4.16 Elemental spectrum (wt.%) from EDS referring billet 2020V-VII heat-treated

Spectrum	Fe	Cr	Ni	Mn	C	O	Al	V
Matrix	81.7	12.8	3.7	1.0	0.8			
1	1.8	49.9		25.4	0.8	22.2		
2	3.4	48.3		25.8	0.7	21.2	0.6	
3	9.9	43.3		22.2	0.7	19.7	3.9	0.2
4	2.1	50.2		25.4	0.7	21.5		
5	1.9	49.7		26.2	0.7	21.5		

2020V-VIII AC and 2020V-VIII HT

This is the sample with the highest oxygen content. According to our FactSage calculations, the addition of hematite allowed us to reach the oxygen saturation of the alloy in its molten state (i.e. about 350ppm). As for most of the argon-dripping as-cast billets, the inclusions were angular and bulky. The characteristic size of the bigger inclusions was also larger than the other billets (about 10-13 microns). Again these Cr, Mn and O inclusions are predicted to be of a spinel type. There is not report regarding the sample 2020V-VIII HT.

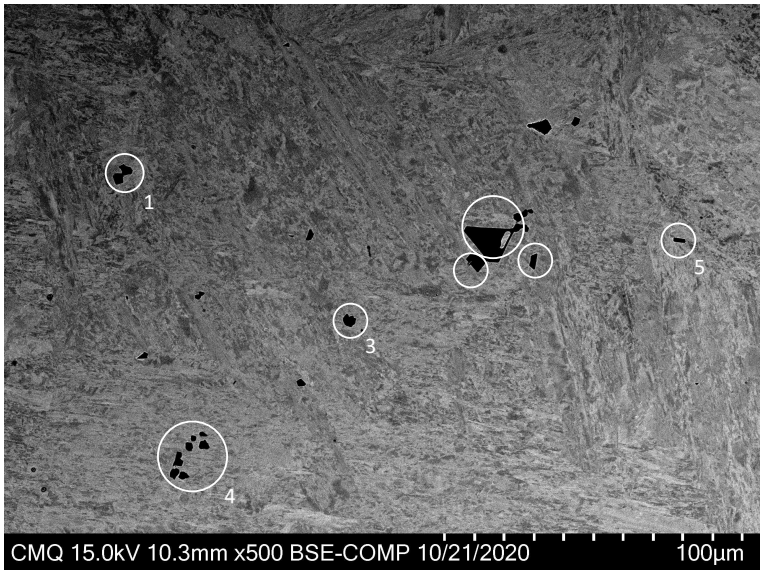

Figure 4.30 SEM image with selected inclusions from the bar 2020V-VIII, as-cast condition (magnification 500x)

Table 4.17 Elemental spectrum (wt.%) from EDS referring billet 2020V-VIII as-cast

Spectrum	Fe	Cr	Ni	Mn	C	O	Al
Matrix	81.4	12.0	3.9	0.9	1.1	0.7	
1	3.3	50.8		22.8	0.9	22.2	
2	3.7	52.1		20.9	1.0	22.2	
3	3.9	49.7		23.9	1.0	21.6	
4	4.0	50.0		23.0	0.9	22.1	
5	7.8	50.0		23.2	0.9	18.1	
6	3.1	51.3		21.5	1.0	22.9	0.1
7	3.7	50.5		23.0	0.9	21.9	

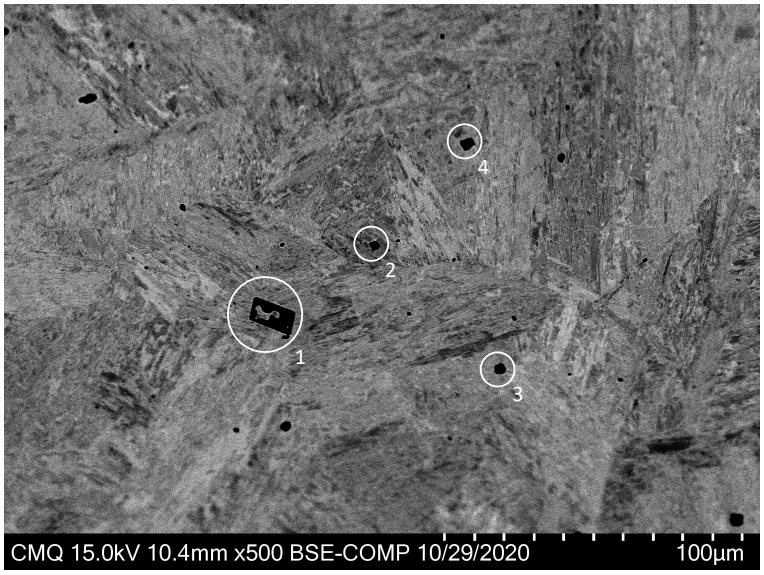

Figure 4.31 SEM image with selected inclusions from the bar 2020V-VIII, heat-treated condition (magnification 500x)

Table 4.18 Elemental spectrum (wt.%) from EDS referring billet 2020V-VIII heat-treated

Spectrum	Fe	Cr	Ni	Mn	C	O	Mo
Matrix	82.2	11.8	3.4	1.0	0.9		0.8
1	14.2	44.8		21.3	0.8	19.0	
2	2.6	49.8		26.2	0.6	20.8	
3	4.2	50.0		25.5	0.8	19.6	
4	3.0	50.0		25.8	0.8	20.5	

2020V-IX AC and 2020V-IX HT

This is the billet that presented the best V-notch toughness (in its heat-treated state) among all the argon-dripping furnace billets. It was both de-oxidized and skimmed. The skimming efficiency can be noticed in the EDS spectra of the inclusions. These spectra show that the inclusions are mostly constituted of Cr, Mn and O, with minor concentration of Al and Fe. There is nothing special to report about the bar 2020V-IX HT.

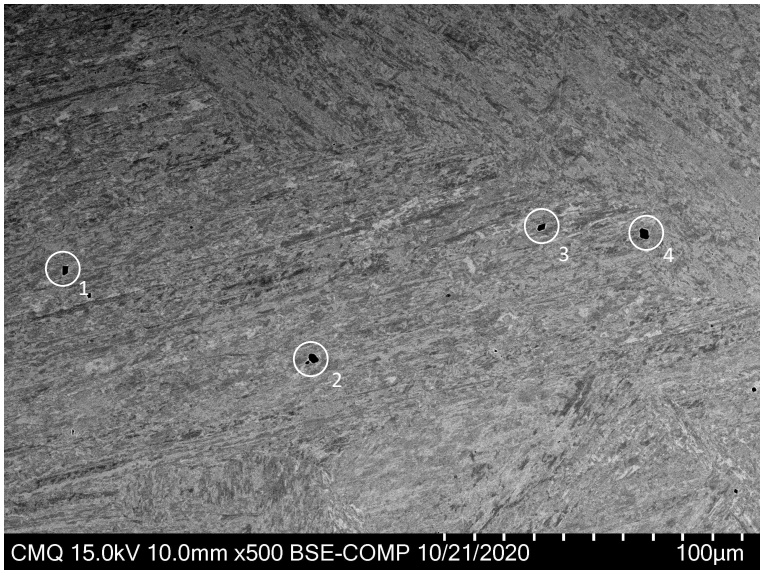

Figure 4.32 SEM image with selected inclusions from the bar 2020V-IX, as-cast condition (magnification 500x)

Table 4.19 Elemental spectrum (wt.%) from EDS referring billet 2020V-IX as-cast

Spectrum	Fe	Cr	Ni	Mn	C	O	S	Al	V
Matrix	80.4	13.0	4.4	1.0	1.2				
1	16.1	41.8	0.8	20.7	1.0	18.5	0.6	0.2	0.2
2	2.9	33.9		27.8	1.0	24.1		10.4	
3	32.1	32.2	1.4	16.4	1.0	15.4		1.5	
4	3.6	42.0		24.7	0.8	23.3		5.5	

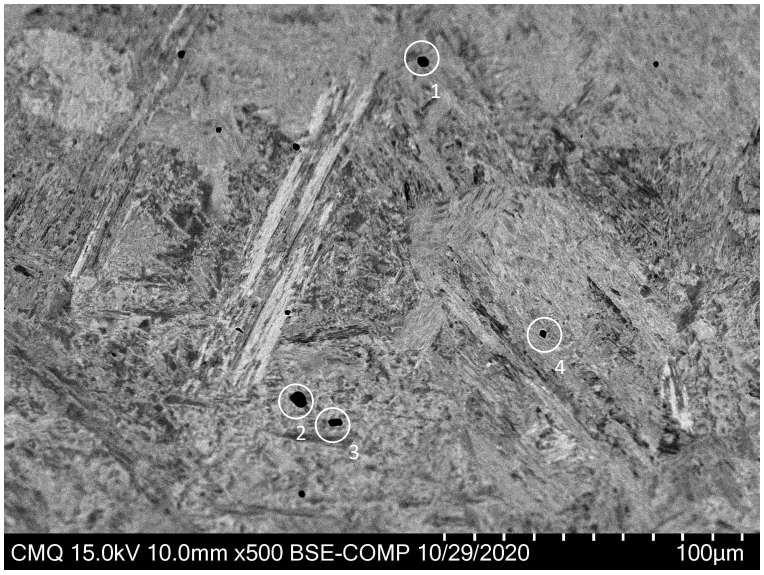

Figure 4.33 SEM image with selected inclusions from the bar 2020V-IX, heat-treated condition (magnification 500x)

Table 4.20 Elemental spectrum (wt.%) from EDS referring billet 2020V-IX heat-treated

Spectrum	Fe	Cr	Ni	Mn	C	O	Si	S	Mo	Al	Br
Matrix	79.1	13.1	4.9	1.1	0.9				1.0		
1	4.2	39.7		28.3	0.6	21.1		0.4		5.6	
2	2.0	31.1		30.0	0.7	23.6				10.5	2.1
3	3.7	46.4		26.7	0.7	20.3	0.1	0.2		1.8	
4	6.8	44.7		26.2	0.6	19.7				2.0	

Commercial samples

Hydro-Québec provided us with four 13Cr-4Ni commercial samples (defined as A,B, C and D). SEM images of these materials revealed interesting features about these commercially produced alloys when compared to our billets. Firstly, it is clear that the inclusions are bigger, but fewer. Sample A presents for example a large slag inclusion (containing Si). These slag inclusions were also observed in sample D. The presence of sulfur also appears to be significant in these materials. This element was not considered in our study. Sample B and C were definitively de-oxidized with aluminum (this is confirmed by their low oxygen content). As for some of our samples, it looks like they did not completed skimmed their melt prior to casting. As a result, the commercial alloys B and C experienced the same formation

of spherical regions associated to large alumina inclusions.

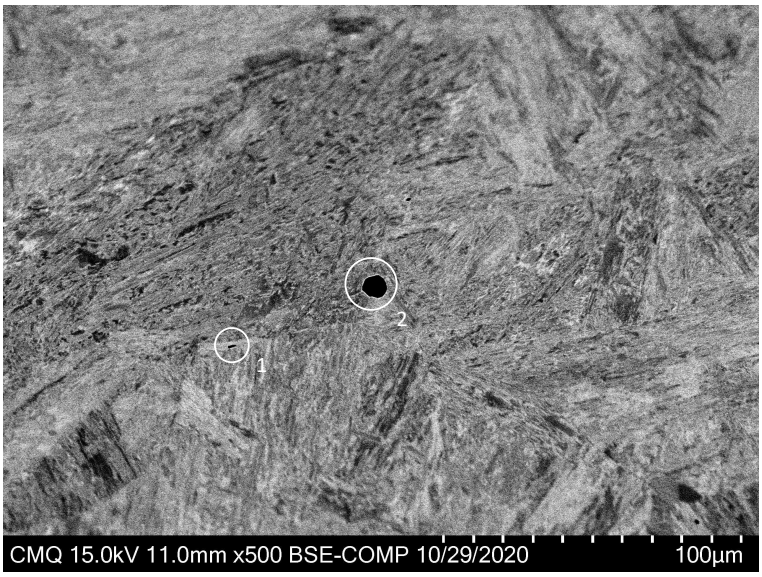

Figure 4.34 SEM image with selected inclusions commercial sample A (magnification 500x)

Table 4.21 Elemental spectrum (wt.%) from EDS referring commercial sample A

Spectrum	Fe	Cr	Ni	Mn	C	O	Si	S	Cu	Al	Ti	Mg	Ca
Matrix	82.7	12.9	3.3		0.8		0.3						
1	41.0	6.8	2.1	30.4	0.9			14.2	4.6				
2	4.9	14.2		24.1	0.8	23.2	15.8	8.3		6.6	0.9	0.6	0.6

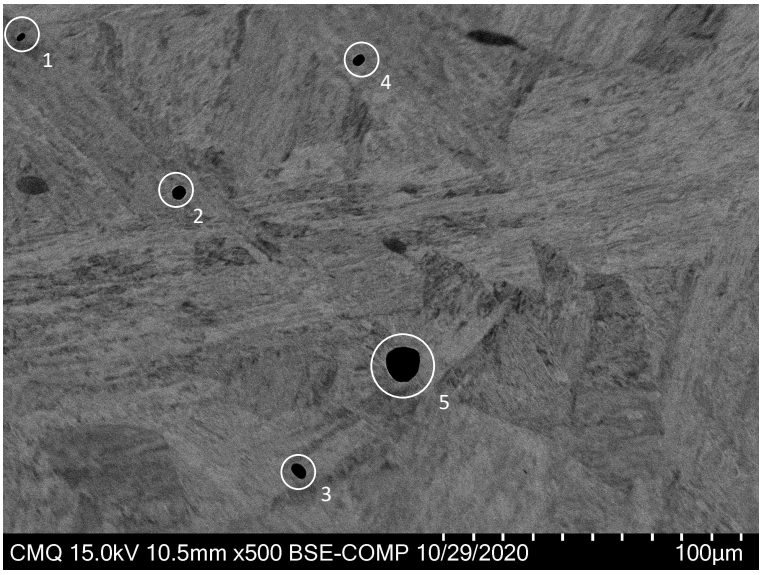

Figure 4.35 SEM image with selected inclusions commercial sample B (magnification 500x)

Table 4.22 Elemental spectrum (wt.%) from EDS referring commercial sample B

Spectrum	Fe	Cr	Ni	Mn	C	O	Si	S	Al	Mg	Ca
Matrix	80.5	13.8	4.0		1.1		0.6				
1	68.9	11.3	3.4	1.1	0.9	5.1	0.4	0.5	7.6	0.4	0.3
2	2.3				0.9	34.6			48.0	14.2	
3	4.0	1.3		1.4	1.0	30.0		5.8	35.1	15.1	6.2
4	40.5	7.5	2.3	2.6	1.1	11.8	0.3	6.8	13.8	6.1	7.2
5	1.2	0.6			0.6	31.1		10.8	32.8	6.7	16.2

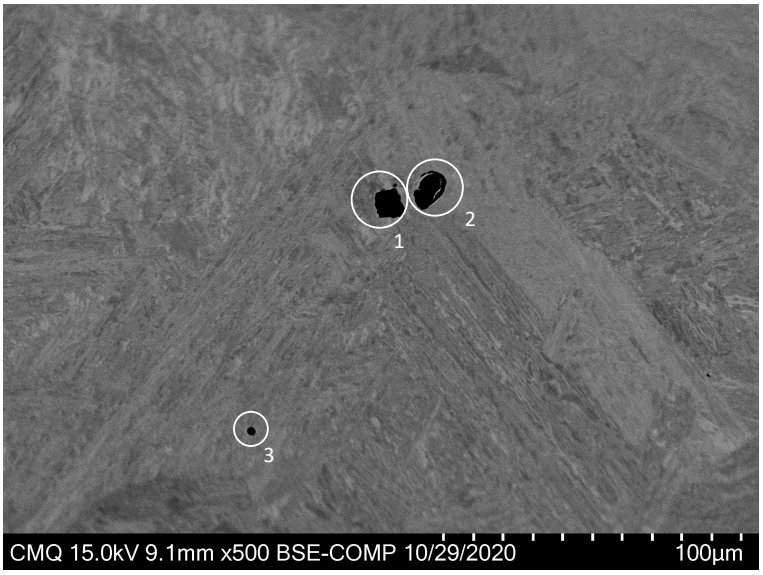

Figure 4.36 SEM image with selected inclusions commercial sample C (magnification 500x)

Table 4.23 Elemental spectrum (wt.%) from EDS referring commercial sample C

Spectrum	Fe	Cr	Ni	Mn	C	O	Si	S	Cu	Al	Mg	Ca
Matrix	82.3	12.3	4.1		0.9		0.4					
1	1.7					34.7				48.5	13.2	1.8
2	25.8	5.5		9.6	30.3	11.9		4.7		8.9	0.6	2.7
3	4.0	3.0		24.2	1.0	15.9		16.2	0.8	30.0		4.8

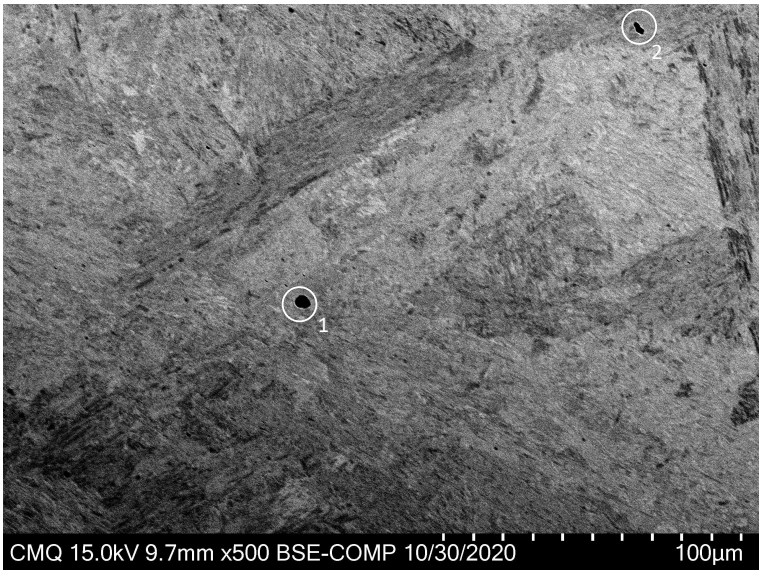

Figure 4.37 SEM image with selected inclusions commercial sample D (magnification 500x)

Table 4.24 Elemental spectrum (wt.%) from EDS referring commercial sample D

Spectrum	Fe	Cr	Ni	Mn	C	O	Si	S	Cu	Al
Matrix	80.3	12.7	3.6		3.4					
1	1.6	1.2		5.7	4.0	44.0	38.6	4.9		
2	56.2	9.3	1.6	3.0	5.1	6.0	3.0	3.5	10.6	1.5

4.4 Impact toughness

A summary of all the results of the v-notch Charpy tests is displayed in figure 4.39. This graph presents the performance of all the nine billets in both as-cast and heat-treated states. The columns indicate the mean impact absorbed energy (which amplitude should be read in the left y-scale). The blue dots show the oxygen content of each specimen (which amplitude can be read on the right y-axis). The blue line crossing the entire graph indicates the minimum performance requirement as provided by our industrial partner. This minimal requirement is 50J. The dark color columns illustrate the performance of the heat-treated samples, whereas the light ones the performance of the as-cast specimens. Under the graph are displayed complementary information concerning the composition of each billet. The samples from the VIP furnace are represented in red and in green for the CONSARC.

The specimens in both condition performed greater than the minimum required, with the

exception of the 2020V-VI (as-cast) which was slightly below the requested. The heats specimens from the CONSARC furnace presented a better behavior when compared to the other bars. Another important point to mention here is that 2 Charpy specimens from the 2020C-I billet in the as-cast state did not completely break while one specimen of the heat-treated sample required more than 80% of the range capacity. These results were accounted for as recommended by ASTM [62] for metallic materials. As an overview, the resistance performance is significantly improved by the heat treatment, however it is no considerably affected by the oxygen content. There is not a well defined trend relating the range of oxygen content analyzed and impact toughness.

When comparing our results for the heat-treated samples with those of a prior study made with the cast (CA6NM = commercial sample A) and wrought 13Cr-4Ni steel (see figure 4.39), we see that most of our samples present a similar or even better performance then these commercial alloys. The four billets (2019V-I, 2020V-VI, 2020V-VII, 2020V-VIII) that showed the worse performance are those with large oxygen content at the exception of the 2020V-VI billet which was deoxidized but not skimmed.

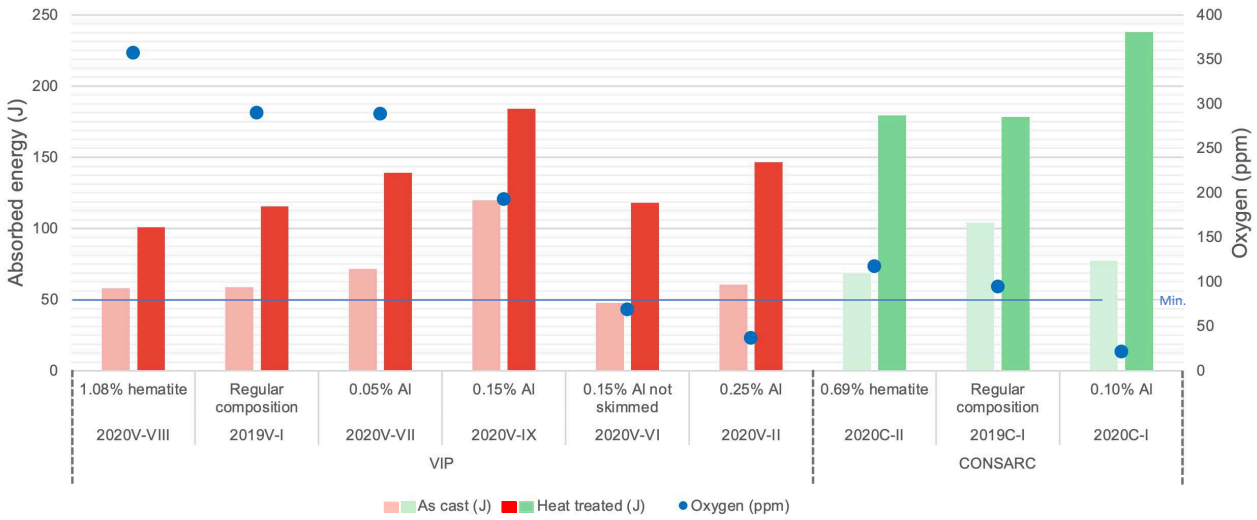

Figure 4.38 V-notch Charpy results vs oxygen content, being accounted all the samples in as-cast and heat-treated condition from both furnaces

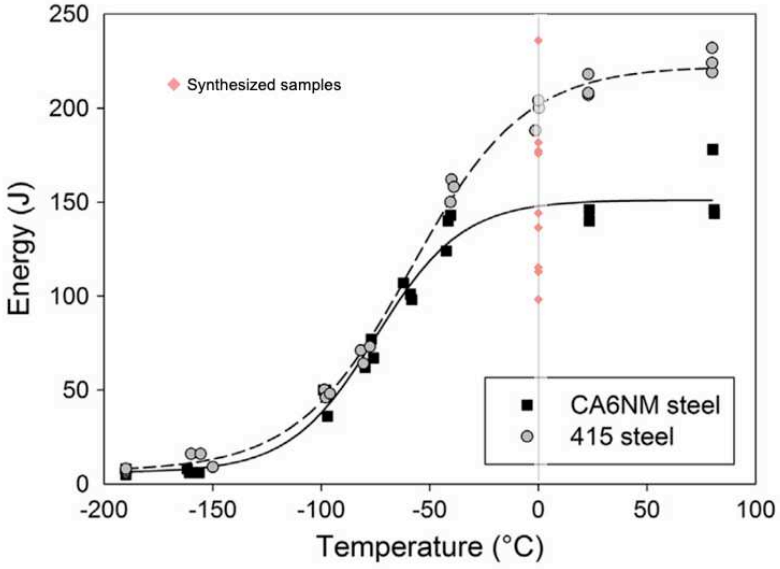

Figure 4.39 V-notch Charpy results vs temperature, being accounted all the samples heat-treated from both furnaces displayed as red rhombus, adapted from [25]

4.4.1 Charpy fractures

Figure 4.40 shows macrographies of the fracture surface of the samples synthesized in the argon-dripping VIP furnace which were subjected to Charpy impact tests performed at 0 Celcius. Two batches of triplicates specimens are presented for each sample (label shown below each panel). The triplicates at the top are specimens tested in their as-cast state while the triplicates at the bottom were heat-treated specimens.

In general, we can qualitatively distinguish between ductile and fragile failures with the following evidences: for fragile fractures, the Charpy specimen keep their original shape as there is no plastic deformation associated to the failure. Also brittle failure induces cleavage surfaces that reflect light more. This results in shiny metallic surfaces when observed with the naked eye. Most of the as-cast samples present these two characteristics. For ductile fracture, we can see clear evidences of plastic deformation. The surface is also more tarnished and shows dimples.

As seen previously, the 2020V-IX sample showed the best v-notch toughness performance among all the samples produced with the argon-dripping furnace. As-cast surfaces of this sample are mostly tarnished and grey with few shiny zones. There are also evidences that the as-cast specimen were plastically deformed when looking at their deformed prism shape. The heat-treated specimen are severally deformed when compared to the other samples. This

trend between the as-cast and heat-treated samples is repeated for all the billets, regardless of the furnace in which they were synthesized. Therefore, we can conclude that the heat treatment soften the alloy and improve the ductility of the material. Figure 4.41 provides the fracture appearance of the samples synthesized in the vacuum CONSARC furnace.

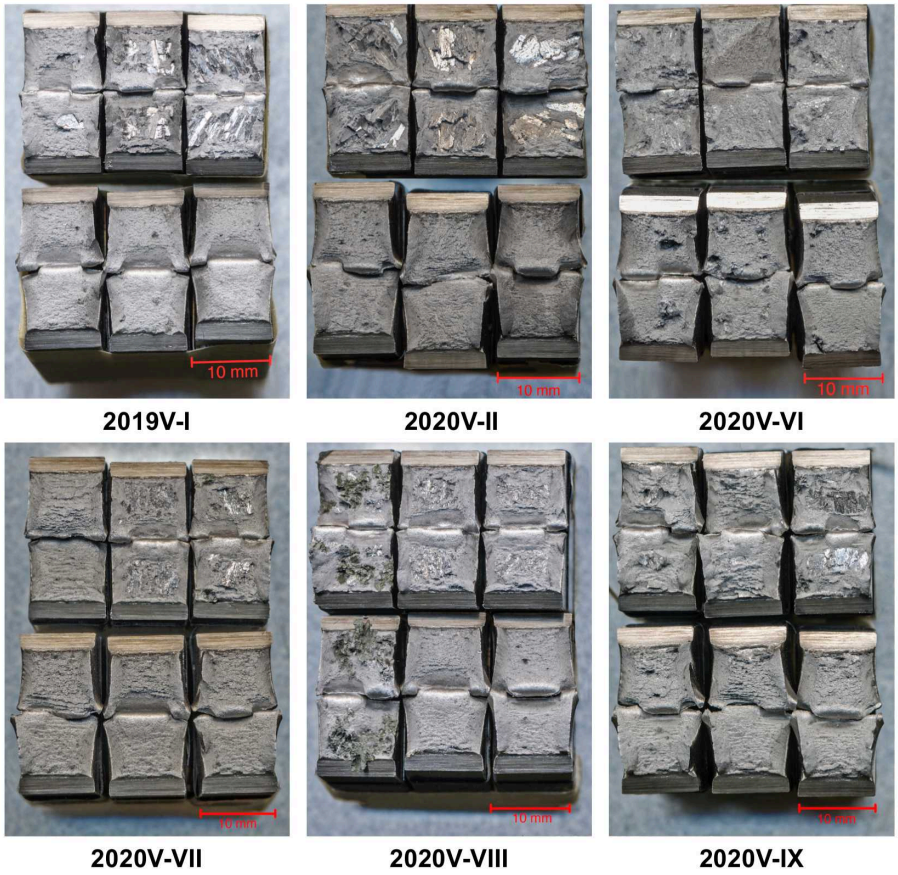

Figure 4.40 Fracture surface of Charpy impact tested samples, specimens synthesized in the VIP furnace

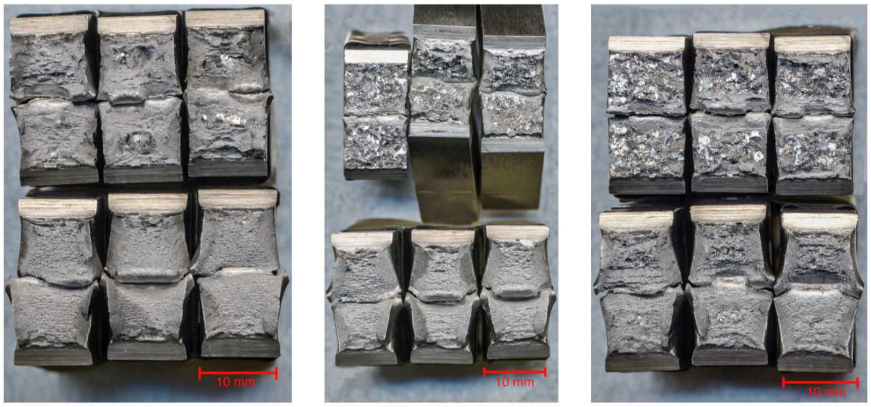

Figure 4.41 Fracture surface of Charpy impact tested samples, specimens synthesized in CONSARC furnace

4.5 Hardness

The chart presented in figure 4.42 shows the relation between hardness measurements and oxygen level of the specimens. This graph was loaded with the results of the measurements done using Rockwell C (HRC) method being converted to hardness Brinell number (HBN). The conversion was made following the conversion table from the study [63] as recommended by H.-Q [64]. The conversion was performed in order to generate comparable results from the commercial samples, since these specimens were only measured using the HRC method.

All the specimens were measured and the average is represented by the columns. The HBN value are verified in the left axis, while the right scale shows the oxygen concentration, indicated in each sample by the blue point. The design of the graph is the same as present in the previous chart with the addition of the yellow bars representing the commercial samples. The blue line crossing the graph identifies the maximum value accepted. Complementary information about each sample is displayed below the graph.

The results show a similarity among them. The heat-treated samples were softener than the as-cast, which was expected as a consequence of the thermal treatment. The heats specimens met the required hardness specification, presenting results nearly to the commercial samples. The oxygen content did not present a relation to the analyzed property. Meaning that hardness is linked with the properties of the matrix, not with oxygen concentration nor the presence of inclusions.

When comparing the HRC measurements in the same sample, the results were very similar

to each other, showing no difference along the radial position of the sample. The synthesized samples were also analyzed through the Brinell hardness method, as required in the ASTM standard for this steel. The measurements were also very much alike among them meeting the requested spec.

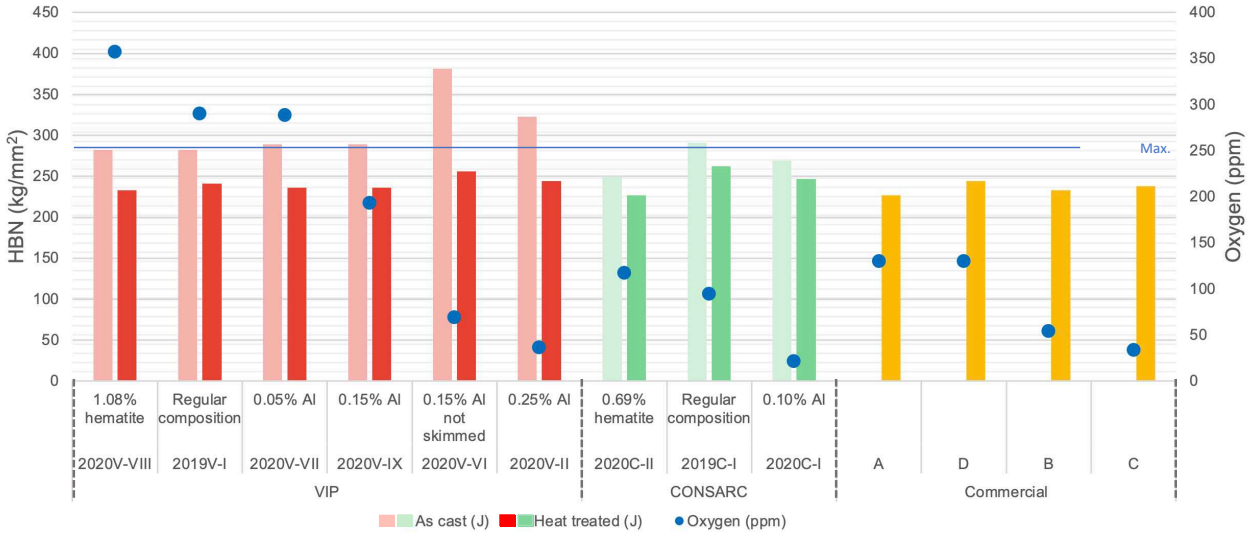

Figure 4.42 Hardness results measured in all the samples as-cast, heat-treated and commercial specimens

CHAPTER 5 CONCLUSIONS AND RECOMMENDATIONS

5.1 Conclusions

To date, there has been no systematic study reported in the literature regarding 13%Cr-4%Ni stainless steels that covers the specific effect of their oxygen content on their mechanical properties such as toughness and hardness. Moreover we could not find scientific studies that compared different melting strategies (i.e vacuum and argon-dripping) when looking at the analysis of type, shape, chemistry and distribution of inclusions after casting and heat-treating the alloys. Furthermore, there was a limited amount of microstructural characterizations for this stainless steel in the literature in both its as-quenched state (directly after the casting process) and after an austempering heat treatment. Although some studies presented some inclusion characterizations that are contaminating this stainless steel, their analyses focused on the inclusion distribution, size and type, without presenting clear data on their origin of formation, morphology and composition. To our knowledge, there also has not been published computational thermo-chemistry simulations of that steel to better understand the type of inclusions that are forming during its elaboration (including melting and heat treating).

In this study, 9 stainless steel billets of about 9 kg containing different oxygen levels were synthesized. These billets were cut and machined into smaller samples for further investigations. Commercial alloys were also studied as references. The main objective of our study strategy was to investigate specifically the effect of the oxygen level on the toughness, hardness and metallurgical state of a 13Cr-4Ni stainless steel. Moreover, we wanted to mimic the deoxidizing process (typically used in the industry) using aluminum as a deoxidizing agent. Mass balances were defined to control the addition of a pollutant which was in this case hematite. Parts of the samples were synthesized in an induction furnace that operates in an open system. The molten alloy was protected by liquid argon dripping. Another batch of billets were produced in an induction furnace that works under vacuum. All the samples extracted from these billets were analyzed in two metallurgical states: i.e. as-cast and heat-treated.

An in-depth study was carried out on the microstructural characterization of these samples, verifying the total density of inclusions (number and area), their distribution according to their size and area, as well as their elementary composition and geometry. Besides, thermodynamic calculations were performed to understand their formation sequence and to confirm composition (i.e. the phases associated to these inclusions). The impact of the oxygen level in the samples, inclusions content, melting process and heat treatment was observed in the me-

chanical behavior of the studied material. For this, v-notch Charpy toughness and hardness test were performed. A consistent analysis considering the relationship among all analyzed effects was provided. Here is a summary of all the main conclusions of this work:

- Overall, the melting, casting and heat treating strategies that were developed in this project allowed us to reach the expected results, i.e. different stainless steel billets with controlled levels of oxygen, with different types of inclusions (conclusion 1). Even if our process was not exactly at an industrial scale, it was possible to synthesize samples which were almost fully comparable to the commercialized materials provided by H.-Q.. As a proof, all our thermally treated samples met the required specifications imposed by our industrial partner for Charpy impact tests and hardness.

- The strategy of polluting the melt with hematite was good (conclusion 2): it was possible to completely dissolve it, saturate the melt and obtain the same oxygen content in both melting strategies (2020C-II and 2020V-VIII). When increasing the oxygen content in the melt, there was an increase in the formation of primary (i.e. from the melt state) chromium and Mn oxides.

- By comparing the statistical analysis of inclusions of the heat-treated synthesized samples with the commercial samples, it is possible to see a substantial difference in the proportion of the number of inclusions and area (conclusion 3). We saw that our samples have larger number of inclusions but are related to a lower total area density, which indicates a smaller inclusion size. At the opposite, the commercial samples, despite having a small count of inclusions, have a significantly larger total area. This is a clear indication that the inclusions are bigger which was confirmed in the microstructural analyses. When observed at the SEM / EDS, some inclusions of the commercial alloys show a spherical shape as well as an elementary composition indicating the presence of silicon. These evidences leads us to believe that they were entrained inclusions coming from a slag phase at the top of the melt during the pouring and casting operations. As commercial alloys B and C had low oxygen contents, we suspected that they were deoxidized. Our assumption was validated as we identified the presence of aluminium in the second type of inclusions observed in the steel. Therefore we believe that the slag was not removed efficiently, leaving alumina particles in the melt. We also believe that these alumina inclusions are not whetted properly by the melt and lead to weak inclusions-metal interfaces that lower the mechanical performance of the alloy.

- We were able to identify four main types of inclusions in our cast billets and resulting samples (conclusion 4): 1) alumina particle (when the melt was deoxidized), primary

corundum inclusions (rich in Cr, Mn, Fe) coming after the casting, 3) secondary corundum inclusions (rich in Cr and Mn) forming after the heat treatment and 4) some slag particles. Two types of inclusions presented spherical shape. These were identified as alumina and slag phase (with the content of Si higher than 8%) inclusions respectively. The samples with the spherical inclusions seem to have their mechanical performance affected the most. This explained for example the moderate Charpy performance of de-oxidized samples 2020V-VI and 2020V-II, even thought they had a low oxygen content.

- It could be seen that the number of inclusions decreased after the heat treatment for the samples synthesized in the CONSARC vacuum furnace (conclusion 5). We assumed that they were meta-stables inclusions. When comparing to the argon-dripping furnace, it was concluded that the vacuum furnace produced billets with smaller inclusions. The specimens obtained from the vacuum furnace did show a significant improvement of their v-notch toughness after going through the thermal process. We also believe that the addition of aluminum in the vacuum furnace led in some cases to the formation of a Al-Fe-Cr intermetallic phase that strengthen the material (sample 2020C-I).

- The inclusion analysis from the ingots synthesized in the argon-dripping VIP furnace generally showed a higher content of inclusions (conclusion 6). After the heat treatment, it was also noted that there was a secondary precipitation of inclusions which was confirmed by an increase of their counts.

- Originally, we thought that there would be a direct correlation between the oxygen content of the steel and its v-notch toughness. This was based on the fact that a smaller oxygen content should result in a smaller fraction of inclusions. This expected correlation was not confirmed. Through a careful analysis of these inclusions, it was possible to conclude that spherical inclusions are to be avoided as they lower the impact resistance of the steel. These are primary inclusions coming from a slag phase or are alumina particle formed during the de-oxidation process that could not be transferred to the slag phase. This observation was validated when comparing the relatively poor performance of the 2020V-VI sample which was not skimmed with the skimmed 2020V-IX sample, the latter having a significantly better performance despite its higher oxygen content. In the 2020V-IX, no alumina inclusions was identified even thought we used aluminum as a de-oxidation agent. It is believed that these inclusions rose at the top of the melt and were removed during the skimming operation prior to the casting operation. The low performance of the 2020V-VI bar, despite its low oxygen content, can be related to the presence of alumina inclusions. These inclusions appeared in a smaller number, but

at a larger area. Simulations carried out with FactSage confirmed that this alumina solid phase should be in equilibrium with the melt under these imposed conditions. The medium performance of this billet (2020V-II) leads us to believe that when comparing alumina with other inclusions, they are most probably more brittle which makes the steel more fragile. Another hypothesised scenario is that the liquid metal does not whet the alumina inclusion which induce a poor steel-inclusion interface. When the alloy solidifies, there is not a strong cohesion between the particle surface and the alloy, which most probably lead to poor performance (conclusion 7).

- The importance of removing the slag prior to casting can also be verified through the toughness results of the ingot 2020V-VII. This sample was also deoxidized using aluminium, however, in the analysis of the composition of the inclusions, no aluminum was present. This is a clear indication that the sample was skimmed properly and that the oxygen remaining in the sample produced other inclusions during solidification. The Charpy test performance of this billet was in fact very close to the other samples with lower levels of oxygen (conclusion 8).

- The hardness tests showed similar results among the different synthesized billets. The hardness was also homogeneous throughout a given billet (in both axial and radial positions). Therefore, hardness proved to be a mechanical property that is not affected by the presence of inclusions or the oxygen content present in the sample. The only variation of the hardness occurred as a response to the heat treatment, which made all our samples softer, as expected. This indicates that the hardness is a bulk property linked to the alloy matrix (conclusion 9).

5.2 Recommendations

This study have shown the importance of avoiding specific types of inclusions that are more detrimental to the steel performance than others. It is important to acknowledge that the oxygen content is not the only parameter to account for when it comes to the presence of inclusions.

It is also essential, from our results, to have an optimal skimming strategy in order to 1) remove inclusions that may float at the top of the melt and 2) prevent slag entrainment. The associated inclusions impact negatively the mechanical properties of the final material.

For a given bulk composition and oxygen content, it seems like the size, shape and distribution of the inclusions are affected by the melting strategy (i.e. under vacuum vs argon-dripping). The more expensive vacuum melting may be a better option if one wants to obtain the

best possible performance as the inclusions appeared to be smaller. It is evident from our study that working within the oxygen limits explored in this project (i.e. between 25ppm and 350ppm) leads to acceptable material's performance for both toughness and hardness according to our industrial partner standards. We firmly believe however that maximum performance could be achieved by lowering the oxygen content. This may be of prime importance when the material is subjected to fatigue. This will have to be confirmed in a future work.

5.3 Limitations

There are two main limitations associated to this work when trying to transfer the acquired knowledge to the industrial scale. The first limitation is the slightly different melting, alloying and casting conditions we used. Even though we use semi-industrial induction furnaces, we are aware that we could not fully mimic the exact industrial steelmaking process used to obtain commercial 13Cr-4Ni. More specifically, we believe that the holding time and synthetic-slag practices result in larger inclusions than the one we got in our billets. The second limitation is linked to the choice of deoxidizer used to lower the oxygen content of the steel. Luckily in this case, we used aluminum and were able to compare our billets with commercial alloys that were also de-oxidized with aluminum.

5.4 Future Research

Firstly, an inclusion database could be created by unifying the information from optical microscopy (format of inclusions) and SEM / EDS (elementary composition). A larger number of samples could be analyzed at higher magnification to perform the inclusion density analysis and adding the characterization of the feature's shape. Other mechanical properties could also be measured as well as others production process conditions in order to increase the knowledge related to this material. It could be interesting in the future to study the effect of other de-oxidizing agent such as Mg, Mn-Si, etc, which are also commonly used in the industry. Corrosion resistance could also be quantified using anodic polarization tests. In fact, preliminary anodic polarization tests were performed. Results indicated a better behavior of the synthesized material when exposed to the 3.5 wt.%NaCl solution in its as-cast state. Another experimental study could be performed using our samples (in both as-cast and heat-treated) in order to understand their corrosion resistance performance. This study could be promptly started since many samples were synthesized, carefully divided and identified during this master's project. Also, it would be important to check and quantify the

fraction of austenite and delta ferrite in these billets. Finally, our samples could be further investigated in order to characterize more precisely the inclusion distributions which would generate data useful for statistical fatigue prediction models.

REFERENCES

[1] BP, "BP Statistical Review of World Energy," no. Tech. Rep. 68, pp. 1–64, 2019. [Online]. Available: https://www.bp.com/content/dam/bp/business-sites/en/global/corporate/pdfs/energy-economics/statistical-review/bp-stats-review-2019-full-report.pdf

[2] I. Kougias, G. Aggidis, F. Avellan, S. Deniz, U. Lundin, A. Moro, S. Muntean, D. Novara, J. I. Pérez-Díaz, E. Quaranta, P. Schild, and N. Theodossiou, "Analysis of emerging technologies in the hydropower sector," *Renewable and Sustainable Energy Reviews*, vol. 113, no. January, p. 109257, 2019. [Online]. Available: https://doi.org/10.1016/j.rser.2019.109257

[3] M. Hassanipour, "Fatigue Crack Propagation Under Variable Amplitude Loading in Steels Used in Francis Turbine Runners," Ph.D. dissertation, École Polytechnique de Montréal, Montreal, QC, 2017.

[4] D. Thibault, M. Gagnon, and S. Godin, "The effect of materials properties on the reliability of hydraulic turbine runners," *International Journal of Fluid Machinery and Systems*, vol. 8, no. 4, pp. 254–263, 2015.

[5] ASM International Committee, "Cast Irons," in *ASM Handb. - Prop. Sel. Irons, Steels, High-Performance Alloys.*, mar 1990, vol. 1, pp. 3–11. [Online]. Available: www.asminternational.org

[6] M. Sabourin, D. Thibault, D. A. Bouffard, and M. Lévesque, "New parameters influencing hydraulic runner lifetime," *IOP Conference Series: Earth and Environmental Science*, vol. 12, p. 012050, 2010.

[7] ASM International Committee, "Selection of Cast Stainless Steels," *ASM Handbook, Volume 6: Welding, Brazing, and Soldering*, vol. 6, pp. 495–499, 1993. [Online]. Available: www.asminternational.org

[8] ASM International Committee, "Welding of stainless steels," in *ASM Handbook, Vol. 6 Welding, Brazing, Solder.*, DL Olson, TA Siewert, S Liu, GR Edwards, Ed., 1993, vol. 6, pp. 677–707.

[9] I. Calliari, M. Zanesco, M. Dabalà, K. Brunelli, and E. Ramous, "Investigation of microstructure and properties of a Ni-Mo martensitic stainless steel," *Materials and Design*, vol. 29, no. 1, pp. 246–250, 2008.

[10] F. Foroozmehr and P. Bocher, "On the ductile rupture of 13% Cr-4% Ni martensitic stainless steels," *International Journal of Fracture*, vol. 224, no. 1, pp. 67–82, 2020. [Online]. Available: https://doi.org/10.1007/s10704-020-00446-2

[11] E. Folkhard, *Welding Metallurgy of Stainless Steels*. Springer-Verlag Wien New York, 1984, vol. 1.

[12] P. Bilmes, M. Solari, and C. Llorente, "Characteristics and effects of austenite resulting from tempering of 13Cr–NiMo martensitic steel weld metals," *Materials Characterization*, vol. 46, no. 4, pp. 285–296, apr 2001. [Online]. Available: https://www.sciencedirect.com/science/article/pii/S1044580300000991

[13] Y. Iwabuchi, "Factors affecting on mechanical properties of soft martensitic stainless steel castings," *JSME International Journal, Series A: Solid Mechanics and Material Engineering*, vol. 46, no. 3, pp. 441–446, 2003.

[14] G. Krauss, *Steels: processing, structure, and performance*, 2005.

[15] M. Boniardi, A. Casaroli, and P. d. M. Dipartimento Di Meccanica, "Stainless steels Gruppo Lucefin Research & Development," *Lucefin*, pp. 10–20, 2014. [Online]. Available: http://www.fa-fe.com/files/pdf/libri{_}articoli/en/2{_}Stainless{_}steels.pdf

[16] G. Krauss, "Martensite in steel: strength and structure," *Materials Science and Engineering: A*, vol. 273-275, pp. 40 – 57, 1999. [Online]. Available: http://www.sciencedirect.com/science/article/pii/S0921509399002889

[17] T. G. Gooch, "Heat treatment of welded 13for sour service," *Welding Journal*, vol. 74, no. 7, 7 1995.

[18] H. Kitahara, R. Ueji, N. Tsuji, and Y. Minamino, "Crystallographic features of lath martensite in low-carbon steel," *Acta Materialia*, vol. 54, no. 5, pp. 1279 – 1288, 2006. [Online]. Available: http://www.sciencedirect.com/science/article/pii/S1359645405006701

[19] C. Celada-Casero, B. M. Huang, J. R. Yang, and D. San-Martin, "Microstructural mechanisms controlling the mechanical behaviour of ultrafine grained martensite/austenite microstructures in a metastable stainless steel," *Materials and Design*, vol. 181, p. 107922, 2019. [Online]. Available: https://doi.org/10.1016/j.matdes.2019.107922

[20] T. G. E. Dossett, Jon L., "1.3.5 tempered martensite," 2013. [Online]. Available: https://app.knovel.com/hotlink/khtml/id:kt00C6Y5W1/asm-handbook-volume-4a/tempered-martensite

[21] J. C. Lippold and D. J. Kotecki, *Welding Metallurgy and Weldability of Stainless Steels*, 2005.

[22] E. K. E. Porter, David A. and M. Y. Sherif, *Phase Transformations in Metals and Alloys*, 2009.

[23] ASM International Committee, "Primary Processing Effects on Steel Microstructure and Properties," in *ASM Handbook, Steels - Processing, Structure, and Performance*, 2005, pp. 677–707.

[24] J. D. Crawford, K. Rohrig, and S. Bechet, "High-Strength Cast Stainless Steels with Enhanced Corrosion Resistance," in *Stainless Steel Castings*, A. S. Melilli, Ed. West Conshohocken, PA: ASTM International, jan 1982, pp. 355–368. [Online]. Available: https://www.astm.org/

[25] F. Foroozmehr, Y. Verreman, J. Chen, D. Thibault, and P. Bocher, "Effect of inclusions on fracture behavior of cast and wrought 13% Cr-4% Ni martensitic stainless steels," *Engineering Fracture Mechanics*, vol. 175, pp. 262–278, 2017. [Online]. Available: http://dx.doi.org/10.1016/j.engfracmech.2017.02.002

[26] W. F. Smith, *Structure and properties of engineering alloys*, 1981.

[27] D. Thibault, P. Bocher, M. Thomas, J. Lanteigne, P. Hovington, and P. Robichaud, "Reformed austenite transformation during fatigue crack propagation of 13%Cr-4%Ni stainless steel," *Materials Science and Engineering A*, vol. 528, no. 21, pp. 6519–6526, 2011. [Online]. Available: http://dx.doi.org/10.1016/j.msea.2011.04.089

[28] ASM International Committee, "STEEL CASTINGS," *ASM Handbook, Volume 01 - Properties and Selection: Irons, Steels, and High-Performance Alloys - 23.1 Classifications and Specifications*, vol. 1, pp. 363–379, mar 1990. [Online]. Available: www.asminternational.orghttps://app.knovel.com/hotlink/pdf/id:kt007OPPY1/asm-handbook-volume-01/classifications-specifications

[29] I. ASTM, "Standard Specification for Castings, Iron-Chromium, Iron-Chromium-Nickel, Corrosion Resistant, for General Application," *a743/a743M 17*, vol. i, pp. 1–8, 2014. [Online]. Available: www.astm.org,

[30] U. S. S. Corporation, *The making, shaping and treating of steel*. United States Steel, 1957, vol. 7.

[31] DOE and AISI, "Technology roadmap research program for the steel industry," American Iron and Steel Institute, Tech. Rep. DE-FC36-97ID13554, 2011. [Online]. Available: https:www.steel.org/~/media/Files/AISI/Making%20Steel/TechReportResearchProgramFINAL.pdf

[32] G. Krauss, *Steels: Processing, Structure, and Performance*. Novelty, OH: ASM International, 2015. [Online]. Available: https://www.asminternational.org/documents/10192/0/05441G_TOC+%282%29.pdf/82ee161b-e171-9960-caab-74619423b6a4

[33] A. L. V. Da Costa E Silva, "Non-metallic inclusions in steels - Origin and control," pp. 283–299, 2018. [Online]. Available: https://doi.org/10.1016/j.jmrt.2018.04.003

[34] L. Zhang and B. G. Thomas, "State of the art in the control of inclusions during steel ingot casting," *Metallurgical and Materials Transactions B: Process Metallurgy and Materials Processing Science*, vol. 37, no. 5, pp. 733–761, 2006.

[35] L. Holappa and O. Wijk, "Inclusion Engineering," in *Treatise on Process Metallurgy*, 1st ed. Elsevier Ltd., 2014, vol. 3, pp. 347–372. [Online]. Available: http://dx.doi.org/10.1016/B978-0-08-096988-6.00008-0

[36] R. Kiessling and N. Lange, *Non-metallic inclusions in steel*, 1978.

[37] R. Kiessling, *The influence of non-metallic inclusions on the properties of steel*, 1969.

[38] Y. Yang, K. Raipala, and L. Holappa, *Ironmaking*. Elsevier Ltd., 2014, vol. 3. [Online]. Available: http://dx.doi.org/10.1016/B978-0-08-096988-6.00017-1

[39] P. A. Thornton, "The influence of nonmetallic inclusions on the mechanical properties of steel: A review," *Journal of Materials Science*, vol. 6, no. 4, pp. 347–356, 1971.

[40] A. Nicholson and D. S. Thornto, *Steelmaking and Non-Metallic Inclusions*. American Cancer Society, 2006. [Online]. Available: https://onlinelibrary.wiley.com/doi/abs/10.1002/9783527603978.mst0063

[41] E. Steinmetz and H.-U. Lindenberg, "Inclusion morphology during aluminum deoxidation (translated)," *Archiv für das Eisenhüttenwesen*, vol. 47, no. 4, pp. 199–204, 1976. [Online]. Available: https://onlinelibrary.wiley.com/doi/abs/10.1002/srin.197603806

[42] W. Tiekink, R. Boom, A. Overbosch, R. Kooter, and S. Sridhar, "Some aspects of alumina created by deoxidation and reoxidation in steel," *Ironmaking*

& Steelmaking, vol. 37, no. 7, pp. 488–495, 2010. [Online]. Available: https://doi.org/10.1179/030192310X12700328925822

[43] j. s. de barbadillo, *Sulfide Inclusions in Steel*. american society of metals, 1975. [Online]. Available: https://books.google.ca/books?id=SmyxzQEACAAJ

[44] S. Meimandi, N. Vanderesse, D. Thibault, P. Bocher, and M. Viens, "Macro-defects characterization in cast CA-6NM martensitic stainless steel," *Materials Characterization*, vol. 124, pp. 31–39, 2017. [Online]. Available: http://dx.doi.org/10.1016/j.matchar.2016.11.040

[45] R. Dasgupta and N. S. Foundation, "Common Defects in Various Casting Processes," *Casting*, pp. 1192–1202, 2018.

[46] C. Luo, "Modeling the behavior of inclusions in plastic deformation of steels," Ph.D. dissertation, KTH, Production Engineering, 2001, nR 20140805.

[47] Y. Murakami and M. Endo, "Effects of defects, inclusions and inhomogeneities on fatigue strength," *International Journal of Fatigue*, vol. 16, no. 3, pp. 163 – 182, 1994. [Online]. Available: http://www.sciencedirect.com/science/article/pii/0142112394900019

[48] A. L. V. Da Costa E Silva, "The effects of non-metallic inclusions on properties relevant to the performance of steel in structural and mechanical applications," *Journal of Materials Research and Technology*, vol. 8, no. 2, pp. 2408–2422, 2019. [Online]. Available: https://doi.org/10.1016/j.jmrt.2019.01.009

[49] M. P. Ryan, D. E. Williams, R. J. Chater, B. M. Hutton, and D. S. McPhail, "Why stainless steel corrodes," *Nature*, vol. 415, no. 6873, pp. 770–774, 2002. [Online]. Available: https://doi.org/10.1038/415770a

[50] D. E. Williams, M. R. Kilburn, J. Cliff, and G. I. Waterhouse, "Composition changes around sulphide inclusions in stainless steels, and implications for the initiation of pitting corrosion," *Corrosion Science*, vol. 52, no. 11, pp. 3702 – 3716, 2010. [Online]. Available: http://www.sciencedirect.com/science/article/pii/S0010938X10003598

[51] A. Akhiate, "Effet de la teneur en carbone sur la résistance du ca6nm à la propagation des fissures de fatigue," Ph.D. dissertation, 2015. [Online]. Available: https://search.proquest.com/dissertations-theses/effet-de-la-teneur-en-carbone-sur-résistance-du/docview/1955148924/se-2?accountid=40695

[52] J. Chaix and M. Brochu, “Influence de la température de revenu sur la résistance du CA6NM à la propagation des fissures de fatigue,” Ph.D. dissertation, 2014. [Online]. Available: https://publications.polymtl.ca/1663

[53] Steel Founders’ Society of America, “High Alloy Data Sheets Corrosion Series,” *Steel Castings Handbook*, pp. 1–7, 2004.

[54] M. Jolly, “1.18 - Castings,” in *Comprehensive Structural Integrity*, 2007, vol. 1, pp. 377–466.

[55] ASTM International, “A751-20 Standard Test Methods and Practices for Chemical Analysis of Steel Products.” *ASTM Standard*, pp. 1–6, 2020.

[56] ASTM, “E1019-18 Standard Test Methods for Determination of Carbon, Sulfur, Nitrogen, and Oxygen in Steel, Iron, Nickel, and Cobalt Alloys by Various Combustion and Inert Gas Fusion Techniques.” *ASTM Standard*, pp. 1–22, 2018.

[57] S. Practice, “Standard Practice for Microetching Metals and Alloys ASTM E-407,” vol. 07, no. Reapproved 2015, pp. 1–22, 2016.

[58] ASTM International, “ASTM E23 18, Standard Test Methods for Notched Bar Impact Testing of Metallic Materials,” *ASTM Standard*, pp. 1–26, 2018. [Online]. Available: www.astm.org,

[59] G. Require, G. Re, R. Bar, P. Vessels, and N. A. Plate, “Standard Test Methods for Rockwell Hardness of Metallic Materials 1 , 2,” pp. 1–38, 2014.

[60] N. Search, L. Out, T. O. Standard, B. Hardness, S. Machines, and B. H. Uncertainty, “Standard Test Method for Brinell Hardness of Metallic Materials Standard Test Method for Brinell Hardness of Metallic Materials 1 Standard Test Method for Brinell Hardness of Metallic Materials,” *ASTM International, West Conshohocken, PA, 2017, www.astm.org*, no. June, pp. 1–36, 2012.

[61] D. Pavlyuchkov, B. Przepiórzyński, W. Kowalski, T. Y. Velikanova, and B. Grushko, “Al-Cr-Fe phase diagram. Isothermal Sections in the region above 50 at% Al,” *Calphad: Computer Coupling of Phase Diagrams and Thermochemistry*, vol. 45, pp. 194–203, 2014.

[62] ASTM E 23-12c, “E 23-12c Standard Test Methods for Notched Bar Impact Testing of Metallic Materials,” *ASTM Standard*, vol. i, pp. 1–25, 2013.

[63] C. Hays and D. H. Patrick, “Hardness Conversion Data for CA6NM alloy,” no. Tech. Communication, Gray Tool Company, Houston, Texas, pp. 229–233, 1982.

[64] Hydro-Quebéc, “Étude expérimentale sur les correspondances entre diverses méthodes de mesure et échelles de dureté pour les aciers inoxydables de type 415,” no. Tech. Rep., Hydro-Québec, Montreal, QC, p. 41, 2012.

APPENDIX A MEASUREMENTS OF ELEMENTAL COMPOSITION ANALYSIS

Table A.1 OES Results - VIP Bars

Identif.	Fe	C	Cr	Ni	Mn	P	S	Si	Mo	Al
Required	Bal.	0.03	11.5-14.0	3.5-5.5	0.5-1.0	0.03	0.03	0.60	0.5-1.00	
Expected	Bal.	0.01	12.73	4.40	0.90	0.01	0.00	0.14	0.75	
	Bal.	0.0153	12.7262	5.0609	0.9484	0.0082	0.0017	0.1375	0.6725	
2019V-I	Bal.	0.0117	13.1101	5.0812	0.9529	0.0077	0.0019	0.1340	0.6674	
	Bal.	0.0118	13.1583	5.1018	0.9592	0.0086	0.0024	0.1344	0.6696	
Average	-	0.0130	12.9982	5.0813	0.9535	0.0082	0.0020	0.1353	0.6698	
2020V-II	Bal.	0.0211	13.1169	4.4026	0.9052	0.0083	0.0061	0.1085	0.6527	0.0820
	Bal.	0.0241	13.2218	4.5862	0.8996	0.0083	0.0032	0.1115	0.6555	0.0812
Average	-	0.0226	13.1693	4.4944	0.9024	0.0083	0.0046	0.1100	0.6541	0.0816
2020V-VI	Bal.	0.0374	12.9079	5.0781	0.9076	0.0110	0.0018	0.0932	0.7058	0.0647
	Bal.	0.0629	13.4183	5.1051	0.9110	0.0111	0.0025	0.0922	0.7213	0.0670
Average	-	0.0502	13.1631	5.0916	0.9093	0.0110	0.0022	0.0927	0.7135	0.0658
2020V-VII	Bal.	0.0095	11.9590	4.6199	0.8520	0.0100	0.0021	0.0859	0.6571	0.0013
	Bal.		12.3366	4.6569	0.8523	0.0107	0.0026	0.0874	0.6457	0.0020
Average	-	0.0095	12.1478	4.6384	0.8521	0.0103	0.0023	0.0867	0.6514	0.0016
2020V-VIII	Bal.	0.0085	11.3272	4.7685	0.8273	0.0096	0.0013	0.0503	0.6431	0.0011
	Bal.	0.0030	11.3372	4.6732	0.8197	0.0103	0.0023	0.0514	0.6359	0.0015
Average	-	0.0058	11.3322	4.7209	0.8235	0.0100	0.0018	0.0508	0.6395	0.0013
2020V-IX	Bal.	0.0083	12.0969	4.7419	0.9431	0.0097	0.0016	0.0809	0.6620	0.0036
	Bal.	0.0046	12.4683	4.7133	0.9358	0.0098	0.0022	0.0802	0.6564	0.0040
Average	-	0.0064	12.2826	4.7276	0.9395	0.0098	0.0019	0.0806	0.6592	0.0038

Table A.2 OES Results - CONSARC

Identif.	Fe	C	Cr	Ni	Mn	P	S	Si	Mo	Al
Required	Bal.	0.03	11.5-14.0	3.5-5.5	0.5-1.0	0.03	0.03	0.60	0.5-1.00	
Expected	Bal.	0.01	12.73	4.40	0.90	0.01	0.00	0.14	0.75	
	Bal.	0.0177	14.5914	5.2470	1.0841	0.0127	0.0054	0.1235	0.7512	
2019C-I	Bal.	0.0153	14.5415	5.3566	1.0367	0.0099	0.0038	0.1133	0.7662	
	Bal.	0.0151	14.5856	5.2980	1.0372	0.0101	0.0022	0.1127	0.7588	
Average	-	0.0161	14.5728	5.3005	1.0527	0.0109	0.0038	0.1165	0.7587	
2020C-I	Bal.	0.0053	12.7719	4.5980	0.7034	0.0092	0.0018	0.0327	0.7922	0.1501
	Bal.	0.0063	12.2997	4.6354	0.7026	0.0089	0.0012	0.0309	0.7737	0.1477
Average	-	0.0058	12.5358	4.6167	0.7030	0.0091	0.0015	0.0318	0.7829	0.1489
2020C-II	Bal.	0.0040	12.2198	4.5712	0.5539	0.0096	0.0018	0.0521	0.6731	0.0177
	Bal.	0.0043	12.2790	4.3597	0.5382	0.0102	0.0033	0.0508	0.6687	0.0195
Average	-	0.0042	12.2494	4.4654	0.5460	0.0099	0.0025	0.0514	0.6709	0.0186